

Dissertation

submitted to the

Combined Faculties for the Natural Sciences and for Mathematics

of the Ruperto-Carola University of Heidelberg, Germany

for the degree of

Doctor of Natural Sciences

presented by

Diplom-Physiker Bastian Barton

born in Wiesbaden, Germany

Oral examination: June 11th, 2008

Development and Implementation of In-Focus Phase Contrast TEM for Materials and Life Sciences

Referees: PD Dr. Rasmus R. Schröder
Prof. Dr. Dr. Christoph Cremer

Entwicklung und Implementierung von in-Fokus-Phasenkontrast-TEM für Materialwissenschaften und Life Sciences

Transmissions-Elektronenmikroskopie (TEM) erlaubt die Abbildung von Objekten aus Materialwissenschaften und Biologie mit einer Auflösung von wenigen nm bis wenigen Å. Durch Kryopräparation sind 3D-Rekonstruktionen von biologischen Systemen unter physiologischen Bedingungen möglich. Die Auflösung ist dabei eingeschränkt durch das niedrige Signal-zu-Rausch-Verhältnis (SNR) der Bilder. Schwache Phasenobjekte, wie native biologische Proben, werden erst durch Phasenkontrast sichtbar, der in der konventionellen TEM durch Defokussieren erzeugt wird. Die Defokussierung liefert jedoch schwachen Kontrast und eine unvollständige Übertragung der Objektinformation, was die Rekonstruktion erschwert. Wünschenswert ist daher die Kontrasterzeugung durch eine Phasenplatte in der hinteren Brennebene der Objektivlinse. Dies ermöglicht eine artefaktfreie und kontrastreiche Abbildung schwacher Phasenobjekte. Phasenplatten wurden in der TEM bisher nur in Form eines dünnen Kohlenstofffilms realisiert, der jedoch Signal- und damit Auflösungsverluste verursacht.

Diese Arbeit zeigt erstmals die technische Implementierung einer elektrostatischen (Boersch-) Phasenplatte und liefert den experimentellen Beweis ihrer Funktionsfähigkeit. Die Boersch-Phasenplatte erzeugt maximalen Phasenkontrast, während Auflösungsverluste vermieden werden. Sie besteht aus einer miniaturisierten elektrostatischen Einzellinse, die eine Phasenverschiebung des ungestreuten Wellenanteils bewirkt. Abschattungseffekte durch die Linse werden durch optische Vergrößerung der Brennebene minimiert. Die Weiterentwicklung zur gänzlich abschattungsfreien "anamorphotischen" Phasenplatte wird beschrieben, die einen pseudotopografischen (Hilbert-) Kontrast erzeugt. Die Verbesserung der elektronenmikroskopischen Rekonstruktion durch eine solche Hilbert-Phasenplatte wird an Hand von Elektronentomografie ungefärbter Zellschnitte demonstriert.

Development and Implementation of In-Focus Phase Contrast TEM for Materials and Life Sciences

Transmission electron microscopy (TEM) allows the imaging of objects from materials sciences and biology with a resolution of a few nm to a few Å. Biological systems can be reconstructed in 3D under physiological conditions using cryo TEM. However, the low signal-to-noise ratio (SNR) of individual images hampers resolution. Weak-phase objects such as native biological samples can be visualized only by phase contrast, which is generated in conventional TEM by defocusing. The defocus technique yields weak contrast and incomplete transfer of object information, which makes reconstruction difficult. Therefore, generating contrast by placing a phase plate in the back focal plane of the objective lens is desirable. This allows for artefact-free imaging of weak-phase objects with strong contrast. For TEM, phase plates have been realised only in the form of a thin carbon film which causes loss of signal and resolution.

This work presents the first technical implementation of an electrostatic (Boersch) phase plate for TEM and gives the experimental proof-of-principle for this device. The Boersch phase plate generates maximum phase contrast while avoiding resolution loss. It consists of a miniaturised electrostatic einzel lens that shifts the phase of the unscattered wave. Obstruction effects are minimised by optically magnifying the focal plane. The advancement to an entirely obstruction-free phase plate is outlined which generates pseudo-topographic (Hilbert) contrast. The enhancement of electron-microscopic reconstruction by such a Hilbert phase plate is demonstrated for electron tomography of unstained cell sections.

Table of Contents

1 Enabling In-focus Phase Contrast TEM: Motivations & Goals.....	1
1.1 Constraints on TEM imaging of native biological specimens.....	2
1.2 The problem of weak phase contrast.....	4
1.3 Phase plates: a solution for the weak contrast problem.....	6
1.4 Which is the ideal implementation of in-focus phase contrast?.....	9
1.5 Goals of this work.....	10
1.6 A short overview of the contents.....	11
2 Mechanisms of Contrast Formation in TEM.....	15
2.1 Principles of image formation.....	15
2.1.1 Electron scattering by weak-phase-weak-amplitude objects.....	15
2.1.2 The influence of aperture functions on image formation.....	16
2.1.3 The general contrast transfer functions.....	18
2.1.4 The relation between contrast and SNR.....	19
2.1.5 Image formation for thick biological objects.....	19
2.1.6 Defocus phase contrast.....	21
2.1.7 The damping of the contrast transfer function.....	23
2.2 In-focus phase contrast generated by physical phase plates.....	26
2.2.1 Zernike-type phase plates.....	26
2.2.2 Topographic in-focus contrast by Hilbert-type phase plates.....	28
2.2.3 Comparison of coherence loss by Hilbert- and Zernike-type phase plates.....	30
2.2.4 Single-sideband imaging.....	31
2.2.5 Modelling phase shift and lens effect of Boersch's electrostatic phase plate.....	32
3 Development and Proof-of-Concept of the Boersch Electrostatic Phase Plate.....	35
3.1 Proof-of-concept.....	35
3.1.1 Fabrication of the miniaturised electrostatic einzel lens.....	36
3.1.2 Experimental verification of the $\pi/2$ phase shift.....	39
3.1.3 Assessing the lens effect of the ring electrode.....	42
3.2 The signal transfer properties of possible Boersch phase plate geometries.....	43
3.2.1 Phase contrast simulations as guide for phase plate design.....	43
3.2.2 Obstruction of structure factors by the ring electrode and twofold vs. threefold lens-supporting rods.....	45
3.2.3 Experimental verification of single-sideband contrast transfer for threefold phase plate support geometry.....	49

3.3 Evolution of the Boersch phase plate architecture.....	50
3.4 Conclusion.....	52
4 Boersch Phase Plate Imaging Enhanced: the PACEM.....	55
4.1 Finding an optical solution for the Boersch obstruction problem.....	55
4.2 The concept of a magnified back focal plane.....	56
4.3 Image simulations assessing the contrast of the Boersch phase plate in a magnified BFP.....	57
4.4 Reducing the aberrations of the transfer lenses.....	59
4.5 Design, manufacturing and test of a precise phase plate positioning system.....	61
4.6 Conclusion.....	62
5 Obstruction-free Phase Contrast: The Anamorphic Phase Plate.....	63
5.1 Is a matter-free electrostatic phase plate possible?.....	63
5.2 The concept of the anamorphic phase plate.....	65
5.3 Simulating in-focus anamorphic phase contrast imaging.....	67
5.4 Implications on the technical design.....	69
5.5 Conclusion.....	70
6 Electron Tomography and Cryo TEM with Hilbert Phase Plates: an Application Study...73	
6.1 Phase contrast in biological electron tomography.....	74
6.1.1 Assessing the phase contrast of thick specimens.....	75
6.1.2 Limitations of defocus contrast CET.....	76
6.1.3 Advantages of in-focus HPC tomography.....	78
6.2 Development of Hilbert phase plate tomography.....	79
6.2.1 Implementation of Hilbert carbon film phase plates.....	80
6.2.2 Experimental characterisation of HPC contrast transfer.....	81
6.2.3 Hilbert phase contrast imaging of frozen hydrated specimens.....	84
6.2.4 Numerical correction for the anti-symmetrical Hilbert contrast transfer.....	86
6.2.5 Effects of edge orientation, gap width and film thickness variations.....	87
6.3 Hilbert phase contrast tomography of embedded sections.....	89
6.3.1 Material and methods.....	90
6.3.2 Reconstructions of mouse muscle sections.....	92
6.3.3 Unstained yeast cell sections as a test for Hilbert CET.....	92
6.4 Discussion & Conclusion.....	95
7 Discussion & Outlook.....	99
7.1 Current approaches to the weak phase contrast problem.....	99

7.2 In-focus Hilbert phase contrast enhances electron tomography.....	100
7.3 First realization and proof-of-principle for a Boersch electrostatic phase plate.....	102
7.4 The PACEM project: exploiting ideal phase contrast for biology and CET.....	104
7.5 A concept for obstruction-free electrostatic phase plates.....	104
7.6 The future of in-focus TEM.....	105
Appendix A: Basic concepts of electron optics.....	109
A.1 Electron lenses.....	109
A.1.1 The movement of electrons in a static electromagnetic field.....	109
A.1.2 Round electron lenses and the paraxial equation.....	110
A.1.3 Asymptotic image formation of round lenses.....	111
A.1.4 Deviations from ideal imaging: lens aberrations.....	112
A.1.5 Spherical aberration.....	113
A.2 From particle to wave optics.....	114
A.2.1 The paraxial Schrödinger equation.....	114
A.2.2 Propagation of the electron wave through a round lens	115
A.2.3 The wave-optical description of lens aberrations.....	116
Appendix B: Fabrication of Hilbert carbon film phase plates.....	119
Appendix C: Construction of a Piezo-driven Phase Plate Goniometer.....	121
Appendix D: Digital image processing with MatLab.....	123
<i>Bibliography.....</i>	<i>127</i>
<i>Publications.....</i>	<i>135</i>
<i>Danksagung.....</i>	<i>137</i>

Abbreviations

2D	<i>Two-dimensional</i>
3D	<i>Three-dimensional</i>
APP	<i>Anamorphic phase plate</i>
BFP	<i>Back focal plane (of the objective lens)</i>
(C)ET	<i>(Cryo) electron tomography</i>
CTF	<i>Contrast transfer function</i>
EMD	<i>Electron microscopy database (Tagari et. al 2002)</i>
FIB	<i>Focused ion beam</i>
HPC	<i>Hilbert phase contrast</i>
PDB	<i>RCSB Protein Data Bank (www.rcsb.org)</i>
Power spectrum	<i>Squared modulus of the Fourier transform of a TEM image</i>
PSF	<i>Point spread function</i>
SEM	<i>Scanning electron microscope</i>
SNR	<i>Signal-to-noise ratio</i>
TEM	<i>Transmission electron microscope</i>
ZPC	<i>Zernike phase contrast</i>

1 Enabling In-focus Phase Contrast TEM: Motivations & Goals

Transmission electron microscopy (TEM) allows the imaging and three-dimensional structural analysis of pleomorphic biological systems in a close-to-native state. The technique has a precision of a few nm up to a few Å. Unlike other methods of biological structure determination such as X-ray crystallography or NMR¹, TEM is not subject to general restrictions in size, mass or periodicity of the objects under investigation. Complex systems such as cell organelles, whole cells and tissues can be studied, along with single molecules, complexes and macromolecular assemblies. The latter may occur in various conformational states within the same sample. For example, the cytoskeleton of native eukaryotic cells (Medalia et al. 2002), the assembly of clathrin-coated cellular vesicles (Cheng et al. 2007) and functional states of the nuclear pore complex (Beck et al. 2002, 2007; Stoffer et al. 2003) have been visualised in some detail by cryo electron tomography (CET). The 3D structure of a protein complex forming a water pore in the cell membrane has been determined at a near-atomic resolution of 1.8 Å by electron crystallography (Gonen et al. 2004). A reconstruction of the molecular backbone of the proteins forming a virus capsid was recently achieved at 4.5 Å resolution by single particle TEM reconstruction, and ribosomes have been studied at 2.4 Å resolution (Ban et al. 2000) by using the same method.

Nevertheless, structural studies of native biological systems are generally hampered by the particularly low signal-to-noise ratio (SNR) of individual images. For example, protein macromolecules have a tertiary structure composed of beta strands and alpha helices on the sub-nanometer scale, which is essential for understanding the function of such molecular machines. However, these features can in general only be resolved in specimens with a high translational symmetry, i.e. 2D crystals (Kühlbrandt et al. 1994), or rotational symmetry, such as viruses or helical filaments (Schröder et al, 1993; Holmes et al. 1998). For specimens lacking such inherent symmetry, as they are encountered in analysis of single molecular complexes (“single particle EM”), sub-nanometer accuracy of the reconstruction can only be obtained by proper alignment and averaging of several hundred thousand individual particle images (Penczek et al. 1992). This procedure is generally only applicable if a sufficient contrast of the individual particles is present in the images, as these have to

¹ nuclear magnetic resonance

be identified and aligned with two translational and three rotational degrees of freedom. Owing to these constraints, the single particle method is limited to objects of $> 100 \text{ kD}^2$ molecular weight at present (Henderson 1995). In the case of the unique amorphous structures that are studied in CET, the resolution of tomograms is limited to 4-5 nm at present. Theoretically, electron tomography could reach molecular resolution (Lucic et al. 2005), as each data set has high information content and redundancy, but the interpretation of the tomographic reconstruction is hampered by the low SNR.

1.1 Constraints on TEM imaging of native biological specimens

The high level of noise compared to the signal of biological TEM imaging originates in the constraints on specimen preparation and in the highly radiation-sensitive nature of the delicate objects. Biological systems maintain their native structure only in their natural aqueous environment. However, for electron imaging, the sample has to be transferred into the high vacuum of the TEM, and therefore has to be fixed, i.e. the contained water has to be removed or prevented from evaporating.

To obtain sufficient contrast, specimens are often mixed with solutions of heavy metal salts (e.g. uranyl acetate) and then air dried. The stain penetrates cavities inside the objects, where it replaces water (negative staining). Despite the strong contrast produced by the heavy atoms, it is only the stain envelope and not the organic structure itself that is imaged. Moreover, the biological objects are usually distorted or flattened by air drying. Therefore high structural resolutions cannot be obtained by this method. Another form of fixation is dehydrating the sample in organic solvent and embedding in polymer or resin, followed by sectioning. Although the biological material is thereby conserved, the dehydration causes severe distortion of cellular features.

The preparation of frozen-hydrated (or “cryo-”) specimens was established in the early 1980s (Taylor and Glaeser 1976; Dubochet et al. 1981) and is still the method of choice for biological specimens. A thin film of water or buffer ($\sim 40 \text{ nm}$ to $1 \text{ }\mu\text{m}$) containing the biological material, e.g. a solution of protein complexes or a thin part of a cell, is spread on top of a holey carbon support film (fig. 1.1). The sample is rapidly plunged into liquid ethane held close to liquid nitrogen temperature (-196°C) and is thereby “shock-frozen” with a high cooling rate. Instead of forming crystalline ice, the surrounding buffer is vitrified and resembles a fluid with high viscosity. This direct approach

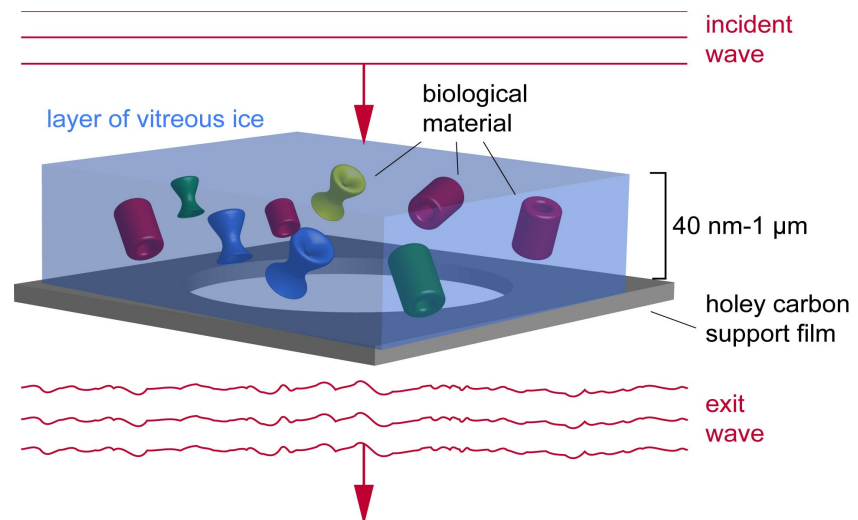
² 1 D (Dalton) = 1 u (atomic unit) = $1.660 \cdot 10^{-27} \text{ kg}$, which is 1/12 of the mass of a carbon atom

has proven to be the best method for preservation of the native specimen structure and for high resolution electron microscopy (Lucic et al. 1995).

At the same time, frozen-hydrated biological samples, such as e.g. suspensions of purified protein complexes, are highly radiation-sensitive. The irradiation with high energy electrons (typically 120 – 300 keV) causes gradual damage to the native structure, primarily by ionisation and formation of free radicals. Despite the high viscosity of the vitreous embedding, such free radicals can diffuse and destroy the specimen structure, e.g. by breaking of chemical bonds. It is assumed that as a consequence, molecular structures can fall apart into fragments, whereas the diffusion of these fragments is largely prevented by the ice embedding. The most obvious form of electron beam damage is the formation of gas bubbles within the ice layer, which often occurs in CET (Grimm et al. 1997).

To keep the amount of beam damage as low as possible and to preserve the object's native structure during analysis, “low-dose” conditions have to be applied. This means that the accumulated electron dose during the acquisition of images of one individual object is kept as low as possible (< 100 electrons/ \AA^2), depending on the aspired resolution. For methods aiming at high resolution, such as electron crystallography and single-particle analysis, a value of 20 electrons per \AA^2 of specimen surface is often assumed as a rough upper limit. This dose limitation usually permits the acquisition of no more than 1-3 micrographs of the same object, before its native structure is potentially destroyed. In CET, where a tilt series of typically 60-120 images of an individual object area has to be recorded, the required dose is considerably higher (~ 50 - 200 $e^-/\text{\AA}^2$). High resolution details of the specimen are potentially destroyed by this amount of irradiation, and consequently, tomographic reconstructions do not allow molecular resolutions (< 1 nm).

Figure 1.1.: The TEM as a projector. The biological material is shock-frozen inside its native environment (a thin layer of water or buffer, spanning a hole in a carbon support film) and transferred into the EM, where it is kept under vacuum at liquid nitrogen temperature. The specimen is illuminated by parallel electron rays, representing a plane wave. Due to the weak scattering, the entire object information is encoded in a small distortion of the exit wave front.



The utilisable energy, or electron dose, is thus strictly limited for biological cryo TEM imaging. Owing to the large chromatic aberration of state-of-the-art electron lenses, inelastic scattering can not be converted into a high resolution image, so that virtually the entire image is generated from elastic scattering. It was found that for typical electron energies (80-500 keV), the ratio of inelastic to elastic scattering is roughly 3:1. This means that for one elastic scattering event, an energy of ~60 eV is deposited in the specimen (Henderson 1995), potentially causing specimen damage as described above. Therefore, as much object information as possible has to be extracted per elastically scattered electron, or in other words, elastic scattering has to be converted into image contrast with the highest possible efficiency.

1.2 The problem of weak phase contrast

Image contrast is the key parameter in biological TEM. There is always a high amount of noise present in the images, contributed from the ice embedding and the detector³. Therefore, the signal-to-noise ratio of an image for a fixed electron dose is determined by the contrast. One major problem of biological TEM therefore originates in the mechanism of image contrast formation. The high energy electron beam is scattered only weakly by native biological samples, as those consist predominantly of light atoms such as H, C, N and O. In fact, typical frozen-hydrated specimens are

³ Together with the complexity of the systems under investigation, this is the major reason for the discrepancy between TEM in biology and in materials science, where today image resolutions of up to 0.05 nm are reached (<http://ncem.lbl.gov/TEAM-project>).

almost entirely transmissive to the electron beam. The fraction of contrast generated by attenuation of the wave amplitude (“amplitude contrast”), originating predominantly from interception of high angle scattering by apertures, is in the order of only 7% (Toyoshima and Unwin 1988). Although the cancelling of inelastic electrons by means of an energy filter can slightly increase the amplitude contrast, its contribution is still marginal. As a consequence, nearly the entire information about the biological scatterer is encoded in a distortion of the object exit wave front by a few degrees (fig. 1.1). Due to the large depth of focus (caused by the small numerical aperture of electron lenses) the 2D phase distribution of the exit wave represents a projection of the specimen's electrostatic potential.

As will be described in section 2.1.1, the exit wave phase distribution is converted into image contrast by interference of the scattered wave portion with the unscattered “reference” wave, which is therefore referred to as phase contrast. However, the detector image intensity does not directly reproduce the specimen projection but its convolution with the Fourier transform of the contrast transfer function (CTF), which is an instrument-specific function. In conventional TEM, the contrast transfer in dependence of the object frequency is sine-shaped, thereby producing negligible contrast for “phase objects” (such as frozen-hydrated samples) when they are imaged close to focus (fig. 1.2 C). Contrast is usually generated by intentional defocusing of the objective lens, but at the cost of a blurring of the image which reduces the attainable resolution further (fig. 1.2 D, E). Another consequence of the sine shaped CTF is an oscillating contrast transfer at high spatial frequencies, including transfer gaps and bands of alternating contrast (fig. 1.2 F, G). Conventional TEM imaging is thus always a trade-off between obtaining fine structural details with low contrast, or a rough object outline with stronger contrast (cf. fig 1.2 C and E).

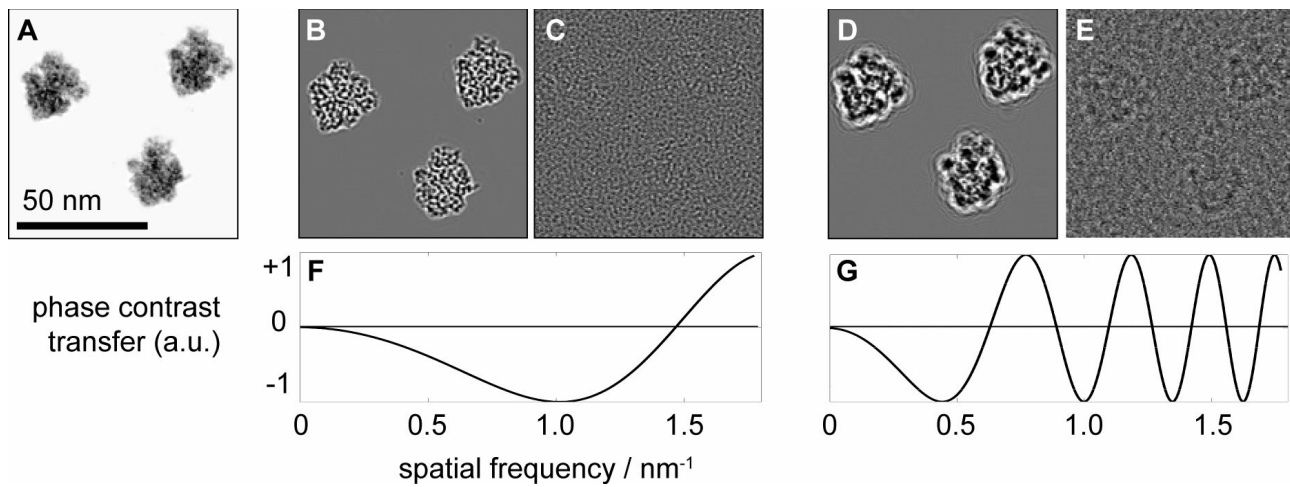


Figure 1.2.: Simulations showing the weak contrast of frozen-hydrated samples in TEM. (A) Model projections of ribosomes (EMD entry 1055) in vacuum. (B) Image contrast generated by a low underfocus (200 nm). (C) If ice embedding and 10% detector noise are included, the individual particles can hardly be localised in the image. (D, E) Images at 1 μm underfocus, assuming the same embedding and noise level as in C. Through stronger defocusing, contrast for low spatial frequencies is enhanced and the particles can be distinguished from noise in E. (F, G) The contrast transfer for defocused images contains gaps and contrast reversals, causing image artefacts as can be seen in D.

1.3 Phase plates: a solution for the weak contrast problem

To overcome the resolution limit of cryo TEM arising from the weak and artifactual contrast transfer of conventional defocused images, this thesis describes the development and application of in-focus phase contrast TEM using physical⁴ phase plates. A physical phase plate is placed in the back focal plane (BFP) of the objective lens, where scattered and unscattered waves are spatially separated (fig. 1.4 A). The phase plate imposes a relative phase shift of the two wave components, such that maximal phase contrast is generated in the image. The phase contrast in TEM images recorded with a phase plate is transferred as a cosine in frequency space as opposed to conventional imaging, where it is transferred with the sine. The sine-to-cosine transition of the CTF leads to

1. strong contrast for low spatial frequencies, as $\cos(0)=1$ and
2. a uniform, maximum phase contrast extending to the highest spatial frequencies for phase plate images recorded in focus, with no transfer gaps or contrast reversals.

⁴ The term “phase plate” is also sometimes used to describe the aberration disc, i.e. the 2D phase distribution of the electron wave in the BFP. To distinguish it from physical devices placed in the BFP to obtain in-focus phase contrast, which are described in this work, the more precise term “physical phase plate” is used in this thesis where necessary to avoid confusion. In the following, however, the short term “phase plate” will be used for preference.

As no blurring and other image artefacts occur, phase plate-mediated in-focus imaging yields optimal contrast for phase objects such as frozen-hydrated specimens (fig. 1.3). With the use of this technique, the weak contrast limitation in TEM of weak phase objects is removed.

The concept of the phase plate was formulated by Zernike (1936). It has been routinely used for decades in light microscopy where it is referred to as quarter-wave plate. In optical phase contrast microscopy, an additional 90° phase shift is applied to the unscattered beam so that it produces maximum image contrast when interfering with the scattered beam. In 1947, Boersch described implementations of the phase plate for TEM (Boersch 1947), using either the inner potential of a thin film or an electrostatic field, generated by a tiny electrode, to generate the necessary phase shift (fig. 1.4). For the latter, a possible technical implementation as a micrometer-sized electrostatic einzel lens was outlined by Matsumoto and Tonomura (1996), who referred to it as the Boersch phase plate. However, the demanding technical implementation of the micro-structured, complex device was not feasible at the time, and a proof of concept was not presented. In 1972, Unwin experimented with a simplified form of an electrostatic phase plate, which consisted of a thin, gold-coated spider web stretched over an objective aperture, intersecting the zero beam (Unwin 1972).

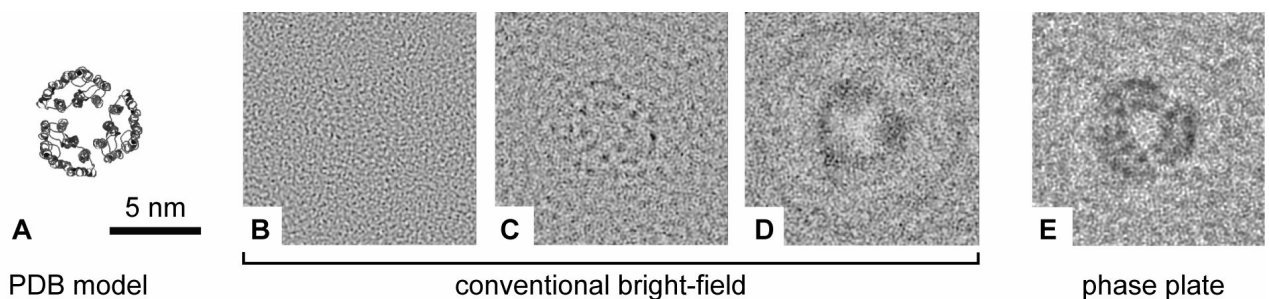


Figure 1.3.: Contrast enhancement by a phase plate for simulated images of the bacteriorhodopsin molecule complex. (A) PDB model. (B-D) images simulated by the software YaMS (Dinges et al. 1995; Müller et al. 2006) for typical conditions at 200 keV electron energy. The molecule of about 5 nm thickness is embedded in an ice layer of 11 nm thickness. Conventional bright field images in focus (B), near Scherzer focus (underfocus of $Z = 72$ nm, C) and at $Z = 2 \mu\text{m}$ underfocus (D) are characterised by poor contrast and extensive blurring, respectively. If contrast is generated by a phase plate (E), the bacteriorhodopsin is clearly visible in focus ($Z = 0$ nm).

The idea of the thin-film phase plate was revived by Nagayama and co-workers in the late 1990s (Danev and Nagayama 2001a, 2001b). They used amorphous carbon to produce thin films, and referred to the resulting device as the Zernike phase plate (fig. 1.4 B). Although a proof-of-principle

was soon obtained by this group, it is difficult to use such phase plates routinely for TEM imaging, owing to technical and practical difficulties. The most severe problem was rapid contamination and charging of the amorphous carbon layer, together with electron-matter interactions in the film that cause image artefacts and loss of coherence (Majorovits 2002; Nagayama 2006). Only recently, the first quantitative application study of a Zernike-type phase plate in biological TEM was published, after the contamination problem was partly solved by heating of the carbon film (Danev and Nagayama 2008).

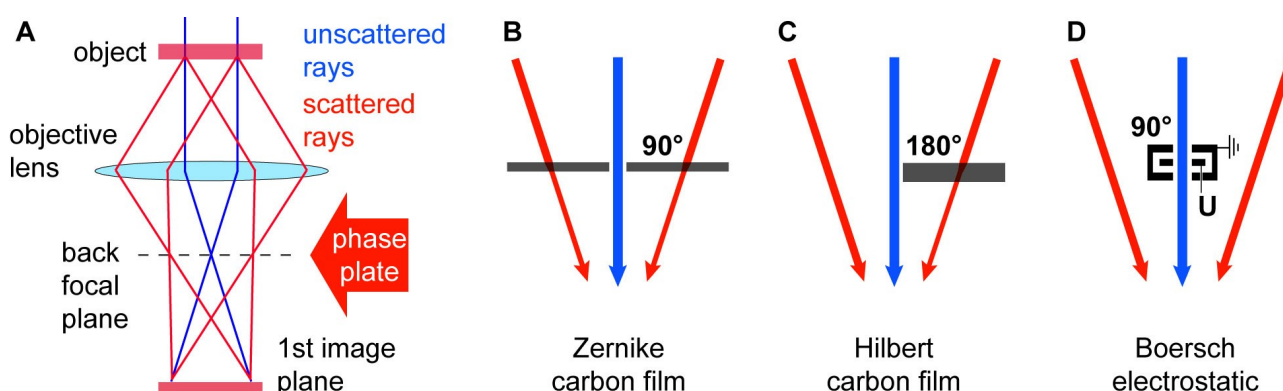


Figure 1.4.: (A) Schematic image formation in a TEM. In-focus phase contrast can be generated by placing a phase plate in the back focal plane, where scattered and unscattered wave portions are spatially divided. (B) Zernike phase plate. The scattered wave is shifted by $\pi/2$ or 90° when propagating through a thin carbon film with a mean inner electrostatic potential of ~ 10 V (Wanner et al. 2006). The unscattered zero beam passes through the central hole and remains unaffected. (C) Hilbert phase plate. The phase of one half-plane of the diffraction pattern is shifted by π or 180° , excluding the zero beam. The weakening of the wave vectors in B and C indicates a loss of coherent intensity caused by scattering of electrons in the carbon layer. (D) Boersch's electrostatic phase plate. The phase of the unscattered wave is shifted by $+90^\circ$ when passing through an electrostatic field trapped inside a micrometer-sized electrostatic einzel lens. The scattered rays pass outside the lens field, so that their phase remains unchanged.

A different type of thin-film phase plate, also adapted for TEM by the Nagayama group (Nagayama 2002), has been applied with somewhat less difficulty than the Zernike type in the meantime: the Hilbert phase plate (fig. 1.4 C). It simply consists of a half-plane of amorphous carbon film, and therefore is easier to align and manufacture. A number of qualitative biological studies using Hilbert phase plates were published since, showing strong phase contrast for specimens such as whole frozen-hydrated cyanobacteria (Kaneko et al. 2006) and cryo sections of cells (Kaneko et al. 2005; Setou et al. 2006). As will be described in more detail in section 2.2.2, Hilbert phase contrast gener-

ates an asymmetrical point image because of the non-rotational symmetry of the half-plane, which may be sometimes suitable for the human eye (Nagayama 2002). Nevertheless, it is an artefact, and the resulting image does not directly correspond to the projection of the specimen potential.

1.4 Which is the ideal implementation of in-focus phase contrast?

Although very impressive results have been achieved by the Nagayama group using carbon film Zernike- and Hilbert-type phase plates by largely solving the charging problem, the experiments still revealed a considerable drawback: elastic and inelastic interactions of the scattered electrons with the carbon film lead to loss of coherence, and thus to a lower signal. The transmissivity of carbon film was reported to be 72% for 300 keV electrons and a film thickness of 31 nm (Danev and Nagayama 2001b). This thickness is needed to generate the $\pi/2$ phase shift necessary for a Zernike phase plate. For the Hilbert phase plate a phase shift of π is required and thus the carbon film needs to be twice as thick. The transmissivity of 64 nm carbon films was reported to be 52% (Setou et al. 2006). However, because of the particular geometry of the Hilbert phase plate, this reduced transmission only occurs in one half-plane of the BFP⁵. Simulations using a multi-slice algorithm came to similar results for the transmissivity of thin carbon films (Majorovits 2002).

The problem of signal loss by carbon film phase plates becomes evident in a recent study (Danev and Nagayama 2008). The article compares the results of single particle reconstruction of a protein complex using in-focus Zernike phase contrast with the conventional defocus method. Although initial particle picking and the subsequent classification and averaging process was helped by the high contrast of individual particles, the resulting resolution was the same for Zernike and conventional reconstructions. This means that the advantage of the optimal $\cos(0)$ contrast generated by the phase plate is obviously cancelled by a decrease of SNR at high resolution. This undesired effect can be considered as an additional damping envelope of the CTF caused by incoherent interactions between the electrons and the carbon film.

It is clear from fig. 1.4 D that electrostatic phase plates avoids in principle the disadvantage of coherence loss. The required relative phase shift between scattered and unscattered wave is generated by an electrostatic field alone, so that outside the ring electrode no electron-matter interactions occur. An electrostatic phase plate is thus the ideal implementation of in-focus phase contrast, as it

⁵ It will be shown in section 2.2.2 that in fact the actual signal attenuation for the Hilbert phase plate will be always slightly lower than for the Zernike phase plate at a given electron energy.

allows to utilise the maximal object information that can be obtained with a given electron dose.

1.5 Goals of this work

The electrostatic phase plate is in theory the ideal technical implementation for in-focus phase contrast in TEM. However, more than 60 years after it was first described by Boersch, it has not been manufactured and applied to this date owing to its complexity and miniature dimensions. Thus, the first experimental questions to answer were:

- Can a Boersch-type phase plate, based on an electrostatic einzel lens having the required micrometer dimensions, be fabricated with state-of-the-art technology?
- Is the transition of the conventional sine CTF to a cosine CTF, enabling strong in-focus phase contrast, achieved using such a device in the back focal plane?
- What is the extent of information loss resulting from the obstruction of parts of the diffraction pattern by the einzel lens and its support? What is the ideal geometry of the device to minimise this information loss?

It is obvious that placing a physical electrostatic einzel lens in the centre of the BFP will intercept electrons passing close to the optical axis. This will cause the loss of low spatial frequencies in the image. For some applications that require high contrast of object features with dimensions >10 nm, e.g. CET, this signal loss cannot be tolerated. Thus, it is desirable to advance Boersch's concept of the phase-shifting electrode.

- Is it feasible to modify the TEM optics so that the effective loss of low spatial frequency signal, caused by the phase plate electrode, becomes negligible?

The central einzel lens is necessary to generate the spatially confined electrostatic field that shifts the phase of the unscattered wave, but in principle the presence of any absorbing material in the beam path is undesirable. An optimal phase plate would be perfectly transmissive, so that the full object information is transferred to the image with maximum contrast:

- Is it possible to realise a matter-free phase plate, consisting only of an inhomogeneous electrostatic field distribution in the BFP?

Experience shows that the Hilbert half-plane geometry (fig. 1.4 C) has practical advantages over the

rotational Zernike geometry (fig. 1.4 B): it needs to be aligned only in one direction in the BFP, whereas for a round phase plate the beam has to be aligned to the central hole in x and y. For a matter-free electrostatic implementation, using a half-plane geometry would simplify the technical design. To exploit these advantages, a method has to be found to convert the asymmetric Hilbert image contrast into a true projection of the specimen potential:

- Can the asymmetric Hilbert phase contrast be converted into strong isotropic contrast that yields a faithful projection image?
- Is in-focus Hilbert phase contrast applicable for electron tomography and CET? Are the resulting 3D reconstructions comparable, or even better, than those obtained by conventional ET?

1.6 A short overview of the contents

Chapter 2 describes the theory of image formation for phase objects, such as biological frozen-hydrated samples and especially thick samples. The instrumental limitations of conventional TEM are outlined in a more precise manner. The improved contrast generated by different types of phase plates is quantified and their further influence on image formation is considered.

The first technical implementation of Boersch's electrostatic phase plate is presented in **chapter 3**. More than 60 years after it was first described, the first experimental proof-of-principle for this “ideal” type of phase plate is given. The extent of signal loss caused by different einzel lens support architectures is quantified in simulations, and it is shown experimentally that a threefold symmetry is the best solution.

Exploiting the optimal signal transfer of the Boersch phase plate for biological applications requires a modification of the electron optics. **Chapter 4** outlines the recent PACEM microscope project, which enables the application of the Boersch phase plate for almost all fields of TEM, including biological cryo imaging and CET.

Chapter 5 describes a novel design of an entirely matter-free phase plate, consisting only of a highly inhomogeneous electric potential generated in the BFP. This “anamorphic” phase plate, of which a first technical implementation is presented, provides the advantages of an electrostatic phase plate, without the constraints of the Boersch phase plate.

Finally, an application study of in-focus phase contrast electron tomography, using the simple and therefore favourable Hilbert half-plane phase plate, is presented in **chapter 6**. The enhancement of image contrast for frozen-hydrated biological specimens is shown, and a method of transforming the resulting strong but an-isotropic contrast into faithful projection images is outlined. In two application studies, the enhanced SNR of 3D reconstructions by Hilbert phase plate ET is demonstrated in comparison to conventional tomography.

All experimental work described in this thesis was carried out at the Max-Planck-Institute of Biophysics in Frankfurt am Main, Germany. TEM Images were recorded with a SESAM II Cryo (Carl Zeiss NTS, Oberkochen, Germany) and a Tecnai G₂ Polara (FEI Company, Hillsboro, USA). The electrostatic phase plates (chapters 3 and 5) were fabricated at the Laboratorium für Elektronenmikroskopie at the University of Karlsruhe, Germany within the framework of a scientific collaboration. The PACEM project (chapter 4) is realised in collaboration with the company Carl Zeiss NTS within the cluster of excellency “macromolecular complexes” at the University of Frankfurt am Main.

2 Mechanisms of Contrast Formation in TEM

This chapter outlines the formation of electron-microscopic image contrast for weakly scattering objects. It shows that the assumption of a weak-phase object is justified also for thick biological objects, although they significantly reduce the amplitude of the incident wave. The physical background of different methods of phase contrast generation is described: phase contrast by defocusing, in-focus contrast by Zernike- and Hilbert-type phase plates and single-sideband imaging.

2.1 Principles of image formation

2.1.1 Electron scattering by weak-phase-weak-amplitude objects

In TEM, the object is illuminated by parallel rays, corresponding to a planar electron wave. The specimen exit wave can be generally written as

$$\psi_o(\mathbf{r}_o) = [1 - \hat{a}(\mathbf{r}_o)] \exp\{-i\eta(\mathbf{r}_o)\}, \quad (2.1)$$

with $\mathbf{r}_o = (x_o, y_o)$ denoting the coordinates in the object plane. $\hat{a}(\mathbf{r}_o)$ denotes the reduction of the wave amplitude by “loss” of electrons. This loss mainly consists of electrons scattered to high angles and intersectioned by apertures as well as inelastic scattering with subsequent cancelling by an energy filter. $\eta(\mathbf{r}_o)$ denotes the distortion of the plane wave front incident to the specimen, equal to the projection of the three-dimensional distribution of electrostatic potential ρ within the specimen of thickness t :

$$\eta(\mathbf{r}_o) = \frac{\pi}{\lambda U_0} \chi(U_0) \int_{z_o+t/2}^{z_o-t/2} \rho(\mathbf{r}_o, z) dz. \quad (2.2)$$

Here, z_o denotes the object plane (λ : electron wavelength, U_0 : acceleration voltage). The potential ρ is assumed to be proportional, or at least closely correlated, to the object mass density. The relativistic constant

$$\chi(U_0) = \frac{2(m_0 c^2 + eU_0)}{(2m_0 c^2 + eU_0)} \quad (2.3)$$

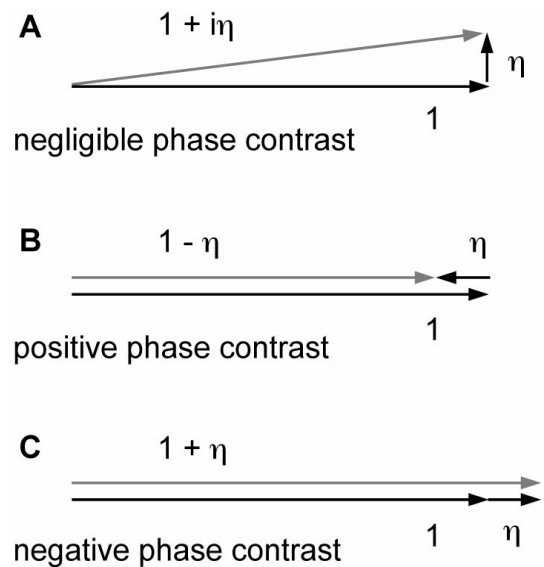
is ≈ 1.16 for $U_0 = 200$ keV (e , m_0 : electron charge and rest mass).

Typical biological objects, especially frozen-hydrated samples, are almost entirely transmissive to the electron beam. Thus, the amplitude modulation is significantly weaker than the phase modulation, i.e. $\eta/2\pi \ll \hat{a}$. Almost the entire information about the object structure is therewith encoded in the wave front distortion $\eta(\mathbf{r}_o)$. Furthermore, it has been shown that e.g. for protein embedded in vitrified ice, η is typically of the order of 5° ($1/36 \pi$) (Majorovits 2002), so that $\eta \ll 2\pi$. This imaging situation and its description is generally called the *weak-phase-weak-amplitude approximation*. For such a weak-phase object, the exit wave function is well approximated by

$$\psi_o(\mathbf{r}_o) \approx 1 - \left(\hat{a}(\mathbf{r}_o) - \frac{\eta(\mathbf{r}_o)^2}{2} \right) - i\eta(\mathbf{r}_o) = 1 - \underbrace{a(\mathbf{r}_o) - i\eta(\mathbf{r}_o)}_{\text{scattered wave}}. \quad (2.4)$$

Thus, within the approximation, the specimen exit wave can be regarded as the sum of an unscattered background, which is set to unity here, and a scattered portion $a - i\eta$. If the small amplitude contribution is neglected, the relative phase of the scattered wave η and the unscattered reference wave is $\pi/2$ or 90° , as expressed by the factor i . To obtain contrast for a weak phase object, an additional phase shift of $\pm\pi/2$ has to be added to the scattered wave, which is illustrated in fig 2.1.

Figure 2.1.: The elastic scattering of electrons in a weak phase object causes a phase shift of $\pi/2$ between the scattered and unscattered parts of the electron wave. The detected intensity (length of resulting vector) is almost the same as of the unscattered background, leading to a negligible phase contrast (A). Maximal phase contrast is achieved by an additional phase shift of $-\pi/2$ (positive phase contrast, B) or $\pi/2$ (negative phase contrast, C) between scattered and unscattered parts of the electron wave. Such a phase shift can be partly generated by defocusing of the objective lens, or ideally by using a physical phase plate.



2.1.2 The influence of aperture functions on image formation

As outlined in appendix A.2.2, propagation of the specimen exit wave to the back focal plane of the

objective lens is equivalent to inverse Fourier transformation of (2.4). The wave function ψ_a in the BFP is then

$$\psi_a(\mathbf{k}) = \delta(\mathbf{k}) - \tilde{a}(\mathbf{k}) - i\tilde{\eta}(\mathbf{k}). \quad (2.5)$$

Here, $\mathbf{k}=(k_x, k_y)$ is the coordinate in the BFP, and $|\mathbf{k}|=k$ is called the spatial frequency. $\tilde{g}=F^{-1}(g)$ denotes the inverse Fourier transform of a function g , and δ is the two-dimensional Dirac Delta distribution. The effect of the lens aberrations (see appendix A.1.4), apertures and other effects that only depend on the spatial frequency can now be expressed by multiplication by an aperture function $G(\mathbf{k})$:

$$\hat{\psi}_a(\mathbf{k}) = [\delta(\mathbf{k}) - \tilde{a}(\mathbf{k}) - i\tilde{\eta}(\mathbf{k})] G(\mathbf{k}) \quad (2.6)$$

Written in the very general form

$$G(\mathbf{k}) = \tilde{B}(\mathbf{k}) \exp(iP(\mathbf{k})), \quad (2.7)$$

the phase P of the aperture function may include lens aberrations and phase plates that effect the phase of ψ_a . The amplitude \tilde{B} contains obstructing elements such as apertures or attenuation by thin films, as will be outlined later.

Fourier transformation of (2.6) yields the image wave,

$$\psi_i(\mathbf{r}_i) = B(0) - F[\tilde{a}(\mathbf{k}) + i\tilde{\eta}(\mathbf{k})] G(\mathbf{k}). \quad (2.8)$$

It is useful at first to calculate the detectable image intensity for an arbitrary aperture function G , especially for one that is not necessarily rotationally symmetric. Therefore, a well-suited approach made by Danev and Nagayama (2004) will be followed, in which the image wave is written as

$$\psi_i(\mathbf{r}_i) = B(0) - \epsilon(\mathbf{r}_i) \quad (2.9)$$

with

$$\epsilon(\mathbf{r}_i) = F\left[\left[\tilde{a}(\mathbf{k}) + i\tilde{\eta}(\mathbf{k})\right] B(\mathbf{k}) \exp\{iP(\mathbf{k})\}\right]. \quad (2.10)$$

The image intensity $I=|\psi_i|^2=\psi_i^* \psi_i$ is then

$$I(\mathbf{r}_i) = B^2(0) - \underbrace{2B(0) \Re \epsilon(\mathbf{r}_i) + \epsilon^2(\mathbf{r}_i)}_{\text{object contrast}}. \quad (2.11)$$

The term ϵ^2 contains only contributions of the orders a^2 , η^2 and $a\eta$, which are all negligibly

small. The contrast $\Re \epsilon$ is equal to the convolution ($*$) of the object amplitude and phase signal with the amplitude and phase point spread functions (PSFs):

$$\Re \epsilon(\mathbf{r}_i) = a(\mathbf{r}_i) * aPSF(\mathbf{r}) + \eta(\mathbf{r}_i) * pPSF(\mathbf{r}). \quad (2.12)$$

2.1.3 The general contrast transfer functions

The amplitude and phase of the aperture function, which are both real, can be expressed as sums of symmetric functions B_S, P_S and anti-symmetric functions B_A, P_A :

$$\begin{aligned} B(\mathbf{k}) &= B_S(\mathbf{k}) + B_A(\mathbf{k}) \\ P(\mathbf{k}) &= P_S(\mathbf{k}) + P_A(\mathbf{k}). \end{aligned} \quad (2.13)$$

Thus, (2.10) can be rewritten as

$$\epsilon(\mathbf{r}_i) = F \left[\left[\tilde{a}(\mathbf{k}) + i \tilde{\eta}(\mathbf{k}) \right] \left[B_S(\mathbf{k}) + B_A(\mathbf{k}) \right] \exp\{i P_S(\mathbf{k})\} \exp\{i P_A(\mathbf{k})\} \right]. \quad (2.14)$$

The Fourier transform of symmetric functions (S) is always real, while for anti-symmetric functions (A) it is always imaginary. Thus, in the image contrast $\Re \epsilon$, only the combinations SS , AA and iAS will survive. Substitution of (2.14) into (2.11) finally yields the image of a weak-phase object for an arbitrary phase and amplitude aperture function

$$I(\mathbf{r}_i) = B^2(0) - 2 B(0) F[S(\mathbf{k})], \quad (2.15)$$

with the image spectrum

$$\begin{aligned} S(\mathbf{k}) &= \tilde{a} \left[B_S \cos P_S + i B_A \sin P_S \right] \exp(i P_A) \\ &+ \tilde{\eta} \left[B_S \sin P_S - i B_A \cos P_S \right] \exp(i P_A). \end{aligned} \quad (2.16)$$

In other words, the transfer of the specimen's amplitude and phase information, a and η , by the microscope is modulated by the *amplitude* and *phase contrast transfer functions*

$$\begin{aligned} aCTF(\mathbf{k}) &= \left[B_S \cos P_S + i B_A \sin P_S \right] \exp(i P_A) \\ pCTF(\mathbf{k}) &= \left[B_S \sin P_S - i B_A \cos P_S \right] \exp(i P_A), \end{aligned} \quad (2.17)$$

which depend on the explicit form of the aperture function. It should be noted that the phase signal $\tilde{\eta}$ is directly proportional to the specimen density, while the amplitude \tilde{a} scales with the logarithm. It has been shown that the phase contrast is 20-40 times more efficient than amplitude contrast (Henderson 2005). Thus, for typical thin, unstained specimens the image contrast (phase contrast) is given by the pCTF alone.

2.1.4 The relation between contrast and SNR

It is worth noting that the image SNR directly depends on the CTFs:

$$SNR = \frac{\sigma(\text{signal})}{\sigma(\text{noise})} \approx \frac{2\hat{A}}{\sigma\{N(\mathbf{r}_i)\}} \frac{1}{n} \sum_{\mathbf{r}_n} |F[S(\mathbf{k})]|. \quad (2.18)$$

Here, Σ denotes the summation over a number n of discrete image pixels at \mathbf{r}_n (σ : 2D standard deviation, $N(\mathbf{r}_i)$: arbitrary image noise distribution). Another expression given by Reimer (1984) relates the SNR to the required dose q , attainable resolution d and the contrast:

$$SNR = 2 F[S(k)] d \sqrt{\frac{q}{e}}. \quad (2.19)$$

2.1.5 Image formation for thick biological objects

Objects investigated in CET, typically consisting of organic material embedded in vitrified ice, may have a thickness up to 500 nm⁶. The attenuation of the beam by such specimens is considerable, predominantly resulting from inelastic scattering and subsequent energy filtering. Furthermore, it is not clear whether the phase distortion of the exit wave is still small, as in the case of a weak-phase object. The exit wave of a thick object may be written in the general form

$$\psi(\mathbf{r}) = A(\mathbf{r}) \exp\{-i\eta(\mathbf{r})\}, \quad (2.20)$$

where \mathbf{r} is used for simplicity instead of \mathbf{r}_o .

Simulations show that the phase shifting potential (or electron refractive index) $\eta' = d\eta/dz$ for the organic material (e.g. protein) and the vitrified ice embedding is very similar. Majorovits (2002) gives a value of 2.18°/nm for protein and 1.96°/nm for vitreous ice, so that $\Delta\eta' = 0.22^\circ/\text{nm}$. The total phase distortion of the plane incident wave after passage through the specimen is then

$$\eta(x, y) = \int_{+t/2}^{-t/2} \Delta\eta'(x, y, z) dz. \quad (2.21)$$

For a specimen of thickness $t = 500$ nm, the phase shift could theoretically be as large as 110°, but only in the very unrealistic case that the organic material is arranged in “columns” along the beam axis z . The results of a simulation for a more realistic object are shown in fig. 2.2. The organic

⁶ CET has been applied on frozen-hydrated specimens of up to 1 μm thickness. However, the beam attenuation is so strong for such objects that they usually cannot be reconstructed in great detail.

material, consisting of lipid membranes, protein particles and vesicles inside a schematic “cell” is distributed almost homogeneously. It is shown that even for an object of 500 nm thickness which is embedded in vitreous ice, the projection $\eta(\mathbf{r})$ will have values in the range of 4-8°. In any case, the exit wave front can be thought of as the superposition of a uniformly phase shifted plane wave and a slightly distorted wave, $\hat{\eta}(\mathbf{r}) = \hat{H} + \eta(\mathbf{r})$. Without loss of generality, the “global” phase \hat{H} can then always be set to zero, as it applies to both scattered and reference wave. Therewith, the approximation $\eta \ll 2\pi$ is justified even for a thick frozen-hydrated specimen, so that the exit wave phase can be written as

$$\exp\{-i\eta(\mathbf{r})\} \approx 1 - i\eta(\mathbf{r}) - \frac{\eta^2(\mathbf{r})}{2}. \quad (2.22)$$

On the other hand, the wave amplitude will decrease exponentially with the specimen thickness. The factor A in (2.20) generally quantifies incoherent electron-specimen interactions such as inelastic scattering and absorption by thick objects, but also high angle scattering high angle and cancelling by an aperture. In fig. 2.2, the simulation result for the exit wave amplitude distribution is shown. It was assumed that that the mass densities scale with η , and that the wave amplitude is reduced to 1/e by a 500 nm thick ice layer. It is shown that despite a mean global amplitude reduction to 37%, the lateral amplitude variations are very small ($\sigma[A(\mathbf{r})] = 0.006$). With this assumption, the exit wave amplitude can be rewritten as the sum of a constant, global amplitude reduction \hat{A} and a small lateral variation $a(\mathbf{r}) \ll 1$:

$$A(\mathbf{r}) = \hat{A} + a(\mathbf{r}) \quad (2.23)$$

Finally, the exit wave of a thick biological specimen can be rewritten as

$$\psi(\mathbf{r}) \approx [\hat{A} - a(\mathbf{r})] \left[1 - i\eta(\mathbf{r}) - \frac{\eta^2(\mathbf{r})}{2} \right] \approx \hat{A} \left[1 - \frac{a(\mathbf{r})}{\hat{A}} - \frac{\eta^2(\mathbf{r})}{2} - i\eta(\mathbf{r}) \right] \quad (2.24)$$

if terms of the order $a\eta$ and $a\eta^2$ are neglected. Apart from the constant amplitude factor A , (4) is equivalent to the weak-phase-weak-amplitude approximation for thin objects described in section 2.1.2. It is possible that (2.23) does not hold for the entire field of view, i.e. if $A(\mathbf{r})$ contains “steps”. An example is a dense cell located next a “void” region with nothing but ice. For such a case, the field of view can always be split up in sub-regions where (2.23) can be applied. The entire image is then formed from superposition of the sub-images, using different \hat{A}_n , and thereby

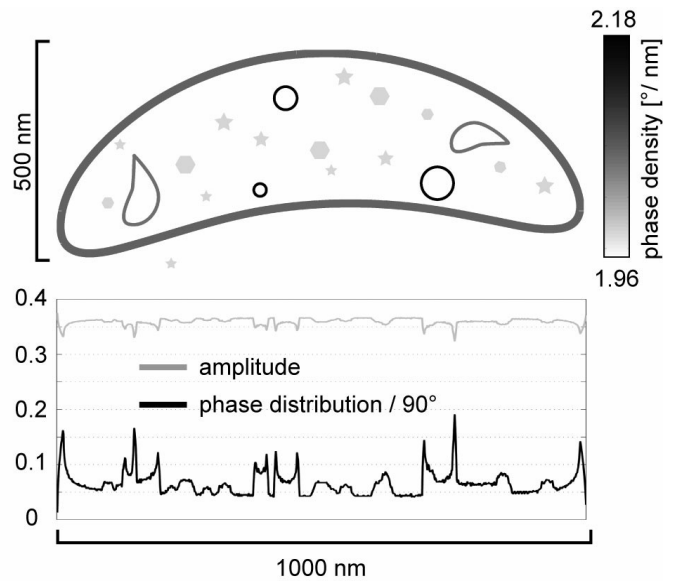
retrieving the original amplitude distribution.

Analogous to the weak-phase-weak-amplitude approximation, the image intensity for a thick object is thus

$$I(\mathbf{r}_i) = \hat{A}^2 - 2\hat{A} F[S(\mathbf{k})]. \quad (2.25)$$

Here, $F[S(\mathbf{k})]$ is again the 2D Fourier transform of the image spectrum $S(\mathbf{k})$. In contrast to the weak object case, the amplitude and phase object structure factors are now $\tilde{a}(\mathbf{k}) = F[a(\mathbf{r})/\hat{A}] - F[\eta^2(\mathbf{r})/2]$ and $\tilde{\eta}(\mathbf{k}) = F[\eta(\mathbf{r})]$, respectively.

Figure 2.2.: Simulation of the exit wave of a schematic “cell” embedded in vitrified ice, which is similar to objects investigated in cellular CET. The drawing indicates the protein density distribution (grey levels = 1.96 - 2.18 °/nm) in the ice layer (white = 1.96 °/nm) (Majorovits 2002). The phase (black curve) and amplitude (grey curve) modulation of a plane incident wave is calculated after passing through an z-x-section of the 500 nm thick object. Despite the thickness of the specimen, the variance of the amplitude and the distortion of the exit wave phase are comparably small. Phase and amplitude can be written as the sum of a larger, constant modulation and a small variance $\eta(\mathbf{r})$ and $a(\mathbf{r})$, respectively, justifying the treatment of such thick ice-embedded specimens as weak-phase objects (see text). For the amplitude modulation, the contrast thickness at which the value drops to 1/e is assumed to be 500 nm, which agrees with experimental observations.



2.1.6 Defocus phase contrast

In conventional TEM, no anti-symmetric apertures or phase shifts are present, i.e. $P_A = B_A = 0$ in (2.17), so that the $pCTF = B_S \sin P_S$. The phase of the $pCTF$ is equal to the wave aberration (cf. appendix A.1.4):

$$P_S(k) = W(k) = -\frac{\pi}{2} (2Z\lambda k^2 - C_S \lambda^3 k^4) \quad (2.26)$$

(Z : defocus, C_S : spherical aberration coefficient). Usually, B_S is represented by an objective aper-

ture diaphragm of radius R , which cancels all rays intersecting the BFP at distances $k_0 > R / \lambda f$. Thus, the conventional phase contrast transfer function is

$$pCTF(k) = \begin{cases} \sin W(k) & k \leq k_0 \\ 0 & k > k_0. \end{cases} \quad (2.27)$$

To obtain significant contrast in the image, the objective lens excitation is intentionally weakened, so that a plane lying above the object plane by the distance Z is imaged. This imaging condition is called *underfocus*⁷ ($Z > 0$). With this, the image of a phase object becomes a dark outline on light background, showing maximal contrast for spatial frequencies where $W(k) \approx \pi/2$. Given by the fact that the conventional pCTF is a sine, low spatial frequencies, containing information about “macroscopic” features of the object such as its size, overall shape and density, are transferred with very low contrast.

The conventional $pCTF$ is plotted in fig. 2.3 for various amounts of underfocus. C_s has a positive value for all round electron lenses. An “optimal” underfocus can be chosen so that within a broad spectral band, $W \approx \pi/2$ and thus $pCTF \approx 1$. This value, $Z_{sch} = \sqrt{\lambda C_s}$, is called *Scherzer focus*. However, for biological TEM this condition is far from being the best choice: The resulting contrast is less than 50% at all spatial frequencies below $1 / 1.07 \text{ nm}$ for a typical TEM (200 kV, $C_s = 2.2 \text{ mm}$). This means that structures like lipid membrane vesicles or the outline of protein molecules, with dimensions of 10 – 100 nm, cannot be visualised.

High contrast transfer for low resolutions is essential for TEM in biology and many other fields, so that conventional bright field imaging requires a high underfocus. Typical applied values range from a few 100 nm in single particle TEM and electron crystallography to 10 – 15 μm in electron tomography. However, the rapidly oscillating underfocus $cPCTF$ contains signal transfer gaps and contrast reversals (fig. 2.3). Furthermore, due to the non-linearity of the image recording step (2.11) and the high noise level, the image signal cannot be restored close to the $pCTF$ zeros. As $\sin W(k) \rightarrow 0$ for $k \rightarrow 0$, low resolution signal is quenched also for high defocus.

In aberration-corrected TEMs, not only the defocus Z , but also the spherical aberration coefficient C_s is an adjustable parameter, at least within some instrumental limits. However, a variable C_s

⁷ The underfocus condition is used rather than its opposite (“overfocus”, $Z < 0$). Its black-on-white contrast adds up with small portions of amplitude contrast that originate from the square phase term in (2.4). In some applications, like electron tomography, the specimen may also generate amplitude contrast, especially by filtering of inelastically scattered electrons; this signal will always have a positive sign.

does not provide an improvement for the problem of vanishing contrast for low spatial frequencies, as the spherical aberration term in (2.26) is almost negligible for $k < 1/(1 \text{ nm})$.

2.1.7 The damping of the contrast transfer function

During the calculation of contrast transfer for a weak-phase-weak-amplitude specimen, it was assumed that the specimen is illuminated by a perfect mono-energetic plane wave that travels exactly along the optical axis. In practice, imperfections of the condenser lenses, a small but finite size of the electron emitting tip and a small energy spread of the electron beam have to be considered. Just like the lens aberrations, those imperfections are treated as perturbations of the idealised imaging process.

It can be assumed that both the energy spectrum of the electron beam and the radial distribution of emission current around the centre of the source tip are Gaussian distributions. In this case, the effect of chromatic imperfections can be expressed as an envelope of the contrast transfer function. Using the reduced spatial frequency $Q = (C_s \lambda^3)^{1/4} k$ and reduced defocus $D = Z / (C_s \lambda)^{1/2}$, the chromatic *aCTF* and *pCTF* can then be written as

$${}^a_p CTF_c(Q) = {}^a_p CTF(Q) \underbrace{\exp\left\{-\frac{\pi^2}{2} A^2 Q^2 (D - Q^2)^2\right\}}_{K_s} \underbrace{\exp\left\{-\frac{\pi^2}{4} B^2 Q^2 (A^2 + Q^2)\right\}}_{K_t}. \quad (2.28)$$

K_s and K_t are the envelope functions due to limited spatial and temporal coherence, respectively, with

$$A = \alpha_c \left(\frac{4C_s}{\lambda} \right)^{1/4} \quad \text{and} \quad B = \frac{\gamma C_c v_m}{U_0 (\lambda C_s)^{1/2}} \quad (2.29)$$

(α_c : condenser aperture angle, v_m : FWHM of beam energy spectrum, C_c : chromatic aberration coefficient, $\gamma = (1 - v^2/c^2)^{-1/2}$ with electron velocity v).

If U , C_s and C_c are considered as unchangeable instrumental parameters, high resolutions can be achieved by applying a small condenser aperture radius, a small tip size and a narrow energy spread of the illumination beam. This is realised on one hand by using field emission guns (FEGs), where the electron beam is extracted from a tip region consisting only of a small number of atoms. On the other hand a monochromator can be positioned prior to the condenser lens system selecting

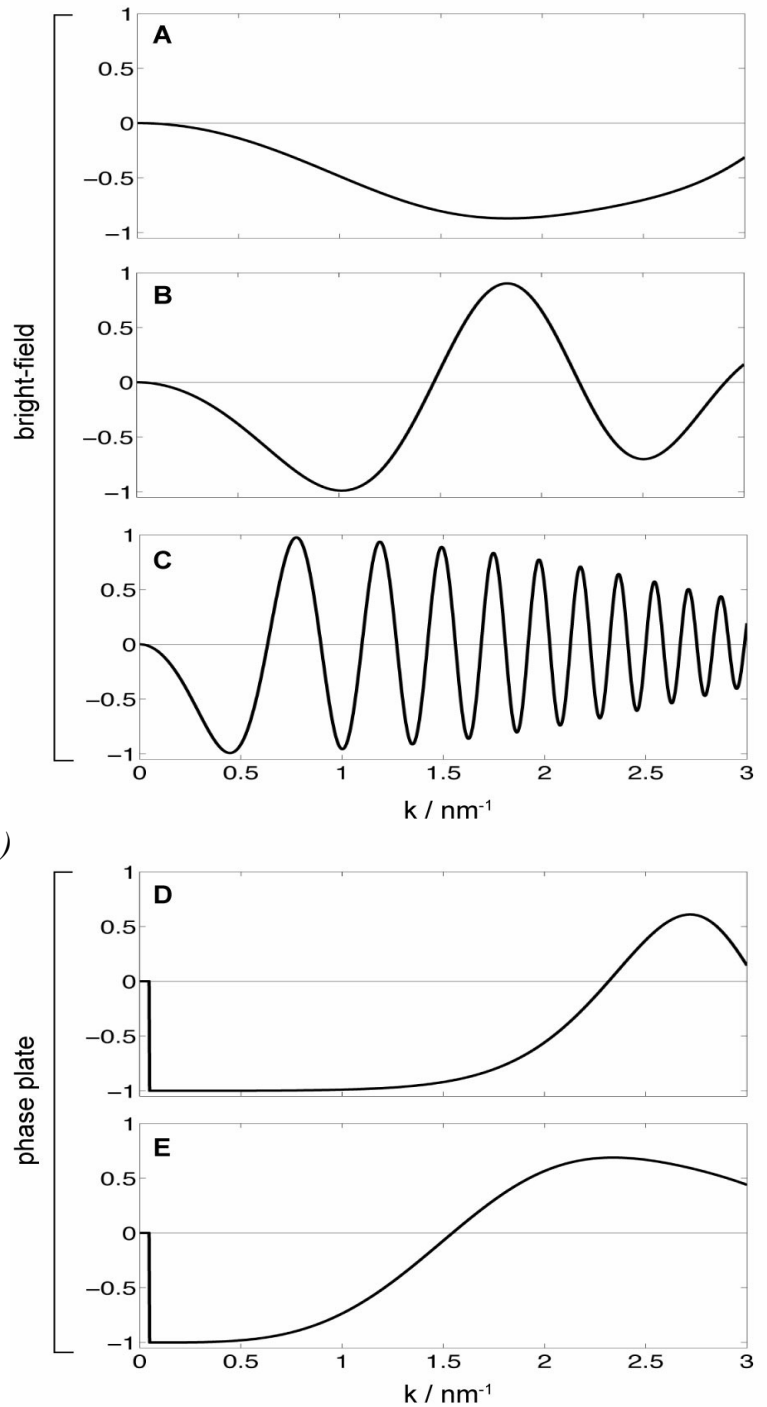
a narrow part of the spectrum by means of a small slit inside a highly energy-dispersive plane. With state-of-the-art aberration correction technology, in principle all of the parameters defining the damping functions have become tuneable, although a combined corrector system for the spherical and chromatic aberrations is at present still in a stage of development (Rose 2004, 2005; Haider and Müller 2004).

By the help of the contrast transfer theory and the expressions of the damping envelope, a definition for the optical resolution of the instrument can be given.

Instrumental resolution: Spatial frequencies that are faithfully transferred to the image with significant contrast, e.g. $\max\{k : CTF(k) > 1\}$

Information limit: Falloff of the combined exponential damping functions of the CTF, e.g. $\max\{k : K_s K_t > 1/e\}$.

Figure 2.3.: Phase contrast transfer functions (pCTFs) for a 200 kV TEM ($f=3.0$ mm, $C_s=2.2$ mm, $C_c=3.4$ mm). The energy spread of the electron beam was assumed to be $\Delta E = 1$ eV. A damping of the pCTF at high spatial frequencies according to (2.28) was assumed. (A-C) Conventional bright field pCTFs. The contrast transfer is oscillating and approaching zero for low resolution. (A) Underfocus $Z=72$ nm (Scherzer defocus). (B) $Z=200$ nm. (C) $Z=1,000$ nm. (D,E) pCTFs of the same TEM equipped with a phase plate (Zernike or Hilbert-type). A hole radius of the Zernike phase plate of 0.38 μm , corresponding to the edge distance of the Hilbert phase plate from the central beam, was assumed. For spatial frequencies $>1/(20.1$ nm), the pCTF is transferred from a sine to a cosine. (D) Gaussian focus ($Z=0$). (E) ($Z=100$ nm) A slight underfocus leads to oscillations of the cosine pCTF. However, for resolutions below $1/(1$ nm) the contrast transfer is still close-to-optimal.



2.2 In-focus phase contrast generated by physical phase plates

2.2.1 Zernike-type phase plates

The Zernike phase plate or $\lambda/4$ plate is a method that is routinely used in light microscopy to enhance the in-focus phase contrast. The principle of this technique is a thin piece of a light refractive material, which is positioned at the focal spot in the BFP of the objective. The thickness of the material is chosen so that the phase of the wave function at $k=0$, corresponding to the unscattered light, is advanced by $\approx\pi/2$ or 90° .

An analogous phase plate for TEM has been first implemented by Nagayama and co-workers (Danev and Nagayama 2001b) in the 1990s, and is also referred to as the Zernike phase plate. A thin layer of amorphous carbon film with a tiny hole, typically $1\ \mu\text{m}$ in diameter, is inserted in the back focal plane of the objective lens. Its surface is oriented perpendicular to the electron beam and the hole aligned with the optical axis (fig. 2.4 B). The intense zero beam of unscattered electrons (“focal spot”) passes through the hole and remains unaffected. The scattered wave, represented by rays that intersect the BFP at a distance $r = k\lambda f$ to the optical axis, passes through the carbon film.

When passing through the carbon layer of thickness t , the electrons are exposed to a positive mean electrostatic potential U_i . Caused by the change in total energy, the phase of the electron wave is thereby advanced by an amount

$$\varphi(t) = \pi \chi(U_0) \frac{U_i t}{U_0 \lambda} . \quad (2.30)$$

Different values for the mean potential U_i can be found in the literature. While Reimer gives a value of $+7.8\ \text{V}$ (Reimer 1984), recent publications report a potential of $U_i = +10.7\ \text{V}$ (Harscher and Lichte, 1998; Wanner et al., 2006). For an acceleration voltage of $U_0 = 200\ \text{kV}$, this results in a carbon film thickness of $20.2\ \text{nm}$ to obtain a phase shift of 90° .

The phase plate changes the symmetric phase of the aperture function (2.7) to $B_s = W(k) + \varphi(t)$. Again, there are no anti-symmetric contributions. The phase contrast transfer function for a Zernike phase plate of thickness t is

$$pCTF_Z(k, t) = \begin{cases} \sin \{W(k) + \varphi(t)\} & k \geq k_0 \\ \sin W(k) & k < k_0, \end{cases} \quad (2.31)$$

with $k = R/\lambda f$ (R : hole radius). For perfect Zernike phase contrast (ZPC) with $\varphi(t_{\pi/2}) = -\pi/2$, the $pCTF$ simplifies to

$$pCTF_Z(k) = \begin{cases} \cos W(k) & k \geq k_0 \\ \sin W(k) & k < k_0. \end{cases} \quad (2.32)$$

A ZPC image in Gaussian focus ($Z=0$) yields continuous maximal phase contrast at all resolutions relevant for biological TEM. As plotted in fig. 2.3, the Zernike $pCTF$ has a value $> 50\%$ for all spatial frequencies up to $1/(2 \text{ nm})$ for a 200 kV microscope with $C_s = 2.2 \text{ mm}$.

Apart from the desired phase shift, incoherent inelastic and multiple elastic scattering of electrons by the carbon film lead to a loss of coherent elastic signal (Majorovits, 2002; Danev and Nagayama, 2008). The electron loss $1 - a_0(t)$ can be quantified in a modulation $a_0(t_{\pi/2}) = a_Z$ of the wave amplitude $B_s(k \geq k_0)$ in the BFP. Considering those ‘‘absorption effects’’, the real $pCTF$ becomes

$$pCTF_Z^{(a_Z)}(k) = \begin{cases} a_Z \cos W(k) & k \geq k_0 \\ \sin W(k) & k < k_0. \end{cases} \quad (2.33)$$

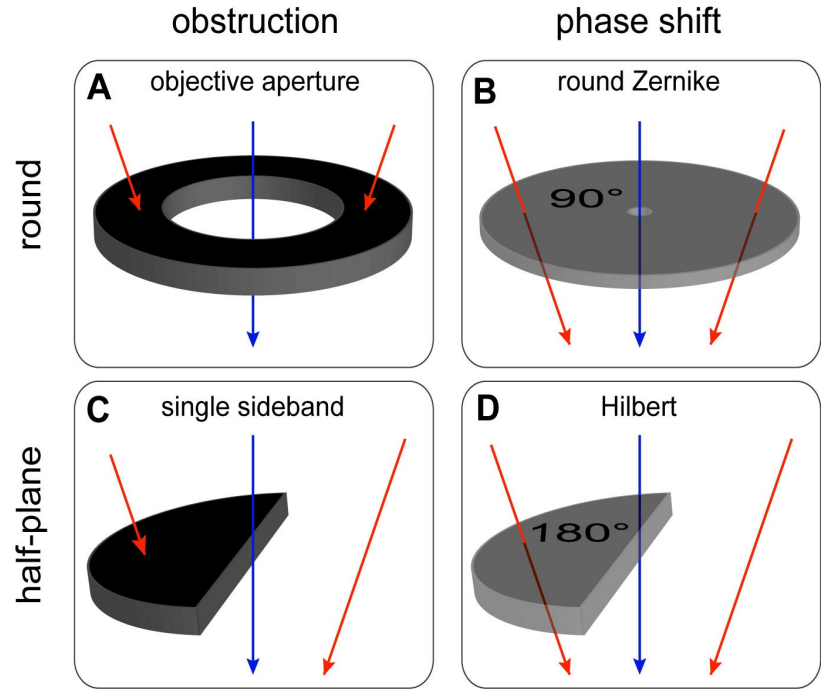
In practice, the fabrication process will not yield the exact film thickness $t_{\pi/2}$ necessary to obtain the phase shift by $\pi/2$. Likewise, it may not be possible to find the ideal Gaussian focus $Z=0$ for image acquisition. Therefore, it is interesting to consider the effect of small film thickness and focus variations of the ZPC contrast transfer:

$$\Delta pCTF_Z = \cos \left[\frac{\pi}{2} \left(C_s \lambda^3 k^4 - 2\lambda k^2 \Delta Z + \Delta t / t_{\pi/2} \right) \right]. \quad (2.34)$$

Deviations of the two parameters are largely uncritical for resolutions $< 1/(1 \text{ nm})$, which includes all relevant spatial frequencies e.g. for electron tomography. Due to the cosine-functionality of the $pCTF_Z$, thickness variations of 25% still yield $>90\%$ contrast in within this resolution range. The contrast transfer is somewhat more sensitive to focus variations: the defocus has to be kept $< 100 \text{ nm}$ to hold the contrast above 90%⁸.

⁸ All values are calculated for a 200 kV TEM with $C_s=2.2 \text{ mm}$. However, the considerations hold for most commercial TEMs used in biology.

Figure 2.4.: Aperture functions $G(\mathbf{k})$ to generate bright-field, Zernike, single sideband and Hilbert phase contrast: (A) Conventional bright-field imaging with a diffraction aperture. (B) Zernike phase plate. (C) Single-sideband aperture. (D) Hilbert phase plate.



2.2.2 Topographic in-focus contrast by Hilbert-type phase plates

The Hilbert phase plate also has its equivalent in light optics, the *Nomarski* or *differential interference contrast* (DIC) technique. As the Zernike phase plate, it was first described for TEM by Nagayama and Danev. The technique is referred to as Hilbert phase contrast (HPC), as it involves an optical Hilbert transform (Nagayama, 2002). The principle of the HPC consists in adding a constant phase of $-\pi$ or -180° to one half-plane ($k_x > 0$) of the diffraction pattern, excluding the zero beam (fig 2.4 B). Together with the lens aberration, the phase of the aperture function is then

$$P(\mathbf{k}) = W(k) + \pi H(k_x), \quad (2.35)$$

with the Heaviside step function $H(k_x)$. The latter can be expressed in terms of the sign function:

$H(k_x) = 1/2 \text{sign}(k_x) + 1/2$. This results in a representation of the phase by symmetric and anti-symmetric terms P_S and P_A

$$P(\mathbf{k}) = \underbrace{W(k) + \frac{\pi}{2}}_{P_S} + \underbrace{\frac{\pi}{2} \text{sign}(k_x)}_{P_A}. \quad (2.36)$$

For an “ideal” Hilbert phase plate, The loss of coherence from the carbon film is neglected, i.e.

($B_S=1$ and $B_A=0$). Substituting (2.36) and into the general $pCTF$ (2.17) then yields the Hilbert $pCTF$:

$$\begin{aligned} pCTF_H(\mathbf{k}) &= \exp\left\{-i \frac{\pi}{2} \text{sign}(k_x)\right\} \sin\{W(k) + \pi/2\} \\ &= -i \text{sign}(k_x) \cos W(k). \end{aligned} \quad (2.37)$$

The Hilbert $pCTF$ is equal to a cosine, with an additional multiplication of structure factors $\tilde{\eta}(\pm\mathbf{k})$ by $\mp i$. Due to the sine-to-cosine transformation of the $pCTF$, the Hilbert phase plate produces particularly strong contrast for low spatial frequencies (see fig. 6.3). The form of the $pCTF$, i.e., the contrast transfer, is equivalent to that of the Zernike phase plate described in section 2.2.1. However, caused by the $\text{sign}(k_x)$ modulation, the resulting image PSF is anti-symmetrical. As shown in the experimental Hilbert images in chapter 6, this leads to a pseudo-topographic object image. The image appears similar to a landscape that is illuminated from one side, the illumination direction determined by the direction of the phase plate.

The loss of coherent electrons $1-a_H$ by scattering processes during the passage of the beam through the carbon film, $1-a_H$ with $a_H=a_0(t_\pi)$, can be written as an aperture function

$$\begin{aligned} B(\mathbf{k}) &= a_H + (1-a_H)H(k_x) \\ &= \underbrace{\frac{1+a_H}{2}}_{B_S} + \underbrace{\text{sign}(k_x) \frac{1-a_H}{2}}_{B_A}. \end{aligned} \quad (2.38)$$

With symmetrical and anti-symmetrical contributions B_S and B_A , respectively. Therefore, if the signal loss is taken into account, the $pCTF$ (2.17) must be rewritten as

$$pCTF_H^{(a_H)}(\mathbf{k}) = -\frac{1+a_H}{2} i \text{sign}(k_x) \cos W(k) + \frac{1-a_H}{2} \sin W(k). \quad (2.39)$$

In practice, the edge of the half-plane will be positioned at some finite distance $d = \lambda f g$ from the centre of the diffraction pattern, to prevent charging and damage of the thin carbon film by the intense central beam (λ : electron wavelength, f : focal length of objective lens). Within the ‘‘gap region’’ $|k_x| \leq g$, the object signal is transferred as the sine of the wave aberration, as in conventional TEM.

If an image is acquired in Gaussian focus and the gap becomes infinitesimally narrow, i.e. $W \rightarrow 0$

and $g \rightarrow 0$, the Hilbert PCTF becomes

$$pCTF_H^{(Z, g \rightarrow 0)} = -i \operatorname{sign}(k_x) . \quad (2.40)$$

This holds for a resolution range where the spherical aberration term $1/2 C_s \lambda^3 k^4$ can be neglected. The anti-symmetric $\operatorname{sign}(k_x)$ artefact can be eliminated by multiplying the image Fourier transform with $i \operatorname{sign}(k_x)$. A numerically corrected in-focus HPC image represents a near-perfect projection of the object's phase shifting potential.

2.2.3 Comparison of coherence loss by Hilbert- and Zernike-type phase plates

The sine-to-cosine transition of the $pCTF$ obtained by carbon film phase plates is connected with a multiple scattering process, which affects object imaging, as in dynamic scattering. In addition, for carbon atoms inelastic scattering of electron is 3–4 times more probable than elastic scattering (Reimer 1984), which reduces the number of electrons available for coherent high-resolution imaging.

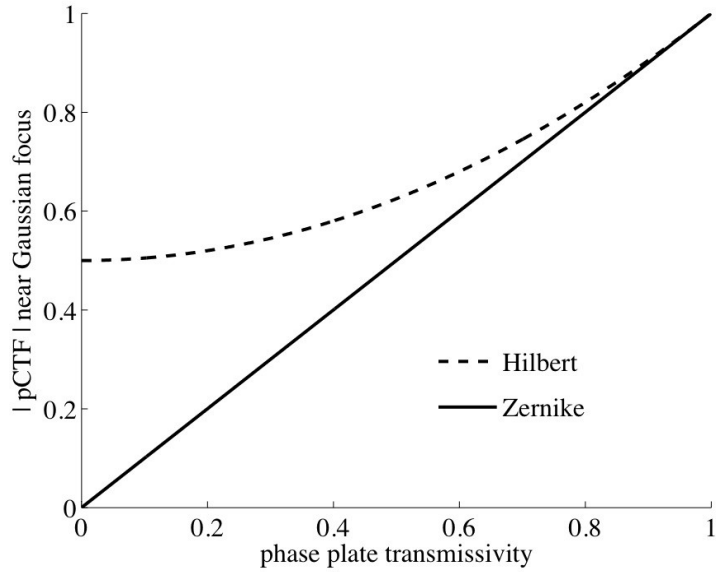
In the case of the Zernike phase plate, the loss of coherent electrons is described by the symmetric amplitude modulation $B_s(k > k_0) = a_0$. This is reflected by a simple attenuation of the $pCTF$ and thus the image signal, cf. (2.33). As the wave phase shift is proportional to the layer thickness, the Hilbert carbon film half-plane must be twice as thick as th

e Zernike film, $t_H = 2t_Z$. The amplitude of the scattered wave is decreased exponentially during the passage through the carbon film, i.e. $a_0(t) \propto \exp(-t / \tau)$. This results in a quadratic relation of the Zernike and Hilbert transmissivities: $a_0(t_H) = a_0^2(t_Z)$. The ratio of contrast transfer in focus ($W(k) \approx 0$) is thus

$$\frac{|pCTF_H|}{|pCTF_Z|} = \frac{1 + a_0^2}{2a_0} \geq 1 . \quad (2.41)$$

It is worth noting that the signal transfer by the Hilbert-type phase plate will always be higher than for the Zernike-type phase plate (fig. 2.5). This becomes most obvious in the extreme case of single-sideband contrast.

Figure 2.5.: Contrast transfer in Gaussian focus depending on the phase plate electron transmission, compared for Zernike- and Hilbert-type phase plates.



2.2.4 Single-sideband imaging

An important special case of Hilbert phase contrast is a half-plane which is completely obstructing the electron beam, i.e. $a_H=0$ in (2.39). This is called the single-sideband condition, as only one half of the diffraction pattern is used to generate the object image (fig. 2.4 C). The corresponding single-sideband pCTF, which can be easily calculated from (2.39), is

$$pCTF_{SSB}(\mathbf{k}) = -\frac{1}{2}i \text{sign}(k_x) \exp\{-i \text{sign}(k_x)W(k)\}. \quad (2.42)$$

Thus, single-sideband (SSB) image is a representation of the phase object, the contrast attenuated by $\frac{1}{2} \text{sign}(k_x)$ uniformly for all spatial frequencies. The phases of the structure factors $\tilde{\eta}(\mathbf{k})$ and shifted by an amount $-\text{sign}(k_x)W(k)$, depending on the wave aberration. If the wave aberration (defocus and C_S) and orientation of the half-plane is known, one can in principle obtain a “perfect” representation of the phase object from a single-sideband image by demodulating the amplitudes and phases in Fourier space with $-i \text{sign}(k_x)$ and $\text{sign}(k_x)W(k)$, respectively. The phase demodulation is obsolete for moderate resolutions if the image is acquired very close to Gaussian focus, so that $W(k) \rightarrow 0$. However, the SSB condition corresponds to a loss of 50% of coherently scattered electrons, which is reflected by the factor $\frac{1}{2}$ in (2.42). This is clearly a drawback for applications that are subject to a high level of noise and a limited electron dose, such as in biological cryo imaging.

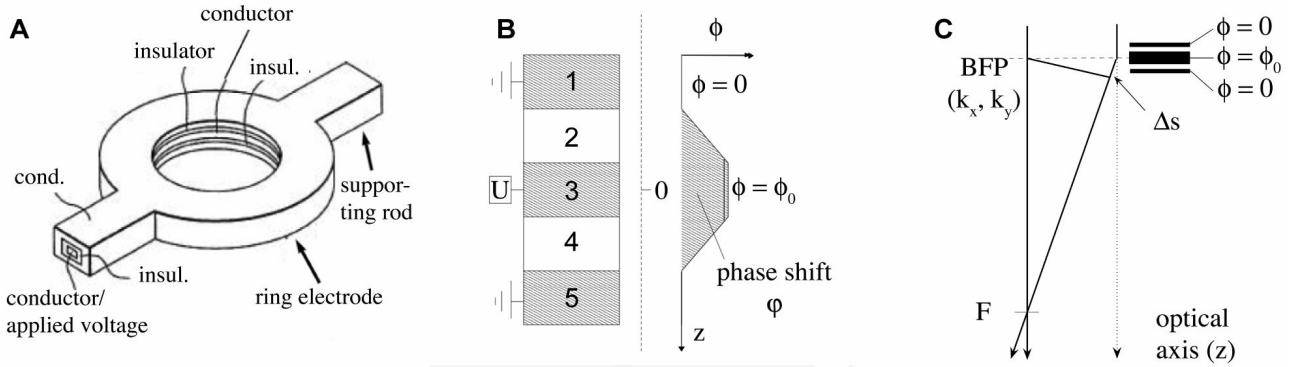


Figure 2.6.: (A) Design of the Boersch phase plate as an electrostatic einzel lens proposed by Matsumoto et al. (B) Modelling the phase shift of the electron wave produced by the field of an electrostatic einzel lens. An electron passing along the optical (z -) axis close to the edge of the phase plate electrode. The axial potential $\phi_0(z)$ can be approximated by homogeneous electrical fields between the conductive layers (grey: conductor, white: insulator). (B) Lens effect of the electrode. Given a finite focal length F , the path difference Δs results in a phase shift depending on the spatial frequency (see text).

2.2.5 Modelling phase shift and lens effect of Boersch's electrostatic phase plate

Boersch's electrostatic phase plate can be regarded as an implementation of the Zernike phase plate. Instead of the scattered wave, the phase of the unscattered electron wave is shifted by means of an electrostatic potential. The technical implementation first described by Matsumoto and Tonomura (1996) as an electrostatic einzel lens is shown in fig. 2.6. The phase shift of an electron wave travelling through the potential ϕ inside the ring electrode is given by

$$\varphi_{PP} = \frac{\pi}{\lambda U_0} \chi(U_0) \int_s ds \phi(s). \quad (2.43)$$

For 200 keV electrons, the relativistic correction factor is $\chi(U_0) \approx 1.16$. If the electron path s is parallel to the optical (z -) axis, it can easily be shown that the integrated potential

$$\Phi_0 = \int \phi(z) dz \quad (2.44)$$

is constant in the (x, y) plane using the Laplace equation (Matsumoto and Tonomura 1996). The only prerequisites are that 1st the potential is laterally restricted to the electrode ring and 2nd that the potential vanishes at infinite distances ($\phi(\pm\infty) = 0$). This is called the negligible-lens approximation, as no deflection of the electrons by the electrode field is assumed.

Using (2.44) and assuming an axial potential $\phi(z)$ of the form depicted in fig. 2.6 B, the phase shift can be calculated for an electron passing through the electrostatic einzel lens at an infinitesimal distance from the ring electrode:

$$\Phi_0 = \phi_0 \left(\frac{t_2}{2} + t_3 + \frac{t_4}{2} \right), \quad (2.45)$$

where t_i denote the layers as depicted in fig. 2.6 A.

The ring electrode will act as an electrostatic einzel lens, and thus the validity of the negligible-lens approximation must be reconsidered. An electron is assumed passing through the electrode at a distance r from the centre. The resulting phase shift $\varphi_{lens}(r)$ can be estimated to a first approximation as

$$\varphi_{lens}(r) = \frac{2\pi r^2}{\lambda F} \quad (2.46)$$

which is derived from the path difference Δs in fig. 2.6 C. F is the focal length of the einzel lens and depends on its geometry as well as on the potential ϕ_0 . If the lens is centred on the optical axis in the BFP and using the relation $r = \lambda f k$, the phase shift as a function of the spatial frequency k becomes

$$\varphi_{lens}(k) = 2\pi \lambda \frac{f^2}{F} k^2. \quad (2.47)$$

As derived here, the phase shift resulting from the einzel lens is proportional to k^2 . Thus it can be subsumed under the defocus term of the conventional wave aberration $W(k) = \pi/2 (C_s \lambda^3 k^4 - 2\lambda Z k^2)$, increasing the apparent defocus Z . This effect was indeed observed during the experiments shown in section 3. It can be understood in a simplified model of image formation: in conventional imaging, the image is formed as an interference of the scattered electron wave with an unscattered, planar reference wave. As a result of the lens effect of the Boersch phase plate, the reference wave is slightly curved, which changes the total wave aberration.

3 Development and Proof-of-Concept of the Boersch Electrostatic Phase Plate

An implementation of a quarter wave plate for the electron microscope, designed as an electrostatic einzel lens, was proposed by Boersch in 1947. The small dimensions of the device have impeded its realisation up to now. This thesis presents the first fabrication and application of a miniaturised electrostatic einzel lens driven as TEM quarter-wave phase plate. The phase modulation is generated by the electrostatic field confined to the inside of a micro-structured ring electrode. This field affects the phase velocity of the unscattered part of the electron wave. By varying its strength, the phase shift of the primary beam can be adjusted to $\lambda/4$, producing strong phase contrast independent of spatial frequency. The phase plate proves to be mechanically stable and does not impair image quality, in particular it does not reduce the high resolution signal. The measured residual lens effect of the einzel lens is minimal. The micro-lens is supported by conducting rods arranged in a threefold rotational symmetry. This particular geometry provides single-sideband signal transfer for spatial frequencies otherwise obstructed by the supporting rods.

3.1 Proof-of-concept

The advantage of the Boersch phase plate is obvious: no further electron scattering is introduced into the beam path, which avoids possible contamination problems and additional inelastic or plural scattering. High-resolution information is not affected and is transferred to the phase contrast image at its full signal strength. Furthermore it is possible to achieve any appropriate phase shift by simply varying the electric potential of the phase plate. Hence, if complex reconstruction of the object is needed (Danev and Nagayama 2001a), both bright-field and phase contrast images can be recorded without the need to insert or retract the phase plate. The design of the Boersch electrostatic phase plate as an electrostatic einzel lens, which could be placed in the BFP and would only affect the unscattered electron beam (fig. 3.1 A), was first proposed by Matsumoto et al. (Matsumoto and Tonomura 1996; Matsumoto et al. 1997). With the recent development of micro- and nano-structuring techniques, it has become possible to fabricate such an electrostatic einzel lens for the first

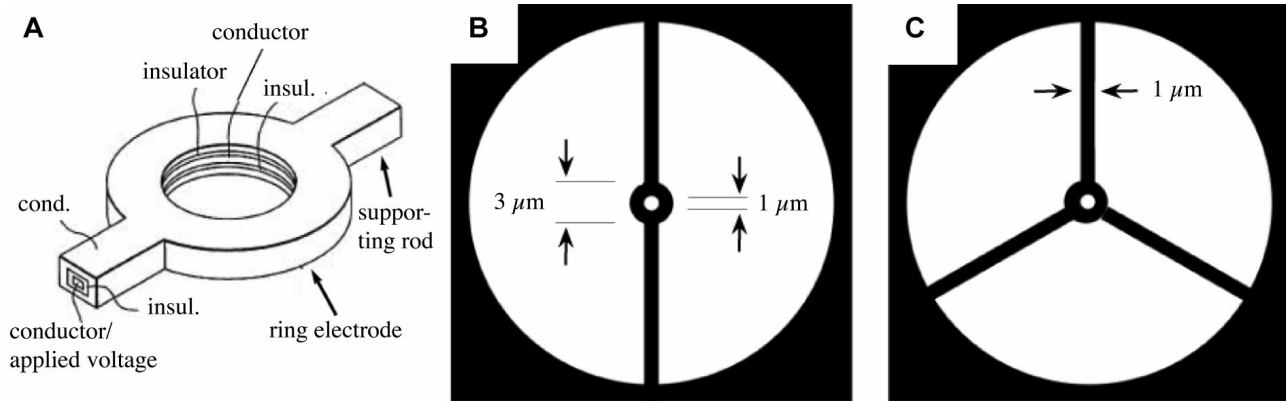


Figure 3.1.: (A) Design of the electrostatic phase plate as proposed by Matsumoto and Tonomura (1996). The central ring electrode consists of five layers of several 10 nm thickness, capturing an electrostatic potential within the ring (cf. fig. 2.6). The phase of the unscattered central beam passing through the hole is shifted, according to the potentials applied to the central electrode layer. The unscattered wave portion passes through outside the ring and remains unaffected. (B, C) Possible geometry of the Boersch phase plate: 2-fold symmetry (B) and 3-fold symmetry (C). Typical dimensions of the phase plate hole, the ring and the supporting rods are indicated in the schematic drawings. The diameter of the aperture is on the order of 100 μm .

time (Schultheiß et al. 2006). Results obtained with this phase plate in the BFP of a Zeiss EFTEM SESAM II Cryo, its effects on the imaging process, and its ability to shift the phase by $\pi/2$ or 90° , are presented in this chapter. The threefold symmetry of the support rods produces single-sideband imaging conditions in the obstructed regions of the BFP, which allows a simple numerical restoration of structure factors affected by the microlens structure.

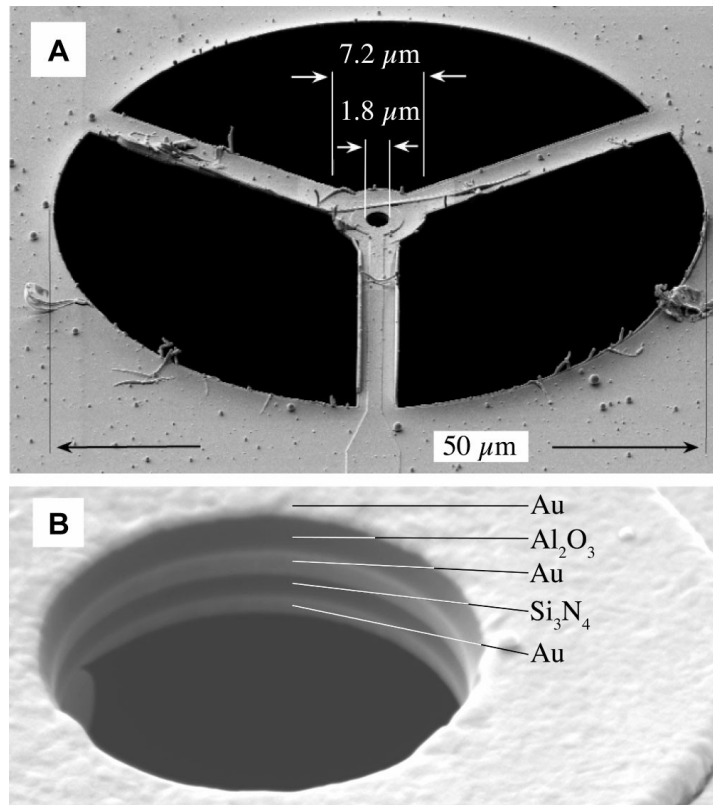
3.1.1 Fabrication of the miniaturised electrostatic einzel lens

The design of the phase plate follows the conventional three-electrode type of an electrostatic einzel lens, with inner dimensions of 1–2 μm . The electrodes form a five layer sandwich structure as proposed by Matsumoto and Tonomura (1996) and were first fabricated as described by Schultheiß et al. (2006). Fig. 3.2 A shows an overall view of the phase plate used in this work. The layered structure of the electrostatic lens is shown in detail in fig. 3.2 B.

Phase plates were structured starting with a commercially available low-stress silicon nitride ($\text{Si}_{3+x}\text{N}_{4-x}$) membrane with a nominal thickness of 100 nm. The membrane is supported by a 200 μm thick silicon frame. The central electrode was defined on the $\text{Si}_{3+x}\text{N}_{4-x}$ membrane by standard electron beam lithography and subsequent electron beam evaporation of gold under high vacuum

conditions. A potential is applied to the electrode via a millimetre-sized contact pad at some distance from the phase plate. The lead from the contact pad to the inner ring electrode is visible as a slightly thickened structure on the vertical supporting rod (fig. 3.2 A). The threefold symmetrical support rods for the electrostatic lens were then patterned into the membrane using the 30 kV Ga⁺ focussed ion beam of a Zeiss EsB1540 SEM/FIB dual-beam instrument. An insulating layer of sapphire (Al_2O_3) was evaporated onto the gold electrode, followed by another gold film to shield the electrostatic field of the central layer. The membrane was rotated during the evaporation process to cover it from all sides. Finally, the central hole was milled into the ring electrode, exposing the central conducting layer as seen in fig. 3.2 B. The measured layer thicknesses (along the beam axis) of the phase plate used in this study are $t_1^{(Au)}=101\text{ nm}$, $t_2^{(Al_2O_3)}=245\text{ nm}$, $t_3^{(Au)}=125\text{ nm}$, $t_4^{(sin)}=144\text{ nm}$ and $t_5^{(Au)}=125\text{ nm}$, resulting in a total thickness of 740 nm. The measurements of these layer thicknesses from the SEM image have an error in the order of $\pm 25\text{ nm}$ due to image pixel size of 4 nm and gradual contrast change between the different layers. The lateral diameter of the surrounding aperture was chosen as $d_a=50\text{ }\mu\text{m}$ and the width of the three supporting rods was 3 μm . The outer diameter of the central ring electrode is $d_o=7.2\text{ }\mu\text{m}$ while the central hole has a diameter of $d_i=1.8\text{ }\mu\text{m}$.

Figure 3.2.: (a) SEM picture of the Borsch phase plate. The diameter of the surrounding aperture is $d_a = 50 \mu\text{m}$, the outer diameter of the ring electrode is $d_o = 7.2 \mu\text{m}$ and the hole diameter $d_i = 1.8 \mu\text{m}$. (b) 5-layer structure of the electrode ring. The total height is 780 nm.



The threefold symmetry of the lens-supporting rods (fig. 3.2 A) was chosen to maximise mechanical stability, while at the same time minimising the loss of information in the image. Theory, simulations, and experimental results of this optimised geometry are discussed in section 3.2. A silicon frame containing two phase plates was fixed onto a 300 μm thick aluminium plate, attached to a piezo-driven micro-manipulator (Kleindiek MM3 Nanomotor) to position it in the BFP of the objective lens (fig. 3.3). The piezo motors allow positioning of the phase plates in lateral (x,y) direction as well as along the electron-optical axis z with an accuracy of better than 10 nm. The central phase plate electrode and the shielding gold layer are contacted separately. While the outer layer is held on anode potential (ground), a variable potential U is applied to the central electrode layer. The electrostatic lens field is shielded by the surrounding gold layer and thereby confined to the inside of the electrode ring, i.e. to the path of the unscattered primary beam.

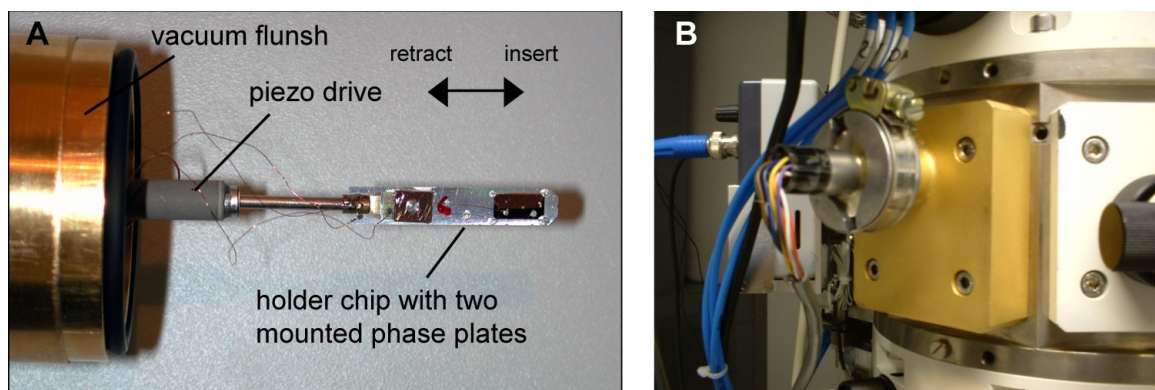


Figure 3.3.: (A) Piezo-driven holder to position the electrostatic phase plate inside the objective of the TEM. The holder arm with two rotational (y,z) and one translational ($x = \text{retract/insert}$) is attached to a vacuum flange containing an electrical feed-through to supply the piezo and phase plate voltages (B). The mechanical precision and stability of the system was better than 10 nm. Two Boersch phase plates can be mounted at the same time. By exchanging the tip, the same system can also be used for positioning of carbon film phase plates.

3.1.2 Experimental verification of the $\pi/2$ phase shift

All experimental tests of the phase plates were performed in a Zeiss EFTEM SESAM II Cryo (focal length $f = 3.0$ mm, spherical aberration coefficient $C_s = 2.2$ mm), equipped with a corrected 90° in-column energy filter and a Schottky field emission gun (FEG). The microscope was operated with an electron energy of 200 keV, the working temperature of the FEG was 1800° K, with an extractor voltage of 4.6 kV. The FWHM of the Gaussian intensity distribution of the focal spot in the BFP was estimated to be ≈ 800 nm.

As a test specimen, amorphous carbon film coated with a thin layer of uranyl acetate was chosen. Images of this object show an equal distribution of all spatial frequencies (white noise). This allows an easy on-line analysis of the electron optical contrast transfer simply by assessing the positions and spacing of the Thon rings. Due to the large portion of coherent high angle scattering by the heavy uranium atoms, image spectra show strong signal at high spatial frequencies up to $1 / 0.4 \text{ nm}^{-1}$. The phase plate was laterally aligned in diffraction mode so that the primary beam was seen to pass through the hole of the central ring electrode. Since the outer aperture and the electrode structure show a clear shadow in the BFP, manual positioning is possible in less than a minute. The optimised vertical position in the BFP is found by focussing edges of the phase plate shadow in diffraction mode. Depending on the mounting of the phase plate chips it was occasionally necessary to

refine the position of the BFP of the objective lens by changing the excitation of the condenser system, in order to increase the distance between BFP and the lower pole piece.

Image series were acquired typically containing 40 images with the phase plate in the BFP at a magnification of 119.800 x on a 1024x1024 pixel GATAN slow-scan CCD camera (Gatan Inc., Pleasanton, USA). The images were zero-loss energy filtered to enhance the SNR. The voltage applied to the central electrode was increased stepwise up to $U \approx 1 \text{ V}$, with a reproducibility and accuracy of the voltage generator of 10 mV. Power spectra (fig. 3.4 A) of the images were obtained by calculating the numerical Fourier transform using MatLab (The Math-Works, USA), which was also used for further data processing (see appendix D). To minimise effects of instabilities of the objective lens or the voltage applied to the phase plate, the spectra of three subsequent images, taken at the same EM settings, were averaged. As an example the power spectra of images recorded at phase plate potentials of 0 V or 0.31 V are shown in fig. 3.4 A. Note the change in position of the Thon rings, which is also seen in the averaged radial intensity profile of the power spectra in fig. 3.4 B. This experiment proves directly the change in contrast transfer of the electron optical lens system, which now includes the electrostatic phase plate, when a potential is applied to the central einzel lens electrode.

To quantify the change of contrast transfer in the recorded images, and thus the relative phase shift between scattered and unscattered electron beam, squared model CTFs of the form

$$|CTF(k)|^2 = |2 \sin W(k) - 2a \cos W(k)|^2 \quad (3.1)$$

were fitted to the data after background subtraction using a least squares algorithm. Appropriate envelope functions for spatial and temporal incoherence and specimen related signal decay were included (see section 2.1.7). The ratio of object amplitude and phase potential was determined to be $a = 29\%$ from images with no phase plate inserted. A potential-dependent defocus value $Z(U)$ and an additional constant phase $\varphi_{pp}(U)$ were used as independent fitting parameters in the wave aberration:

$$W(U, k) = \frac{\pi}{2} (C_s \lambda^3 k^4 - 2 \lambda Z(U) k^2) - \varphi_{pp}(U) \quad (3.2)$$

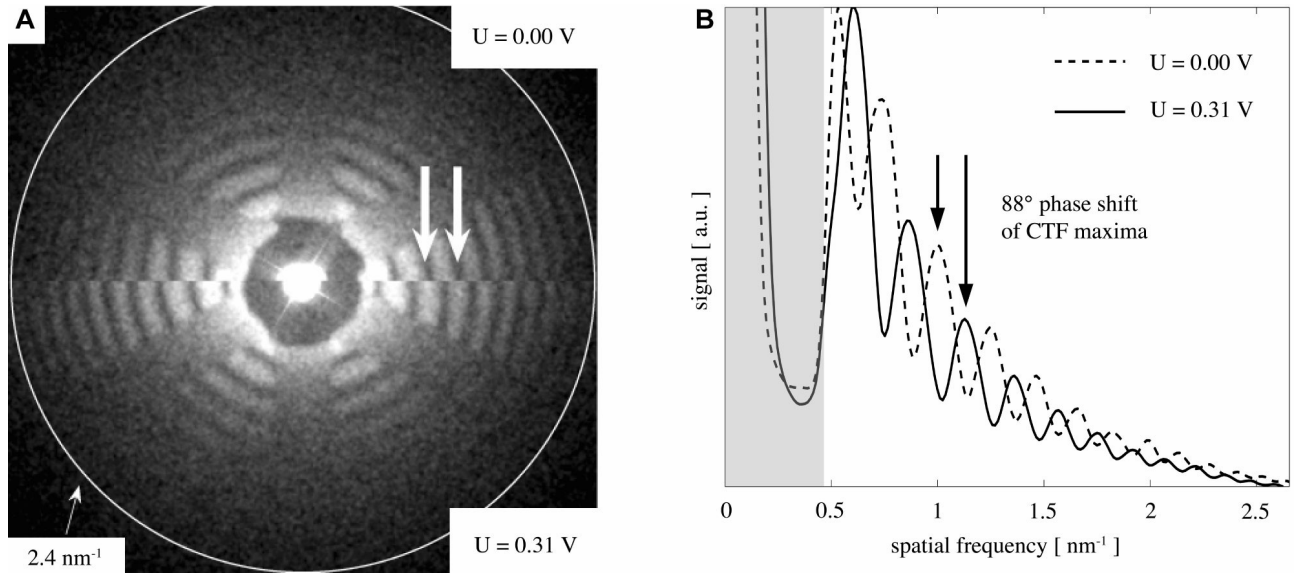


Figure 3.4.: Conversion of a bright-field sine CTF into a phase contrast cosine CTF. (A) Power spectra of images of uranyl acetate on carbon film. The two half images show power spectra at a constant underfocus of $Z = 690$ nm with the Boersch phase plate in the BFP of the objective lens at an applied potential of 0 and 0.31 V, respectively. The Thon rings corresponding to the maxima of the CTF are uniformly shifted, indicating a constant phase shift of the primary electron beam. (B) Radial intensities of the power spectra from A. The constant shift of the maxima indicates a phase shift of the CTF by 88° (for details on the numerical fitting procedure see text). Signal transfer for spatial frequencies lower than $1/2.4$ nm $^{-1}$ is blocked due to obstruction by the ring electrode. Data are averaged azimuthally over 5° and further smoothed by applying a box convolution.

The resulting fit for the phase shift $\varphi_{pp}(U)$ and defocus $Z(U) = Z + Z_{pp}(U)$ for a typical image series are shown in fig. 3.5. The CTFs clearly reveal a shift which is independent of the spatial frequency k and proportional to the applied electrode voltage (fig. 3.5 A), as predicted from theory (eq 2.44). The phase could be shifted by up to 207° at $U = 1.0$ V. This is more than twice the amount of uniform phase shift required to obtain a cosine-shaped phase plate-mediated CTF. A phase shift of $\pi/2$, or 90° , was reached at a potential of ≈ 0.4 V. A linear fit to the data points (assuming 0° constant phase shift at $U = 0$ V) yields a relative phase shift of about $200^\circ/\text{V}$.

Following the theoretical considerations in section 2.2.5, the calculations for the applied layer thickness composition (cf. fig. 3.2) yield a phase shift of $133^\circ/\text{V}$ for 200 keV electrons. Assuming this value, an electrode potential of $\phi_0 = 0.68$ V would be sufficient for obtaining a 90° phase shift of the primary beam. The experimental results indicate that a smaller potential is sufficient. Possible reasons are 1st - a difference in material and “effective electric” layer thicknesses and 2nd - edge ef-

fects due to the small dimensions of the device.

3.1.3 *Assessing the lens effect of the ring electrode*

In the negligible-lens approximation described in section 2.2.5, the electrostatic einzel lens should act as a device which only affects the phase of the unscattered electron wave. In this case, deflection caused by the electrostatic field can be neglected. Numerical simulations (Matsumoto and Tonomura 1996) yield deflection angles in the range of some 10^{-6} mrad for an electrode potential $< 1V$, which are negligible compared to the mean scattering angle of ≈ 10 mrad. In this case, all electrons in the central beam are phase shifted uniformly, resulting in a constant phase shift of the CTF.

However, the CTF phase shifts obtained from the experiments revealed a k^2 -dependent contribution. This can be expressed in terms of a change in defocus, and its voltage dependence is shown in fig. 3.5 B. Fits of various data sets resulted in a mean defocus change of $Z_{pp}(U)/U = 29 \pm 10 \text{ nm/V}$, corresponding to a focal length of the einzel lens of $F = (1200 \pm 600) \text{ m}$ at an applied potential of $U = 0.5 \text{ V}$. This is still within the negligible-lens approximation, indicating that this approximation indeed applies to the phase plate design applied for this work. Apparently, the thickness and composition of the layered structure does not have a large effect on the electron path deflection.

Although electrodes with very different ratios $t_2^{(Al_2O_3)} / t_3^{(Au)}$ of 1.5 or 6.0 were tested, the observed defocus changes were very similar. Although the deflection of the unscattered electrons - the lens effect of the phase plate - is small, the additional frequency-dependent phase shift has to be considered for high-resolution imaging. For an applied voltage $U = 0.4 \text{ V}$, giving a phase shift $W(k)$ of 90° at $k = 0$, the value would change to 112° at $k = 1/(0.5 \text{ nm})$. This problem is simply solved by imaging at a defocus of $Z = -Z_{pp}(U)$ instead of Gaussian focus, to obtain optimal phase contrast. A wave aberration introduced by the phase plate of the order of k^2 can always be compensated by an additional objective lens defocus. Consequently, the observed electron deflection by the ring electrode does not impede the use of the Boersch phase plate in TEM imaging.

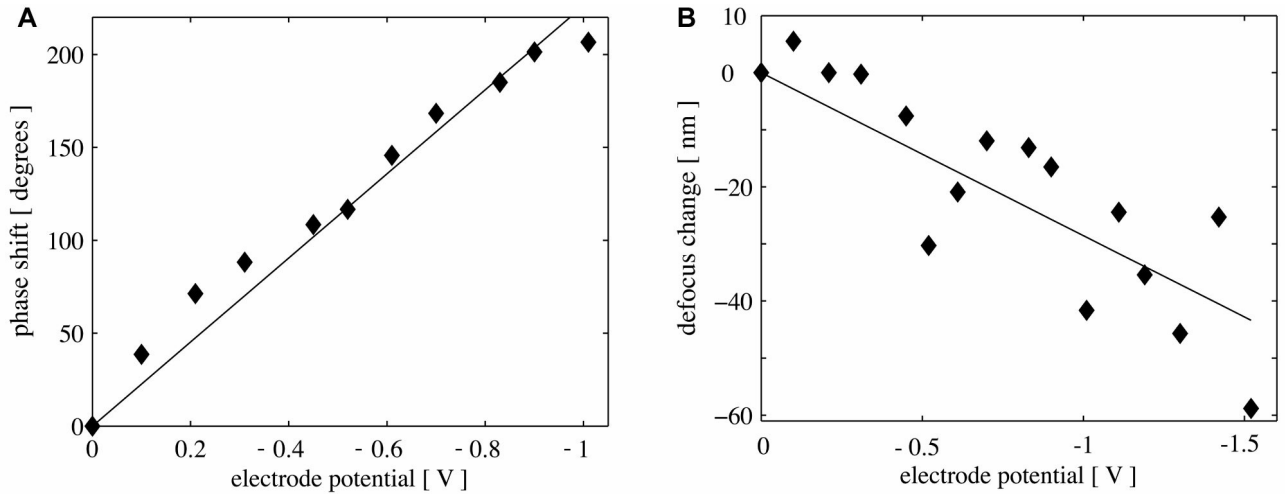


Figure 3.5.: Phase shifts and lens effect of the phase plate as observed in images of uranyl acetate on carbon film recorded at different phase plate potentials. Data points represent the constant phase shift $\varphi_{PP}(U)$ and the defocus $Z_{PP}(U)$ depending on the potential U as derived by numerical fit of expression (3.1) and (3.2) to the experimental CTF data. (A) Constant phase shift $\varphi_{PP}(U)$ of the image CTFs. The interpolation shows a linear dependence on the voltage U applied to the phase plate. (B) The einzel lens causes a small defocus change of ca. 30 nm/V, i.e. a spatial frequency-dependent phase shift proportional to k^2 .

3.2 The signal transfer properties of possible Boersch phase plate geometries

3.2.1 Phase contrast simulations as guide for phase plate design

Section 3.1.2 presents and discusses the experimental evidence that an electrostatic einzel lens can indeed be used as quarter-wave phase plate for TEM. What has not been considered so far are the inevitable but undesirable side effects on the image introduced by the finite size of the lens and its supporting structure. To assess the extent of obstruction and the resulting limitations of possible designs, the effects of a number of different sizes and geometries were simulated.

The simulations were performed with the image processing program SPIDER (Frank et al., 1996) and the image simulation package YaMS (Dinges et al., 1995; Müller et al., 1998), both modified by the addition of own tools specific to phase plate simulation. In the simulations shown here a Siemens star (cf. fig. 3.6) is converted into a weak phase object $P(x, y)$ by transforming a real object density distribution $a(x, y)$ into the real and imaginary part of a complex image, $P(x, y) = \exp\{i a(x, y)\}$. The maximum phase shift is assumed to be 10° (dark areas of Siemens

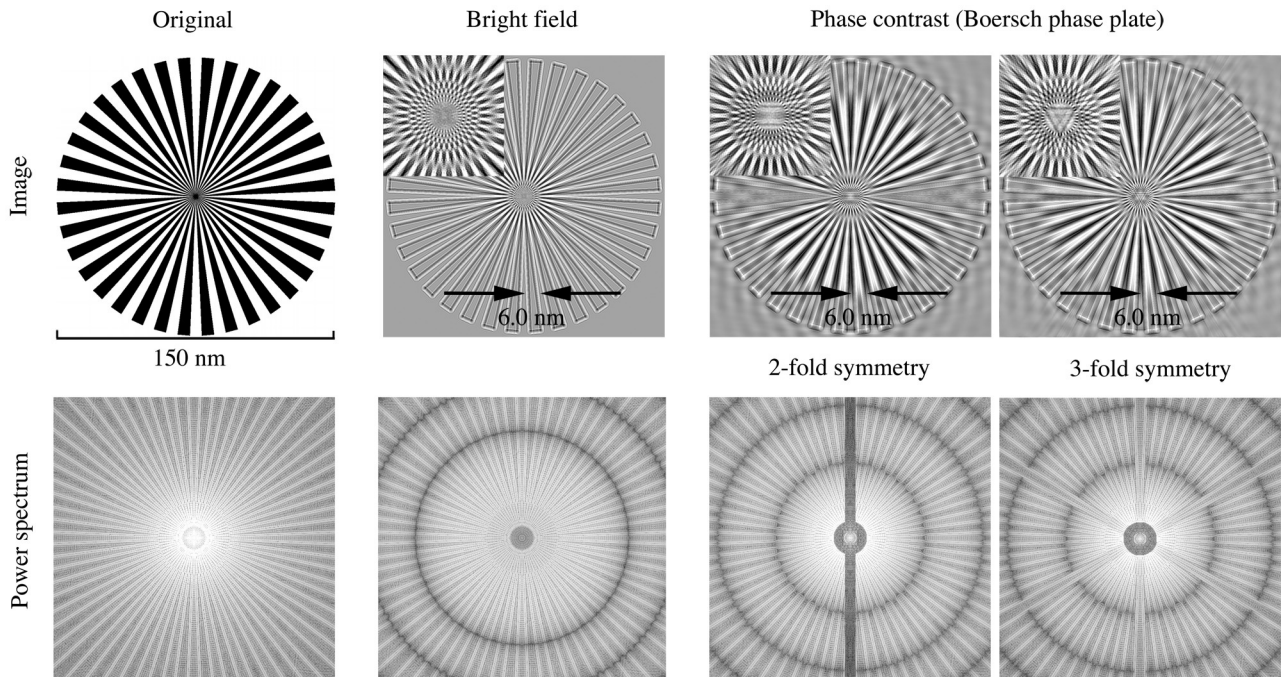


Figure 3.6.: Effect of twofold or threefold symmetrical support rods on signal transfer (electron energy 120 keV, focal length 2.7 mm, diameter of ring electrode 3 μm). Shown are an original object (Siemens star, dark area represent weak phase object of 10° phase shift at molecular dimensions, scale bar = 150 nm) and the inner part of its logarithmic power spectrum. Images (top row) and power spectra (bottom row) are simulated for typical bright-field contrast without phase plate and for phase contrast with a phase plate of twofold or threefold support symmetry at a phase shift of $\pi/2$ (positive phase contrast). The insets show the enlarged centre of the simulated image. The simulations show the partial loss of information in the obstructed part of the BFP: While conventional bright-field conditions result in isotropic information loss and contrast reversal, the phase contrast images show an additional shadowing by the ring-shaped lens and its twofold and threefold supporting rods. In case of threefold symmetry, the original object information can be retrieved, as discussed in the text. Note the contrast reversal and position of isotropic information loss in bright-field and phase contrast images (dark rings in power spectra), reflecting the $\pi/2$ phase shift and corresponding $\sin \rightarrow \cos$ transformation of the CTF. The pair of arrows points to an object detail of 6.0 nm size, which corresponds to the cut-on frequency of the phase plate electrode.

star in fig. 3.6, $a(x, y) \leq \pi/18$), which seems to be a realistic value for weak phase objects in biology (Simon et al. 2003). The Siemens star was chosen as a test object, since its visual appearance depends strongly on the correct interference of the initial structure factors. Therefore, it gives an immediate visual feedback on the effects of contrast transfer resulting from different phase plate designs.

As listed in table 1, different parameters for the simulations can be used. Desirable conditions for macromolecular imaging at realistic dimensions of the Boersch phase plate are assumed. The im-

ages shown in fig. 3.6 are simulated for a 120 keV TEM (electron wavelength $\lambda = 3.34$ nm) with a spherical aberration coefficient $C_s = 2.7$ mm and focal length $f = 2.7$ mm. The phase plate aperture diameter is 100 μm while the diameter of the central lens opening is 0.97 μm . An image size of 4096 x 4096 pixels with a pixel size ≈ 0.05 nm was chosen. In Fourier space this corresponds to a sampling of 0.00488 nm $^{-1}$ and a pixel size of 44 nm if expressed in real distances in the BFP, as calculated from $r = \lambda f k$ (r : distance from the optical axis in the BFP). The supporting rods were assumed to be 0.97 μm wide. The underfocus was chosen at 300 nm.

TEM	$d_o / \mu\text{m}$	cut-on / nm
E = 120 keV	7.2	2.5
f = 2.7 mm	3.0	6.0
E = 200 keV	7.2	2.1
f = 3.0 mm	3.0	5.0
E = 300 keV	7.2	1.5
f = 2.7 mm	3.0	3.5

Table 1. Low spatial frequency cut-on resulting from the Boersch electrode with outer diameters (tested prototype, proposed smallest diameter of electrode) for different electron energies E and focal lengths of the objective lens f , corresponding to three different commercially available TEMs.

3.2.2 Obstruction of structure factors by the ring electrode and twofold vs. threefold lens-supporting rods

The ring electrode of the electrostatic lens and its supporting rods lead to a complete loss of those structure factors blocked in the BFP. The obstruction of the ring electrode cannot be avoided and blocks a band of low spatial frequencies. The cut-on frequency

$$k_{\text{cut-on}} = \frac{d_o/2}{\lambda f} \quad (3.3)$$

depends on the outer diameter d_o of the ring electrode. Table 1 gives some typical values for this cut-on parameter, in particular a cut-on frequency of $1 / 6.0$ nm $^{-1}$ for the simulated phase contrast at 120 keV electron energy and an outer ring electrode diameter of 3 μm . It is interesting to see the effect of this cut-on in the actual images as illustrated in fig. 3.6. Note that for this comparison the bright-field image was simulated without an obstructing phase plate in the BFP. In case of the phase contrast images the expected blocking of structure factors at low spatial frequencies is obvious (cf.

fig. 3.6, bright-field and phase contrast images). The simulation illustrates that for typical macromolecular imaging conditions (cf. scale bar 150 nm) a low-frequency cut-on of $1 / 6.0 \text{ nm}^{-1}$ is tolerable. An object of a size a few times larger than the corresponding cut-on frequency is imaged with negligible effect of the obstructing ring electrode, the corresponding area of the star is imaged reasonably well (cf. arrows in bright-field and phase contrast images at an object size - thickness of Siemens star arm - of 6.0 nm). The loss of a low spatial frequency band is observed in the power spectra of the phase contrast images as a dark central ring.

A very different situation applies to the supporting rods of the ring electrode. fig. 3.1 A and B show the centro-symmetrical twofold support symmetry as proposed by Matsumoto and Tonomura alongside a non-centro-symmetrical threefold symmetry (fig. 3.1 C). Simulated images for these two support symmetries (fig. 3.6, phase contrast images) show strong image aberrations at all spatial frequencies, most obviously for high spatial frequencies (centre of the Siemens star). The reason for these aberrations is easily explained by the obstruction of structure factors in the BFP (fig. 3.6, phase contrast power spectra). Power spectra are calculated from the simulated image intensities, thus Friedel symmetry of structure factors is imposed, which results in centro-symmetrical power spectra. In case of twofold support symmetry the complete loss of information in the BFP is apparent. Along the direction of the supporting rods no image information is available. By contrast, for the threefold support symmetry a six-fold shadow pattern is visible, however, structure factors are not blocked completely but modified in the following way: the observation of a non-blocked signal transfer reflects the single-sideband imaging conditions for a non-centro-symmetrical support geometry of the ring electrode.

The form of the phase and amplitude of the Boersch aperture function (see section 2.1.2) is illustrated in fig. 3.7. The supporting rods block electrons only on one side ($+k_x$) of the diffraction pattern in the BFP, while electrons scattered in the Friedel position ($-k_x$) are not obstructed. This results in single-sideband imaging conditions (see fig. 3.8). However, the obstructed signal can be fully restored, although the SNR is reduced in the affected region.

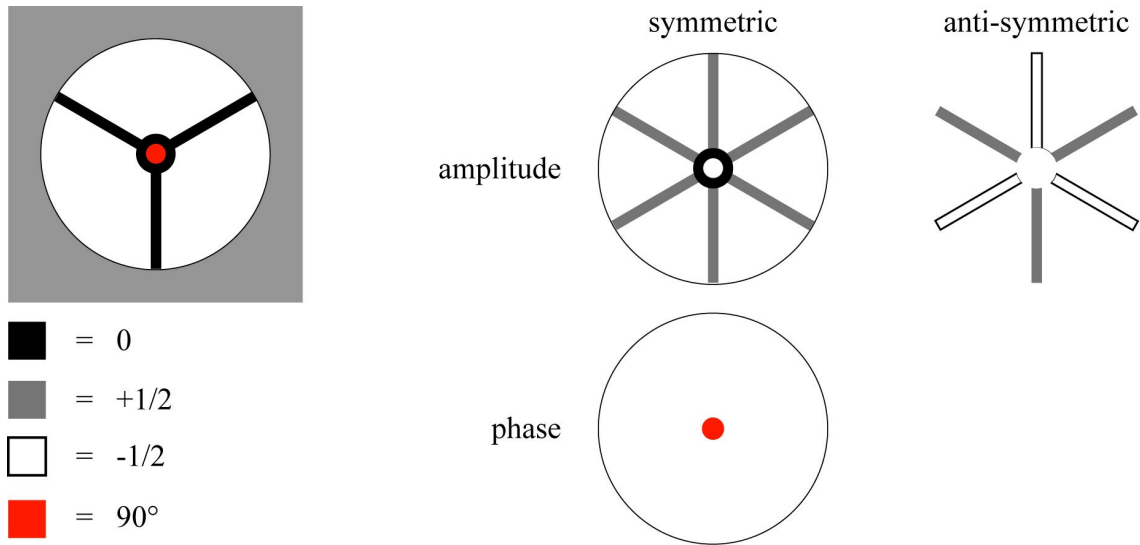


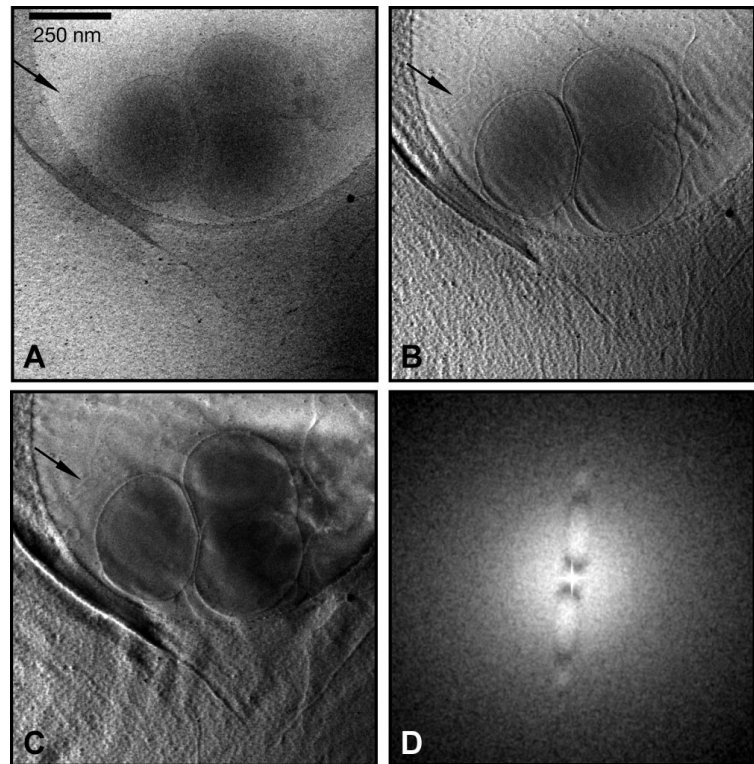
Figure 3.7.: Symmetric and anti-symmetric components of amplitude and phase of the Boersch aperture function (see section 2.1.3). The threefold arrangement of the support rods avoids the total loss of the corresponding spatial frequencies, as the signal is transferred via single-sideband contrast (see text).

As derived in section 2.2.4, the single-sideband phase contrast transfer function is given by

$$pCTF_{SSB}(\mathbf{k}) = -\frac{1}{2} i \text{sign}(k_x) \exp\{-i \text{sign}(k_x) W(k)\}. \quad (3.4)$$

This means that amplitude and phase of the pCTF in the Fourier space “obstructed” by the support rods is anti-symmetrically modulated by $-i \text{sign}(k_x)$ and $-i \text{sign}(k_x) W(k)$, respectively. Its squared modulus is $|pCTF_{SSB}(\mathbf{k})|^2 = 1/4$, reflected in the lack of CTF zeroes along the six-fold shadow pattern in the power spectrum of the simulated phase contrast image in fig. 3.6. The data can thus be corrected for the CTF by applying the inverse functions, $\sin^{-1} W(k)$, to structure factors in between rods and $-2i \text{sign}(k_x) \exp\{i \text{sign}(k_x) W(k)\}$ to the partially obstructed structure factors.

Figure 3.8.: Effect of single-sideband (SSB) contrast on an image of a typical cryo specimen (thylakoid membrane vesicles from plant chloroplasts in vitrified ice, ice thickness approx. 400 nm, 20 kx prim. mag.). (A) Nearly all of the object structure factors are transferred via phase contrast, as the object is essentially invisible in focus ($|CTF| \approx \sin 0$). (B, C) The contrast is enhanced if one half of the BFP is covered (SSB contrast, $|CTF| \approx \frac{1}{2} = \text{const.}$). The appearance of the image is comparable to that of a Hilbert phase plate image, but the SNR is attenuated by a factor of $\frac{1}{2}$. (D) Power spectrum of amorphous carbon film imaged under SSB conditions with high defocus. Apart from a narrow stripe of spatial frequencies transferred with the bright-field sine CTF, the partially obstructed part of the spectrum shows non-oscillating SSB contrast.



In contrast to the centro-symmetrical geometry, where the entire information blocked by the rods is lost, the threefold support geometry does not cause any substantial loss of information. It is also obvious from (3.4) that the maximal transmitted SNR is reduced by a factor of two in the affected regions with respect to the non-obstructed CTF (cf. fig. 3.9). This may result in a lower structural resolution in the corresponding image directions. However, for high spatial frequencies the spectral area shadowed by the rods is relatively small (see fig. 3.6), as its ratio to the overall area is approximately $6W(\pi\lambda f k)^{-1}$, where W is the rod width. Therefore this effective loss of signal is less critical for high-resolution imaging. On the other hand, for low spatial frequencies the signal amplitude should be sufficiently high to allow data correction and object reconstruction.

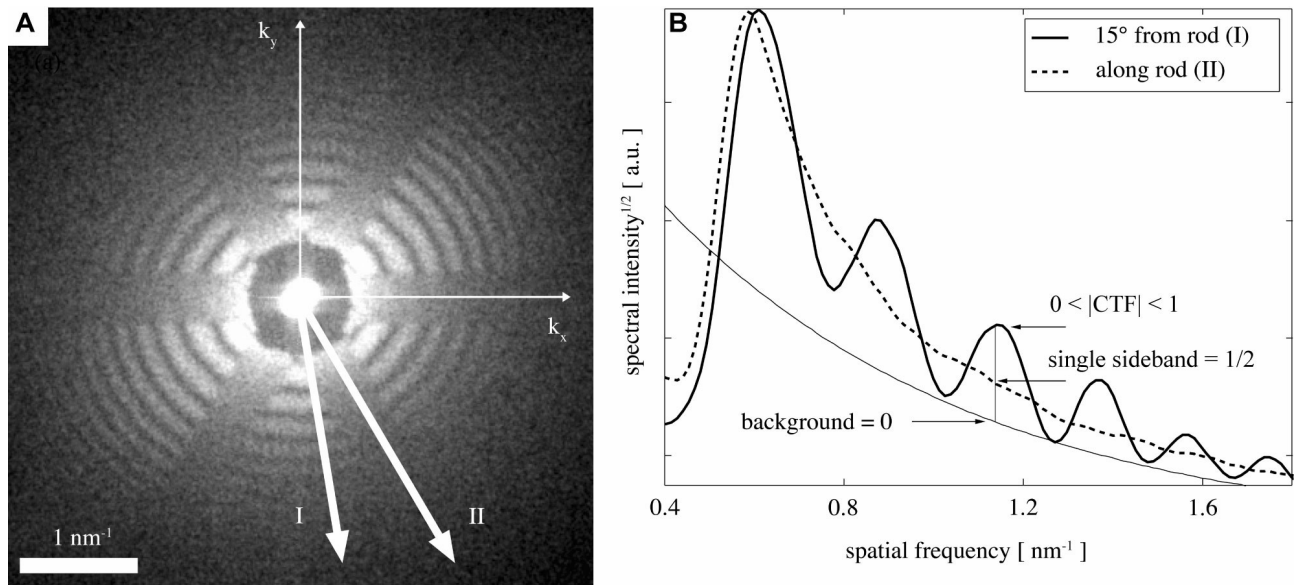


Figure 3.9.: Single-sideband contrast transfer for a threefold phase plate support. (A) Logarithmic power spectrum of an image of amorphous carbon film with a thin layer of uranyl acetate. A Boersch phase plate with threefold support geometry (cf. fig. 3.1 C and 3.2 A) was positioned in the BFP. It is apparent that the signal under the supporting rods is not zero unlike the signal under the central ring electrode. The two arrows indicate the directions of unaffected spatial frequencies (I) and frequencies affected by a supporting rod (II). (B) Square root of radial intensities of the power spectrum along directions I and II in A. The dashed curve shows the non-oscillating single-sideband contrast transfer for spatial frequencies affected by a support rod. Data are averaged azimuthally over 5° and smoothed by applying a box convolution.

3.2.3 Experimental verification of single-sideband contrast transfer for threefold phase plate support geometry

To avoid loss of image information, a non-centro-symmetrical design for the support of the Boersch phase plate was chosen (figs. 3.1 C and 3.2 A). Single-sideband signal transfer was tested by the experimental procedure described in section 3.1.2. Since images of amorphous carbon film contain structure factors at all spatial frequencies in first order at similar strength, the amplitude of all structure factors can be assumed to be ≈ 1 . Thus, the power spectra represent to a good approximation the squared amplitude of the CTF. The logarithmic power spectrum (fig. 3.9 A) shows clearly that the signal transfer for spatial frequencies obstructed by the rods is not zero, as is the case for the central electrode ring. The square root of spectral intensities plotted in fig. 3.9 B shows that for frequencies transferred under the single-sideband condition there are no gaps in the transmitted signal. The dashed curve, which is averaged over a small band along the shadowed region of the spectrum, shows no modulation, in contrast to the non-sideband transferred signal (solid curve). As expected,

the amplitude of the constant single-sideband transfer ($|pCTF(\mathbf{k})| = 1/2$) is almost exactly half the maximum value detected for the non-sideband transferred signal ($|pCTF(k)| = |\sin W(k)|$) adjacent to the rod. This means that for the chosen geometry there is non-zero single-sideband signal transfer, which has no gaps and can be computationally corrected as described in section 3.2.2.

3.3 Evolution of the Boersch phase plate architecture

The experiments clearly show that with the chosen phase plate design, signal transfer is not impaired at high resolution. In particular, there is no interaction of electrons with matter as in the case of a Zernike-type phase plate made of carbon film. It was also shown that the threefold geometry of the supporting rods allows for almost complete information retrieval, i.e. there are no serious obstructing effects of the lens support. Therefore, the electrostatic quarter-wave Boersch phase plate seems to be ideal for high-resolution, high-contrast TEM of biological objects.

It is interesting to note that in contrast to experiments with phase plates consisting of other materials (e.g. carbon film) the data recorded with the phase plate do not show deteriorated data quality. High resolution is not affected at all, the phase plate simply represents an objective aperture (Barton 2005). In the experiments with clean phase plates, i.e. phase plates without any initial contamination from the fabrication process, did not develop obvious contamination and subsequent charging effects. It can be assumed that besides the effect of good vacuum conditions (oil-free cryo conditions) this is also the result of the conducting gold layer covering the phase plate. Most probably the phase plate is also heated by the electron beam during operation. This is also indicated by the observed lateral drift of the phase plate for varying intensity of the electron beam. In future it may thus be necessary to control temperature and to detect and correct misalignment of the phase plate automatically.

Simulations and experiment show that the finite size of the electrostatic einzel lens impedes the transfer of structure factors at low spatial frequencies, which are blocked by the ring electrode. The cut-on of contrast transfer for resolutions below 6.0 nm for the specified simulation conditions (120 kV, $C_s = 2.7$ mm, $f = 2.7$ mm) seems acceptable for imaging of small biological complexes, but will impair phase contrast imaging of larger biological macromolecules and complexes. This effect becomes more severe with increasing electron energy, as the scattering angles become smaller. It is therefore crucial to minimise the overall dimensions of the ring electrode, in particular its outer diameter (cf. fig. 3.2).

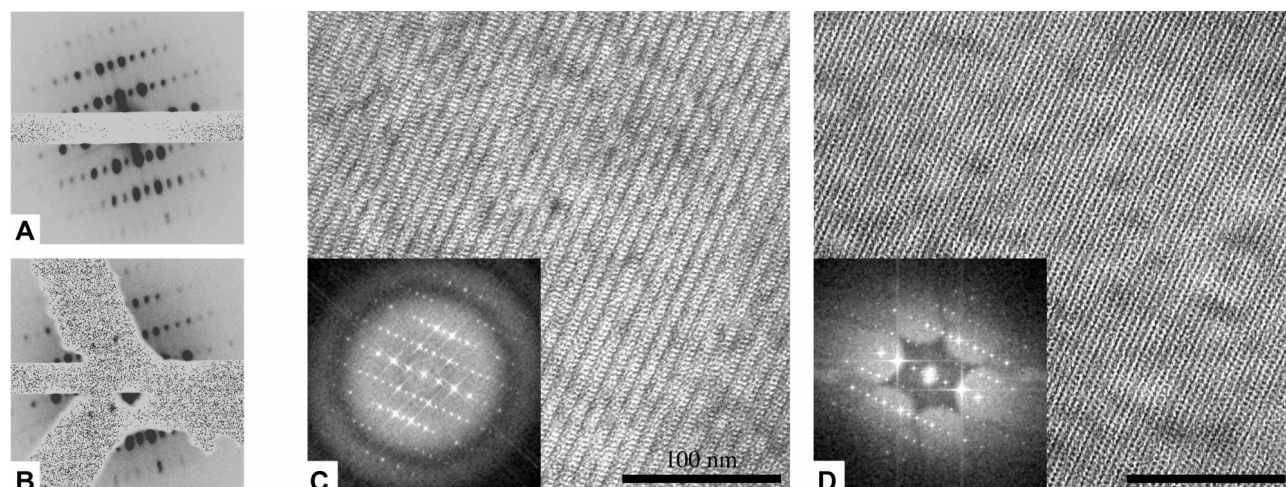


Figure 3.10.: Electron diffraction and imaging with Boersch phase plate in diffraction plane. As sample, negatively stained protein crystals were used (thin 3D micro-crystals of bovine liver catalase, cubic unit cell of 6.9 nm 17.3 nm). (A, B) Electron diffraction patterns without (A) and with (B) phase plate in the diffraction plane (data recorded on a Gatan slow scan CCD). Note that in both cases the central beam is blocked by a beam stop (straight bar). (C, D) Images of catalase crystals without (C) and with (D) phase plate in the diffraction plane. The insets show the power spectra of the images. The contrast of image D is dominated by single-sideband imaging. Only a few Bragg spot Friedel pairs are not obstructed by the phase plate support rods and contribute to the image as phase contrast. Also note the different appearance of the crystal periodicity, which results from the partial blocking of the lowest order Bragg reflections by the innermost parts of the ring electrode. For these experiments a phase plate with modified structure (cf. fig. 3.11) was used. Images were recorded on a ssCCD, the prim. magnification was 65 kx.

For the phase plates and the EM used in the first experiments, with $d_o = 7.2 \mu\text{m}$, $E = 200 \text{ keV}$, and $f = 3.0 \text{ mm}$, all image resolutions lower than $1 / 2.1 \text{ nm}^{-1}$ were lost, as can be seen in Figs. 3.4 and 3.9. While for certain high-resolution imaging applications such as in materials science this may be tolerated, phase plates with an outer ring diameter of around $3 \mu\text{m}$ with a cut-on at $1 / 5 \text{ nm}^{-1}$ need to be designed for biological single particle analysis. Even though imaging conditions would still not be optimal, at least smaller biological molecules and complexes can then be imaged with maximum Boersch phase contrast.

Fig. 3.10 shows images acquired with a modified phase plate geometry at a reduced electron energy of $E = 100 \text{ kV}$. From both electron diffraction and imaging it is obvious that not only the inner ring electrodes, but also the supporting rods need to be minimised. With the present geometries, the imaging with the in principle available true phase contrast does not improve object visibility any further. As is shown in fig. 3.10 D, the apparent image contrast is dominated by the single-sideband

imaging, i.e., almost all diffraction spots are in regions affected by the diffraction rods. The resulting object visibility is comparable to that of the typical mixed amplitude-phase contrast of a negatively stained and defocused bright-field image (fig. 3.10 C). To obtain the full advantage of the Boersch phase plate and to show its improved imaging properties directly, it will be necessary to further minimise the size of its obstructing structure relative to the size of the diffraction pattern of the object.

New generations of Boersch phase plates are manufactured with significantly reduced electrode and rod dimensions (fig. 3.11). One limiting dimension will certainly be the inner opening of the lens, i.e. the corresponding electron beam diameter of the focussed unscattered beam. If the electrode ring and the inner opening become smaller, it becomes more demanding to align the phase plate to the electron beam. This is another argument for automatization of the alignment procedure using also a fully software-controlled stage for the phase plate (see appendix C).

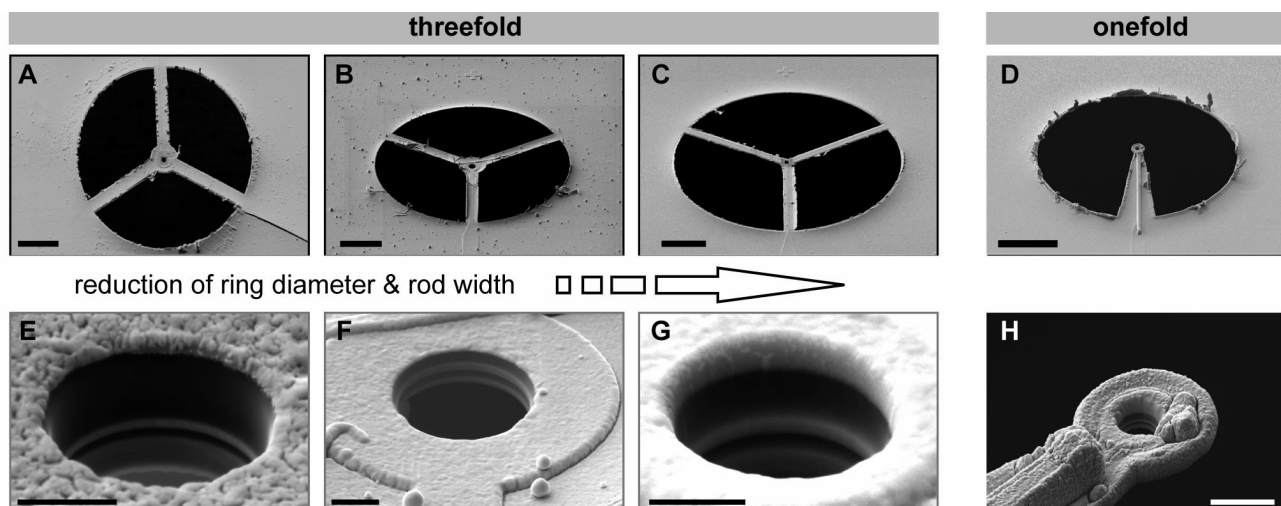


Figure 3.11.: Evolution of geometries of the Boersch electrostatic phase plate towards smaller support and electrode dimensions. (A, E) Inner electrode diameter $d_i=1.6 \mu\text{m}$, outer diameter $d_a=7.1 \mu\text{m}$, support rod width $d_s=3.2 \mu\text{m}$. (B, F) $d_i=1.8 \mu\text{m}$, $d_a=7.2 \mu\text{m}$, $d_s=3.1 \mu\text{m}$. (C, G) $d_i=0.9 \mu\text{m}$, $d_a=2.3 \mu\text{m}$, $d_s=2.3 \mu\text{m}$. (D, H) Design with a single support rod (onefold symmetry). $d_i=1.1 \mu\text{m}$, $d_a=3.7 \mu\text{m}$, $d_s=2.3 \mu\text{m}$ (inside) / $10.7 \mu\text{m}$ (outside). Scale bars: $5 \mu\text{m}$ (top row) and $0.5 \mu\text{m}$ (bottom row).

3.4 Conclusion

Almost 60 years after Boersch proposed an electrostatic quarter-wave phase plate, it has now become possible to produce the required sub-micrometer-sized layered structure of an electrostatic

einzel lens and to use it as a phase plate. The described experiments prove that the unscattered electron beam is uniformly phase shifted by the electrostatic potential of the lens electrode positioned in the centre of the BFP, as proposed by Matsumoto et al. An additional relative phase shift between scattered and unscattered electron wave can be adjusted, and thus, for the appropriate phase shift of $\pi/2$, a conversion of the sine PCTF into a cosine function is achieved. In a C_s corrected TEM with vanishing wave aberration ($W(k) \rightarrow 0$), phase objects can thus be imaged perfectly with a quarter-wave phase plate. At optimal defocus, the phase contrast CTF can be adjusted to its ideal situation, independent of k :

$$pCTF_{\pi/2}(k) = \cos W(k) = 1 . \quad (3.5)$$

This means perfect contrast transfer of weak phase objects up to the information limit in aberration-free images. The first steps for the construction of such an instrument are described in chapter 4.

The use of a non-centro-symmetrical geometry of the einzel lens support allows for single-sideband signal transfer of object information that is potentially obstructed by the supporting rods. Apart from an attenuation of the signal transfer envelope by a factor of $1/2$. This information can be restored by straight-forward image processing. Except for the inevitable loss of signal at low spatial frequencies due to the finite width of the ring electrode, no other information is thus lost irretrievably with the described phase plate design. The expected lens effect, manifested in the deflection of the unscattered electrons, is small within the relevant resolution range and can be compensated by defocusing. The multilayered electrode structure proved to be stable under long-term electron irradiation. The experimental results presented here confirm the theoretical and numerical predictions and show that Boersch phase contrast TEM is possible.

4 Boersch Phase Plate Imaging Enhanced: the PACEM

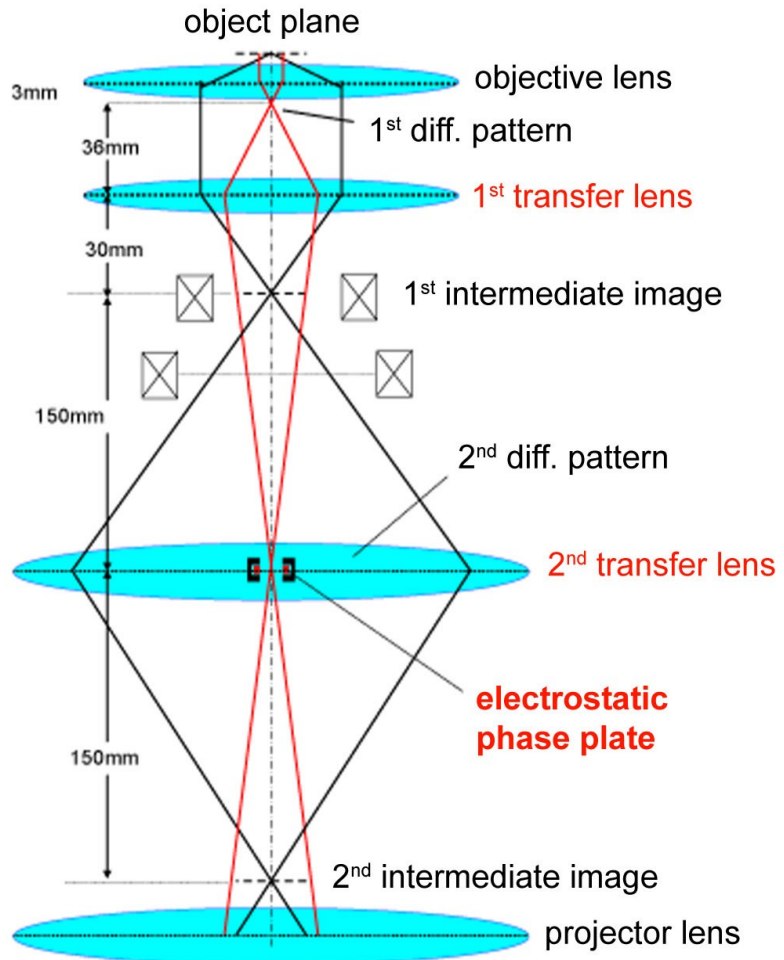
In chapter 3, the first proof-of-principle for Boersch's electrostatic phase plate is shown. It consists of a micrometer-sized einzel lens held in the center of the BFP by threefold support rods. The electrostatic phase plate avoids the attenuation of high-resolution signal, as it occurs in thin-film phase plates. A remaining problem of the design is the obstruction of low spatial frequency signal by the ring electrode and the three support rods. In this chapter, a modified optics of a TEM is described, which reduces the low resolution loss dramatically by increasing the focal length of the objective. The optics generates a magnified diffraction pattern where the phase plate can be placed. An undesirable increase of the spherical aberration, which is connected with an increase of the focal length, can be compensated by incorporation of a double-hexapole C_s corrector. Image simulations show that with the novel PACEM (phase contrast aberration corrected electron microscope), nearly optimal in-focus phase contrast imaging of biological macromolecules is possible.

4.1 Finding an optical solution for the Boersch obstruction problem

Although the design for the Boersch electrostatic phase plate has undergone several miniaturisation steps (cf. fig. 3.11) there will be certain lower limit for the dimensions of the einzel lens electrode and the necessary support rods. If the device is to be applied in structural biology, the retrieval of low object frequencies in the order of a few 10 nanometers is essential, e.g. to map systems of cellular membranes. Thus, the need of an electron-optical solution to the problem of information loss by the obstructing ring electrode-structure and the support rods is evident. In principle it would be sufficient to increase the focal length f of the objective lens to create a magnified image of the BFP. At a magnification M , the signal cut-on frequency (3.3) changes to

$$k_{cut-on}^{(M)} = \frac{d_o/2}{M \lambda f}, \quad (4.1)$$

Figure 4.1.: Ray optics of the diffraction magnification unit which is the core of the PACEM microscope. The additional transfer lenses generate a de-magnified 1st intermediate image and a magnified image of the diffraction pattern in the plane of the 2nd transfer lens. Within this magnified BFP, a miniature electrostatic einzel lens can be placed acting as a phase plate. If the diffraction pattern is magnified by a factor of 5, the amount of low-frequency signal loss would be dramatically decreased (cf. fig. 4.2). As the coefficients of spherical (C_s) and chromatic aberration (C_c) decrease proportionally with the focal length of the system, a corrector for the spherical aberration has to be incorporated above or below the DMU (not shown). The figure was kindly supplied by Marko Matijevic (Zeiss SMT).



i.e. it is decreased by a factor of M . With a magnification $M = 5 - 10$, even the current outer diameter of the ring electrodes (2.6-7.2 μm , see section 3.3) would be applicable for structural biology with minimal loss of low-resolution information. However, depending on the size of the unscattered beam, an increased central electrode opening will be necessary.

4.2 The concept of a magnified back focal plane

To realize a TEM optimized for imaging of biological phase objects, equipped with a Boersch-type electrostatic phase plate, the PACEM⁹ project has been initiated. Its technical design was based on the experimental results obtained from the first prototypes of the electrostatic phase plate, which are

⁹ phase contrast aberration corrected electron microscope. The PACEM is being built at the Max Planck Institute of Biophysics (Frankfurt am Main, Germany) in collaboration with the company Carl Zeiss SMT (Oberkochen, Germany).

documented in chapter 3. In the course of the project, a dedicated TEM is being designed and constructed, including two main components:

1. A diffraction magnification unit (DMU), consisting of an additional transfer lens doublet to generate a conjugate, magnified back focal plane (see fig. 4.1).
2. A double hexapole corrector (Haider 1998; Urban et al. 1999) to compensate the increase of spherical aberration by a factor of ~ 5 , caused by the increased effective focal length of the system.

The additional transfer lens system of the PACEM effects a de-magnification of the 1st intermediate image, thereby generating a magnified image of the diffraction pattern of the BFP, as shown in fig. 4.2. Within this magnified BFP, a miniature electrostatic einzel lens can be placed acting as a phase plate. If the diffraction pattern is magnified by a factor of 5, the cut-on frequency (cf. section 3.2.2) of the phase plate CTF would be increased by the same amount according to (4.1). This modification allows using the electrostatic einzel lens phase plate for molecular single particle reconstruction and cryo electron tomography for typical instrumental parameters (see table 2), almost without restrictions.

4.3 Image simulations assessing the contrast of the Boersch phase plate in a magnified BFP

The cut-on frequency of the electrostatic phase plate is increased to the order of several 10 nanometers by the diffraction magnification unit. Thus, the PACEM can be used for structural analysis e.g. by single particle imaging. Figure 4.3 shows simulated phase plate images of ribosome complexes embedded in vitrified ice. Assumed is a Boersch phase plate with the central ring electrode held by three support rods arranged in a non-centro-symmetric geometry, as shown in figs. 3.1 and 3.2. In-focus images are simulated for an ideal $\pi/2$ phase shift of the CTF, thus producing maximal phase contrast for spatial frequencies that are not affected by the ring electrode or the supporting rods. The image formation for a 5fold magnification of the diffraction pattern is compared to the results obtained with a conventional optics.

It is evident that with a the 5fold magnified BFP a nearly artifact-free image of the ribosome complexes with strong contrast can be obtained, even for ring electrode diameters of 7.2 μm (fig. 4.3 C,D), corresponding to the first functional prototype described in section 3.1.2. If the diameter is re-

duced to $2.6\ \mu\text{m}$ (fig. 4.3 F,G), which is already achieved for the never phase plate generations, the resulting image is a perfect representation of the projected molecular density. As opposed to the phase contrast produced by underfocusing, which show the typical blurring artifacts, the image mode combining phase plate, aberration corrector and DMU allows ideal transfer of the object information.

electrode diameter [μm]	cut-on [nm] $f = 3.0\ \text{mm}$	cut-on [nm] $f = 15\ \text{mm}$
7.2	3.1 / 2.1	15 / 11
2.6	8.5 / 5.8	43 / 29
2.0	11 / 7.5	55 / 38

Table 2. Low spatial frequency cut-on caused by the Boersch electrode with three different outer diameters, compared for a conventional TEM (typical focal length $f = 3.0\ \text{mm}$) and a TEM with 5fold magnified BFP ($f = 15\ \text{mm}$). Black numbers: acceleration voltage = 100 kV, red numbers: 200 kV.

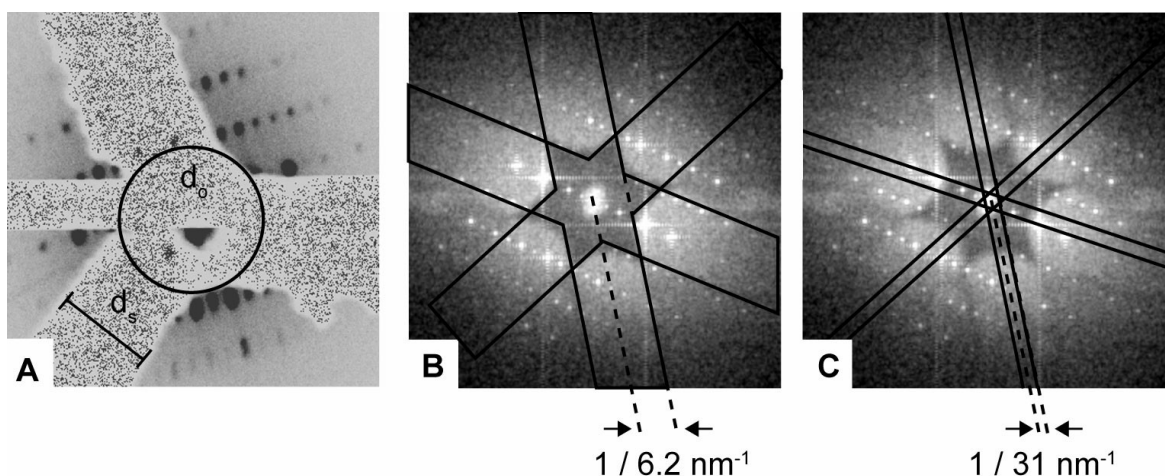


Figure 4.2: Impact of the geometry of the Boersch einzel lens phase plate on imaging of protein crystals. (A) Diffraction pattern of a bovine catalase crystal (unit cell $a=6.9\text{nm}$, $b=17.3\text{nm}$) recorded on a CCD camera with 100 kV and a focal length of 3 mm. The region obstructed by the phase plate structure is clearly visible. The diameters of the ring electrode ($d_o = 2.6\ \mu\text{m}$) and the support rods ($d_s = 2.3\text{mm}$) are indicated. (B) Power spectrum of an image of the same object. The spatial frequency domain obstructed by the ring electrode appears entirely black, indicating a complete loss of signal. The structure factors which are affected by the support rods and therefore transferred with single-sideband contrast are outlined by black lines. (C) Power spectrum from B, overlaid with the obstruction pattern of a 5fold magnified BFP. Compared to B, the obstructed portion of the diffraction pattern is now minimal, thus permitting the transfer of nearly all structure factors with maximal phase contrast.

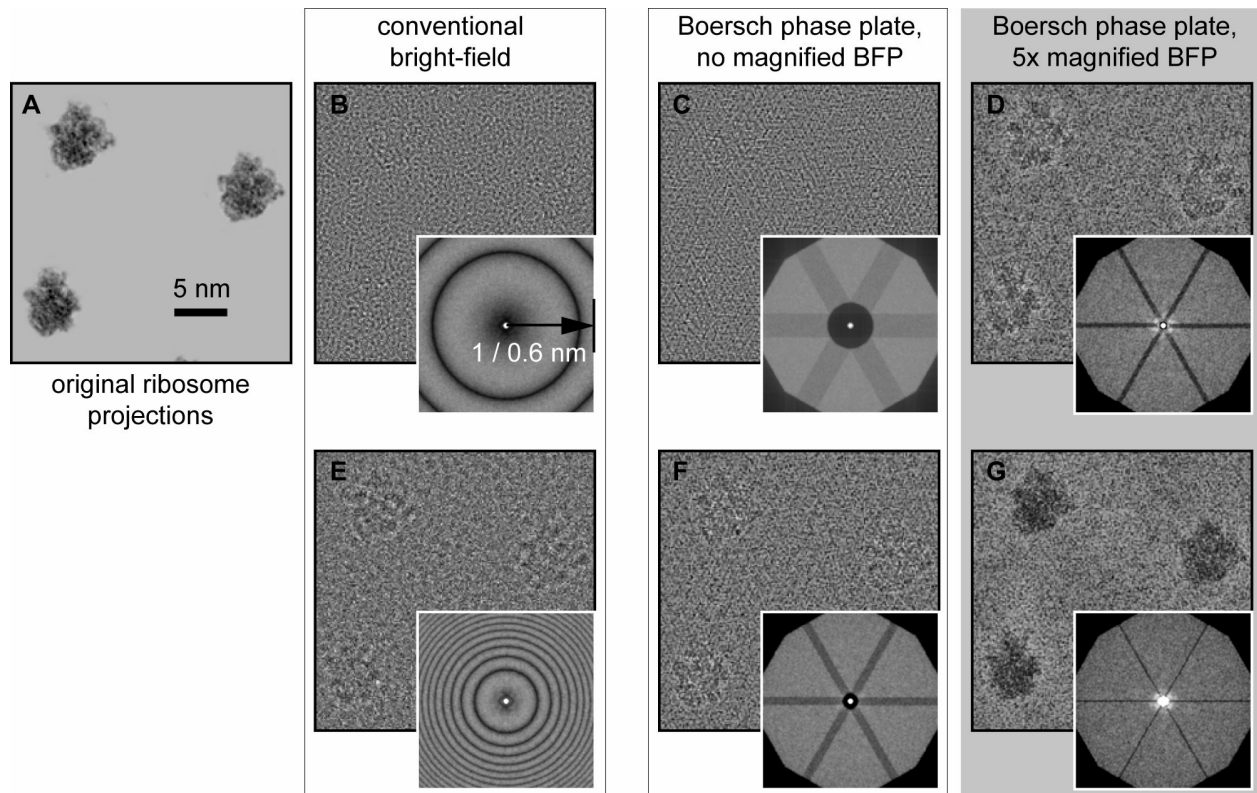


Figure 4.3.: (A) Projections of ribosome complexes (EMD entry 1055). (B-G) Simulated images for a 200 kV TEM with $f=3.0$ mm and $C_S=2.2$ mm, assuming an ice embedding corresponding to 10% noise. (B,E) Conventional image contrast without phase plate generated by a low underfocus (200 nm, B) and medium underfocus (1,000 nm, E). (C,F) In-focus images obtained by a Boersch phase plate with 3fold geometry as described in section 3.2. A perfect 90° phase shift of the pCTF is assumed. For an electrode outer diameter of $7.2 \mu\text{m}$, corresponding to the first functional prototype of the phase plate, the particle outlines completely vanish in the image. The signal loss is reflected in the black ring at the origin of the power spectrum (inset), indicating the complete loss of low spatial frequencies. (F) For a reduced outer lens diameter of $2.6 \mu\text{m}$ the contrast is slightly improved. (D,G) Simulations assuming the same phase plates as in C and F, being placed in a 5fold magnified BFP ($f=15$ mm). The spherical aberration is adjusted to the same value used in B-F, which can be achieved by incorporating a C_S tuner (see text). For both designs, the ribosome particles can now be clearly distinguished from noise. (G) For the design with the small electrode, which was already fabricated for this work, a nearly ideal projection of the object can be obtained in the image (cf. A). The completeness of the structure factor transfer can be seen from the power spectrum, where only a negligible portion is affected by rods or electrode ring.

4.4 Reducing the aberrations of the transfer lenses

The values of spherical and chromatic aberrations of the lens system, C_S and C_C , roughly scale proportionally to the focal length f . For a typical TEM objective with $f=3.0$ mm and $C_S=2.2$ mm, the latter would be increased to ~ 11 mm. A large C_S leads to unwanted oscillations of the oth-

erwise ideal phase plate pCTF (cf. (3.5)) and, in addition, gives rise to a damping of high spatial frequencies in the image spectrum (cf. (2.28)). This is not tolerable, as the resolution limit of the PACEM instrument is aspired to be in the order of ~ 0.2 nm to allow e.g. for high resolution macromolecular imaging.

Therefore, a corrector element for the spherical aberration is incorporated in the design. Such a lens systems, including of two magnetic hexapole lenses, is commercially available (CEOS GmbH, Heidelberg, Germany). It allows for adjusting C_S to a wide range of values, especially to zero and negative values (Uhlemann and Haider, 1998). The corrector can be incorporated in the optical ray path before or after the DMU (not shown). Either the (positive) spherical aberration generated by the DMU is compensated by the C_S corrector (negative C_S), or vice versa. If the increase in C_S caused by the magnification of the BFP can be compensated by the corrector, a near-perfect imaging of biological phase objects can be achieved (fig. 4.3 D,G).

On the other hand, the chromatic aberration coefficient C_C will also be increased by the DMU. In fig. 4.4, the form of the chromatic envelope for such a microscope is plotted according to (2.28). If an increase of C_C from 3.4 mm to 17 mm is assumed, which is realistic, the information limit would drop to ~ 0.2 - 0.3 nm. Although this is not a drawback for biological applications, an optimized TEM with Boersch phase contrast therefore needs to incorporate a C_S and C_C corrector, both of which are in principle available (Haider and Müller 2004).

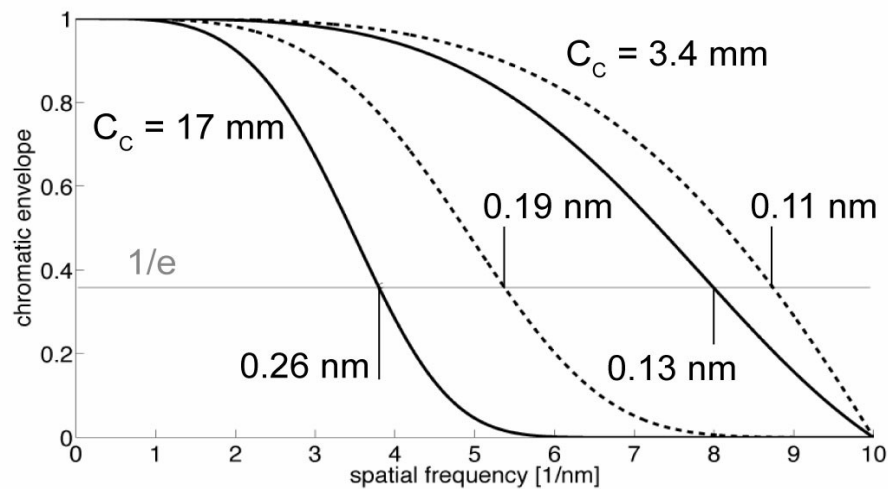


Figure 4.4.: Chromatic envelope of the CTF (see section 2.1.7) compared for a typical conventional TEM ($C_c = 3.4$ mm) and a TEM with 5fold increased focal length ($C_c = 17$ mm). Solid lines: beam energy spread 0.3 eV, dashed lines: 0.15 eV. The information limits, where the CTF amplitude drops below $1/e$, are indicated.

4.5 Design, manufacturing and test of a precise phase plate positioning system

To allow the application of the Boersch phase plate in the PACEM for biological low-dose imaging techniques, a reliable, precise and stable positioning system for the phase plate had to be designed. The ring electrode with a typical diameter of ~ 1 μm has to be aligned to the optical axis with a precision of a few 10 nm, and drift of the phase plates during image series acquisition has to be avoided. A suitable device, of which two prototypes are already being tested, is shown in fig. 4.5. It is based on a piezo-driven in-column stage mounted inside a modified vacuum flange that can be attached to the TEM column. Three slick-and-slide piezo drives allow the translational positioning of the phase plate in lateral (x and y) and beam direction (z) with a precision of a few nanometers (Lengweiler 2005). The range of movement is ~ 5 mm in y and z, and ~ 20 mm in x direction which allows to full retract the holder tip from the beam path if the phase plate is not needed. Two phase plates at a time can be mounted onto the tip of the holder. First test runs show that the lateral drift of the phase is minimal (see appendix C). By moving the tip with the z axis, the phase shifting electrode can be precisely adjusted to the height of the BFP, i.e. to the beam crossover of the 1st DMU transfer lens (see fig. 4.1).

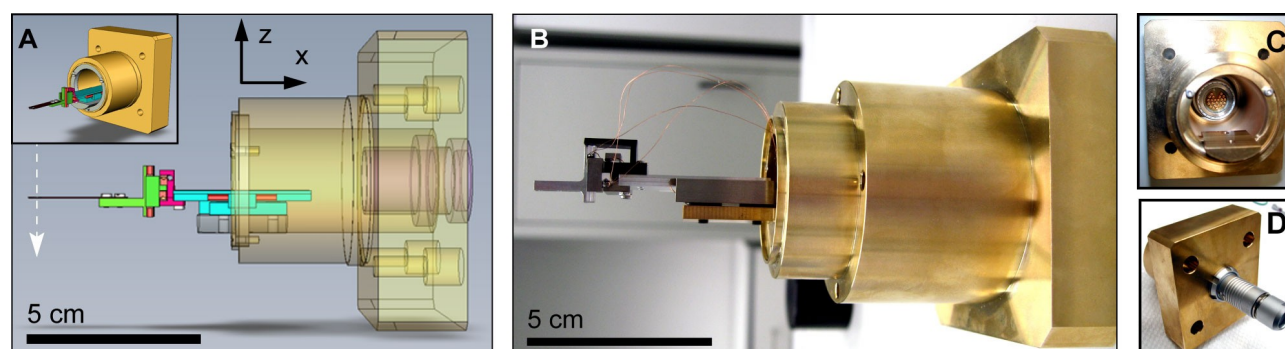


Figure 4.5.: Piezo-driven phase plate positioning system with three translational axes (x,y,z). The device was specially designed for positioning of the electrostatic phase plate in the magnified BFP of the PACEM, permitting an accuracy of a few nm. (A) Side view of the initial CAD construction. The vacuum flange (brass colored) is attached to the microscope wall. Two microscopic Boersch phase plates are mounted onto the tip of the holder and can be precisely aligned to the beam axis (dashed arrow). The phase plate can be moved by slick-and-slide piezo drives in x (light blue), y (magenta) and z direction (green). (B) Prototype for the PACEM with no phase plates mounted. The required bias voltage for the two phase plates is supplied by thin wires with an insulating coating. (C) Front view of the flange without piezo drives. The vacuum feed-through for the piezo and phase plate voltages can be seen. (D) Rear view of the flange with attached connector plug. For more details see appendix C.

4.6 Conclusion

In the course of the PACEM project, a novel TEM is being designed and constructed that combines the Boersch electrostatic phase plate with a diffraction magnification unit and a spherical aberration corrector. Image simulations show that if the the diffraction pattern can be magnified by a factor of 5 and the increase of C_s is compensated by the corrector, near-perfect images of ice-embedded protein complexes can be obtained. Although the resolution of the system will be initially limited to 0.2-0.3 nm owing to the increased chromatic aberration, this does not compromise the analysis of native biological specimens. A precise and stable in-column piezo positioning device for the phase plates was designed and constructed, providing practical ease-of-use of the system. The PACEM fully exploits the optimal phase contrast of the Boersch phase plates, while almost entirely removing the problem of signal obstruction by the einzel lens and the support rods.

5 Obstruction-free Phase Contrast: The Anamorphic Phase Plate

The problem of low-resolution signal loss by the Boersch phase plate can be dramatically reduced by magnifying the BFP as described in chapter 3. However, it is desirable to avoid those obstruction effects completely. Therefore, a novel electrostatic phase plate is proposed in this chapter. Instead of using special structures for confining the electric fields, a highly anisotropic field distribution is employed, which is placed at an anamorphic image of the diffraction plane, i.e. in a plane where the diffraction image is compressed in one direction. The field shifts the phase of a thin stripe of the electron wave. Here, simulated phase contrast images for different modes of operation are shown along with a first prototype.

5.1 Is a matter-free electrostatic phase plate possible?

For a general TEM phase plate, the phase shift Φ of the electron wave in the BFP can be written as the projection of the 3D potential distribution ϕ :¹⁰

$$\Phi(\mathbf{k}) = \frac{\pi\chi}{\lambda U_0} \int \phi(\mathbf{k}, z) dz, \quad \mathbf{k} = (k_x, k_y). \quad (5.1)$$

χ is the relativistic constant described in section 2.1.2. It is assumed that the electron rays travel in the direction of the optical axis. This is a good approximation as the scattering angles are in the order of mrad for acceleration voltages of a few hundred kV. To realise a Zernike phase plate, a “dip” in the lateral phase distribution Φ around the origin of the BFP with $|\mathbf{k}|=k=0$ is required, so that

$$\Phi_z(k) = \begin{cases} 0 & k = 0 \\ \pi/2 & k \neq 0 \end{cases} \quad (5.2)$$

is approximated. The requirement for a Hilbert phase plate is somewhat less demanding: here, an “edge” of the phase shift in one direction is needed:

¹⁰ This is not valid for phase plates based on magnetic fields (Nagayama 2005).

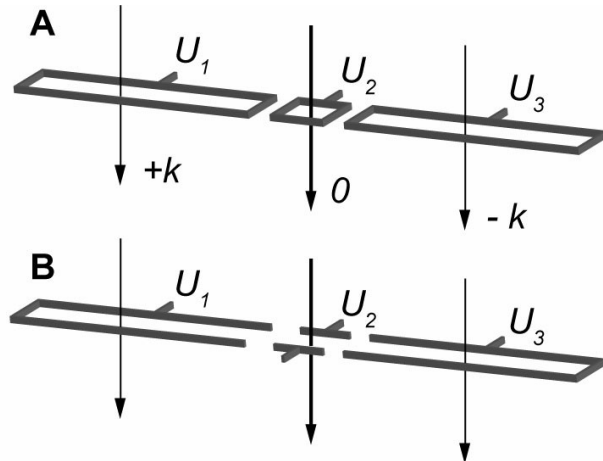
$$\Phi_H(k_x) = \begin{cases} 0 & k_x \leq 0 \\ \pi & k_x > 0 \end{cases} \quad (5.3)$$

The necessary potentials can be generated by placing a charge distribution $\rho(\mathbf{k}, z)$ in the BFP, as expressed by the Poisson equation $\nabla^2 \phi(\mathbf{k}, z) = -4\pi \rho(\mathbf{k}, z)$. Expressed in terms of the lateral phase shift distribution, this can be rewritten as

$$\left(\frac{\partial^2}{\partial k_x^2} + \frac{\partial^2}{\partial k_y^2} \right) \Phi(\mathbf{k}) = -4\pi \varrho(\mathbf{k}). \quad (5.4)$$

The potential is assumed to be symmetric on both sides of the BFP; $\varrho(\mathbf{k})$ is the projection of the charge distribution along the beam axis. In case of a Hilbert- or Zernike thin-film phase plate, the charge distribution is represented by a carbon film with a mean inner electric potential (cf. section 2.2.1). The Boersch electrostatic phase plate generates the required potential dip inside the charged central ring electrode (see fig. 3.2).

Figure 5.1.: (A) Electrostatic phase plate with three closed electrodes placed in the BFP, held on different potentials. It was shown that the phase shift of electron waves travelling through each electrode is always constant, so that a constant relative phase shift between scattered ($\pm k$) and unscattered (0) rays can be achieved. (B) A slightly modified design with open electrodes. While the phase shift will be approximately the same as in A, no obstructing material is present within the slit.



For a matter-free phase plate, the central part of the BFP has to be also charge-free, so that

$$\left(\frac{\partial^2}{\partial k_x^2} + \frac{\partial^2}{\partial k_y^2} \right) \Phi(\mathbf{k}) = 0. \quad (5.5)$$

It can be easily shown that under this condition neither local minima, as required to realise an electrostatic Zernike phase plate, nor a one-dimensional “jump” of the lateral phase shift forming a Hilbert phase plate, can be generated. In fact, it was proven theoretically (Matsumoto and Tonomura 1996) and experimentally (Barton 2005) that the phase shift within a closed electrode (fig. 5.1 A) will always be constant if the lens effect is negligible. This was confirmed by the einzel lens experiments described in section 3.1.2.

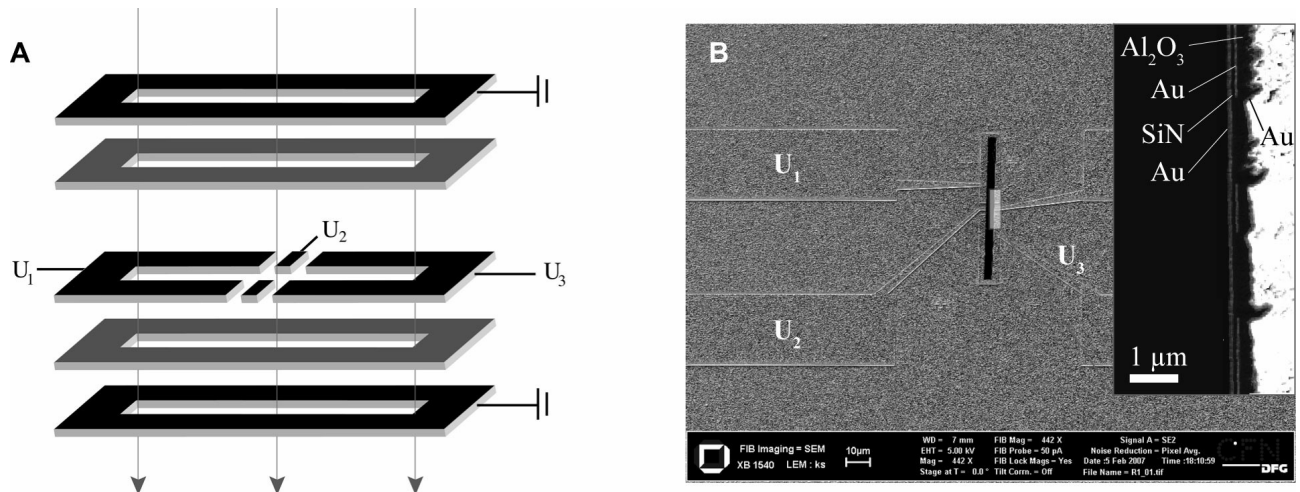


Figure 5.2.: (A) Schematic 5-layer structure of a prototype for the anamorphic phase plate. The central layer of conducting material (black) is divided into three areas, that are held at different potentials U_1 , U_2 and U_3 . The resulting inhomogeneous potential distribution in the areas framed by the respective electrodes will lead to relative phase shift of electron rays travelling through the U_1 , U_2 and U_3 areas. By applying appropriate voltages, obstruction-free Hilbert- and Zernike-type phase plates can be realised (see fig. 5.4). (B) SEM image of a prototype for the anamorphic phase plate (Katrin Schultheiß, University of Karlsruhe). Voltages $U_{1/2/3}$ are supplied by conducting paths, as indicated. The anamorphic electron beam passes through the slit without any obstruction. The 5-layer structure (inset) to avoid stray fields is the same as for the Boersch-type phase plates as described in chapter 3.

5.2 The concept of the anamorphic phase plate

A good approximation to a charge-free electrostatic phase plate can be realised by a slit with high aspect ratio as drawn in fig. 5.1 B, containing three independent electrode potentials along its long axis. The projected potential, i.e. the phase shift will gradually change when going outward from the central electrode on potential U_2 towards the outer electrodes, held on potentials U_1 and U_3 , respectively. However, this variation can become relatively abrupt if the electrode dimensions are on the micrometer scale, thus approximating an electrostatic Hilbert ($U_1 = U_2 \neq U_3$) or Zernike ($U_1 = U_3 \neq U_2$) phase plate. By maintaining a high aspect ratio of the slit, i.e., a small diameter in

k_y direction, the unwanted variation of the phase shift in k_y becomes negligibly small.

However, the functionality of such an “anamorphic” phase plate (APP) is based on a diffraction pattern with vanishing diameter in k_y direction, while having the full extend in k_x direction to allow for the phase manipulation. The originally round pattern has to be optically converted into an ellipse, with an aspect ratio in k_x and k_y comparable to that of the electrode slit. To obtain such an anamorphic diffraction pattern, an image of the BFP has to be de-magnified in k_y , and at the same time magnified in k_x direction. A simplified ray path for a suitable lens system, including 16 magnetic quadrupoles, is illustrated in fig. 5.3 (p.68). A similar arrangement is used to realise a combined corrector element for chromatic (C_C) and spherical (C_S) aberration (Haider and Müller, 2004; Rose, 2004).

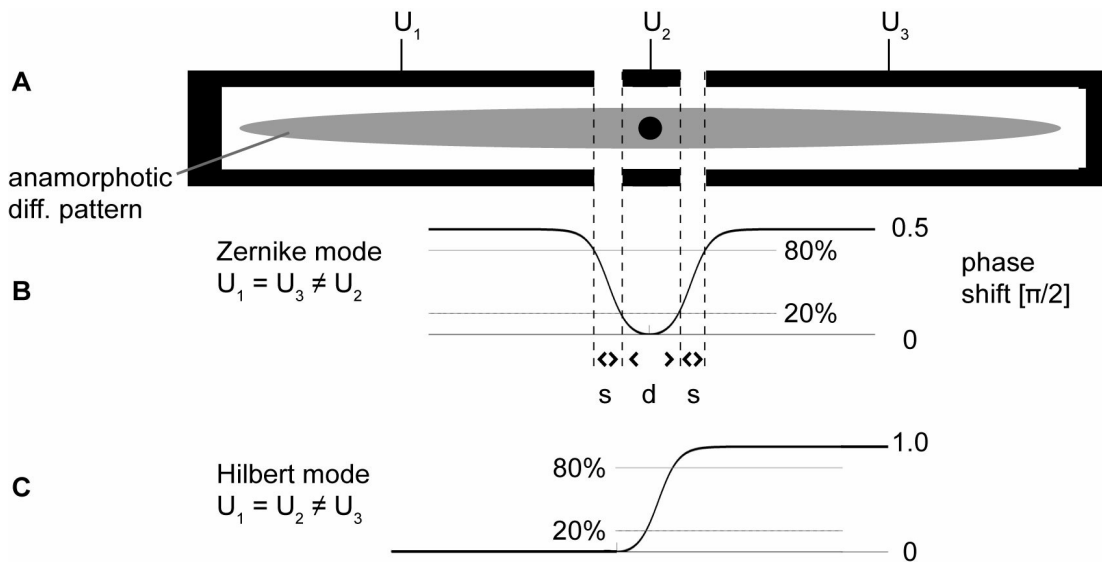


Figure 5.4.: Modeling the potential distribution inside the slit of the anamorphic phase plate. (A) Central layer of the 5 layer electrode structure. An anamorphic diffraction pattern (grey) is generated by multiple magnetic quadrupole lenses (cf. fig 5.3). (B) Potential along the long axis of the slit modelled by a double Fermi edge. To realise a Zernike phase plate, two subsequent, perpendicular anamorphic diffraction patterns have to be created, and three independent electrodes are needed. The phase shift for each plane is then $\pi/4$. (C) For the Hilbert mode, only one anamorphic plane and only two electrodes are required to shift the phase in one half of the BFP by π .

An appropriate technical implementation of an anamorphic phase plate is shown in fig. 5.2 A, together with a preliminary prototype (fig. 5.2 B). The prototype was fabricated at the Laboratorium für Elektronenmikroskopie of the University of Karlsruhe. Apart from the different lateral geo-

metry, the slit has the same 5-layer structure as the Boersch electrostatic einzel lens (cf. fig 3.2) to avoid fringing fields. In contrast to the round einzel lens, the central conducting layer of the “anamorphic phase plate” (APP) contains two or three independent electrodes (fig. 5.4 A). By holding these on different potentials, a Hilbert phase plate with one step of $\Phi(k_x)$ (fig. 5.4 C) or a Zernike phase plate with two steps (fig. 5.4 B) can be realised. While for the Zernike mode, three independent electrodes are needed, two electrodes are sufficient to operate the device in Hilbert mode.

The advantage of the matter-free anamorphic phase plate is clear: There is no coherence loss, as in the case of carbon film phase plates, and no obstruction of low spatial frequency signal, as it is caused by the ring electrode of the Boersch phase plates described in chapter 3. All electron rays emerging from the specimen travel through vacuum, and thus the complete object information is transferred to the image with optimal contrast. Moreover, an APP brings the flexibility to be operated in Zernike- and Hilbert mode by adjusting the potentials of the three independent electrodes accordingly (fig. 5.4 B/C).

As outlined in fig. 5.3 (p. 68), designs for state-of-the art aberration correctors principally include two elliptical diffraction planes with an aspect ratio of $\sim 1:10$. For the application of an anamorphic phase plate, this aspect ratio should be increased to $\sim 1:30$ by addition of appropriate multipole lenses (Schröder et al. 2007). As the APP leaves a stripe of spatial frequencies $k_x < g \approx (d/2 + s)/(\lambda f)$ largely unaffected (fig. 5.4 B), two perpendicular APPs operated in Zernike mode can be placed inside the two anamorphic diffraction patterns depicted in fig. 5.3. If each instance of the phase plate shifts the relative phase of zero and scattered beams by $\pi/4$, the resulting $pCTF(\mathbf{k}) = \sin\{\Phi(\mathbf{k})\}$ becomes

$$pCTF(k_x, k_y) = \begin{cases} 0 & k_x, k_y < g \\ 1 & k_x, k_y > g \\ 0.71 & \text{else.} \end{cases} \quad (5.6)$$

For simplicity, it is assumed that the spherical aberration coefficient is adjusted to zero by means of a C_s corrector. This phase contrast transfer is an excellent approximation to a perfect Zernike phase plate.

5.3 Simulating in-focus anamorphic phase contrast imaging

To quantify the contrast generated by an obstruction-free anamorphic phase plate for a biological

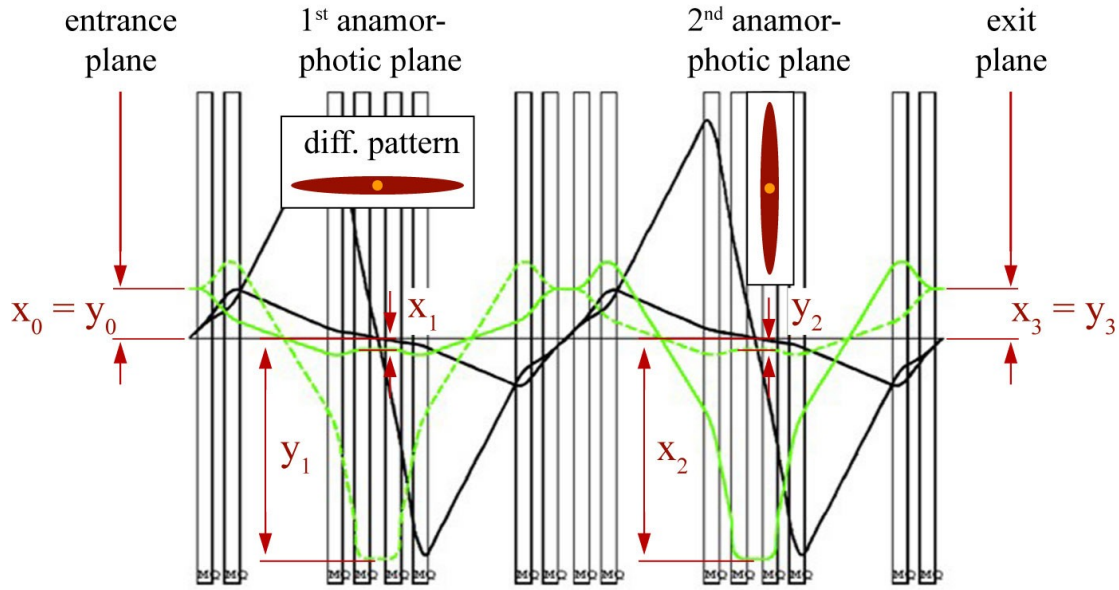


Figure 5.3.: Principle of an electron optical element consisting of 16 magnetic quadrupole lenses, generating two subsequent, perpendicular anamorphic diffraction planes. The green curve shows the distance of the principal rays from the optical axis in x (solid curve) and y (dotted curve) directions.

frozen-hydrated specimen, images of Ribosome complexes were simulated (cf. section 4.3). Simulations were carried out for a single APP in Hilbert mode as well as for a pair of perpendicular APPs in Zernike mode (Schröder et al. 2007). The potential in slit (k_x) direction was modelled by two symmetrical Fermi step functions, as plotted in fig. 5.4 B and C:

$$\Phi(k_x) = S_- \left[1 + \exp\left\{\frac{-k_x + g}{T}\right\} \right]^{-1} + S_+ \left[1 + \exp\left\{\frac{k_x - g}{T}\right\} \right]^{-1}. \quad (5.7)$$

For a Hilbert APP, the scaling factors were set to $S_- = 0$, $S_+ = \pi / \max\{\phi(k_x)\}$, and to $S_+ = S_- = (\pi/2) / \max\{\phi(k_x)\}$ for the Zernike mode. The temperature factor T was adjusted so that the phase shift reaches a value of 80% at the cut-on frequency $g = (d/2 + s)/(\lambda f)$, corresponding to the rim of the outer electrodes:

$$T = \frac{g}{\ln(1/0.8 - 1)}. \quad (5.8)$$

The resulting phase contrast transfer functions for the Hilbert mode are plotted in fig. 5.5. Figure 5.6 shows simulated images of native ribosome particles embedded in vitrified ice (fig. 5.6 A), using the phase shift model in (5.7). For comparison, a conventional underfocus image (fig. 5.6 B) and an in-focus image obtained with a Boersch phase plate without magnification of the BFP (fig.

5.6 C) are also shown. In the Boersch image, the ribosomes can be hardly distinguished from the surrounding noise owing to the obstruction of low spatial frequencies by the ring electrode structure (cf. section 3.2.2). This situation is substantially improved already for APPs with relatively large diameters of the central electrode of 2 μm (fig. 5.6 D,G). Both Hilbert- and Zernike-type APPs yield a good representation of the individual particles, with strong in-focus contrast.

5.4 Implications on the technical design

The image simulations for frozen-hydrated protein complexes show that an anamorphic phase plate operated in Hilbert mode yields strong phase contrast. The spatial frequency transfer is practically equivalent to that obtained with a pair of crossed APPs in Zernike mode (fig. 5.6 F,I). As a result of the asymmetric potential distribution in the BFP, Hilbert APP images are convolved with an anti-symmetric PSF artefact (see section 2.2.2). As will be shown in chapter 6, this artefact can be eliminated numerically, thus yielding a near-isotropic, artefact-free, strong contrast image. From a technical point of view, the Hilbert version seems to be preferable: It requires only two physical electrodes and does not require the difficult fabrication of the delicate central electrode (U_2 in fig. 5.2 A) which is only $\sim 1\mu\text{m}$ in diameter. Although a prototype including three independent electrodes has already been fabricated, a higher mechanical and electrical stability is expected for the simplified Hilbert design with only two “macroscopic” electrode pads.

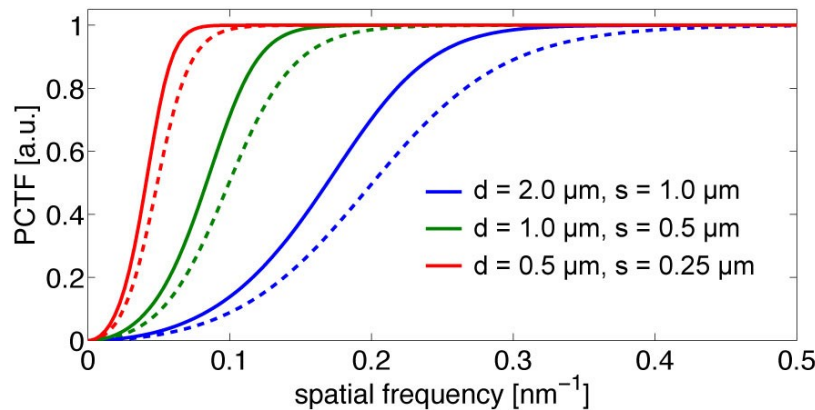
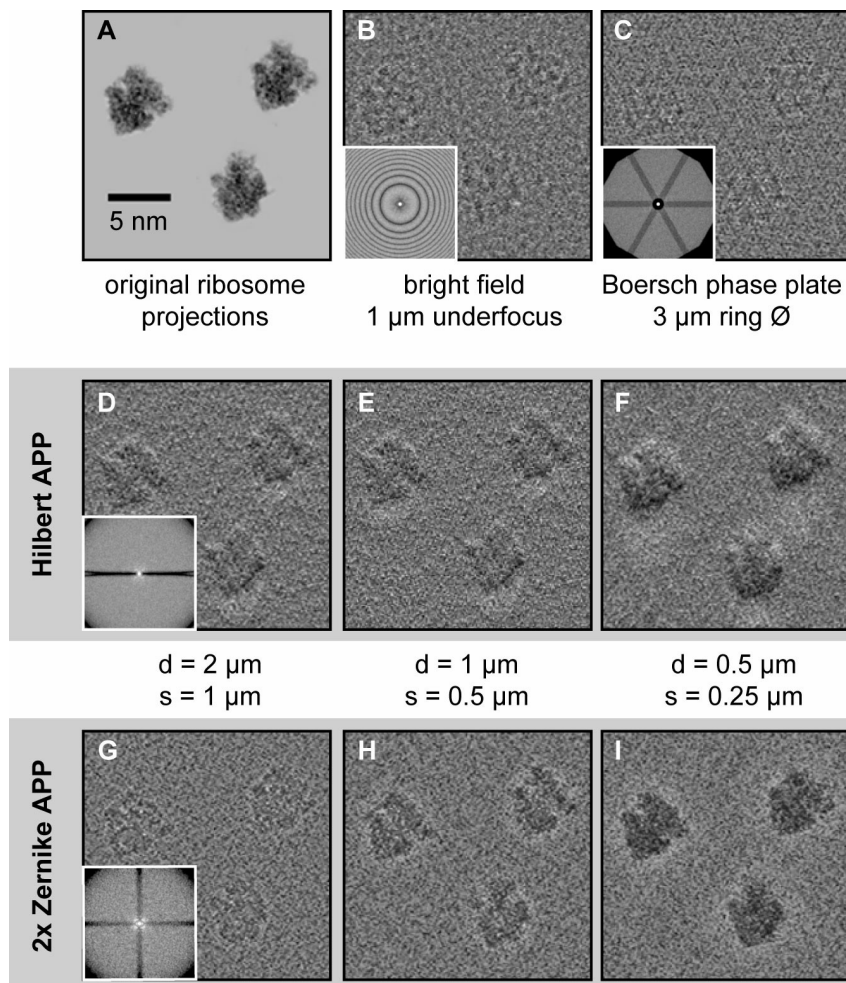


Figure 5.5.: Phase contrast transfer functions (pCTFs, solid curves) and phase shifts (dashed curves) for an anamorphic phase plate (in slit direction), used in a 200 kV TEM with $f = 3.0$ mm. Curves for three different electrode sizes are shown, assuming the potential model described in fig. 5.4. For the smallest design with $d = 0.5$ μm and $s = 0.25$ μm , no further magnification of the anamorphic BFP in slit direction will be needed to obtain good contrast for resolutions < 10 nm.

Figure 5.6.: Image simulations comparing an obstruction-free anamorphic phase plate applied in a 200 kV TEM ($f=3.0\text{mm}$, $C_s=2.2\text{mm}$) to other forms of phase contrast. (A) Ribosome projections (EMD entry 1055). (B) Conventional bright-field image with $1\ \mu\text{m}$ underfocus. (C) Boersch phase contrast image using a round electrostatic einzel lens with $3\ \mu\text{m}$ ring diameter (see chapter 3). (D-F) Asymmetric contrast produced by a single anamorphic phase plate in Hilbert mode, using various electrode dimensions. (G-H) Near-isotropic contrast obtained by a pair of perpendicular Zernike APPs. The crossed Zernike mode yields the best representation when compared to A, but requires three physical electrodes and two anamorphic diffraction planes.



5.5 Conclusion

This chapter presents the concept of an obstruction-free electrostatic phase plate, based on an inhomogeneous electric potential distribution generated within an anamorphic diffraction pattern. Simulations show that such an anamorphic phase plate (APP) produces strong in-focus phase contrast and avoids the disadvantage of low spatial frequency obstruction common to the einzel lens implementations. An anamorphic phase plate requires an elliptical diffraction pattern with a high aspect ratio of 10:1 – 30:1. Such anamorphic diffraction planes can be generated by a multi-quadrupole aberration corrector. This allows to mount the novel phase plate inside future state-of-the-art TEMs with minor modifications. A first prototype has been fabricated, suitable for operation of the device as an

electrostatic Zernike- and Hilbert-type phase plate. For future functional APPs, the fabrication as a Hilbert type with only two adjacent electrodes is preferable because of its higher stability and the lower effort for manufacturing.

6 Electron Tomography and Cryo TEM with Hilbert Phase Plates: an Application Study

In chapter 5, the concept of the obstruction-free anamorphic phase plate is described. It is expected that the technical implementation is simplified if the device is operated in Hilbert contrast mode. In this chapter, an application study for a carbon film Hilbert phase plate for electron tomography (ET) is presented. In ET, the low SNR in images of unstained specimens recorded with conventional underfocus phase contrast makes it difficult to interpret the obtained 3D volumes. This problem can be partially solved by applying a Hilbert phase plate for tomography. The Hilbert phase plate provides strong positive phase contrast which - in principle - extends to the information limit of the microscope. It is demonstrated that the anti-symmetric Hilbert phase contrast (HPC) can be numerically converted into isotropic contrast, which is equivalent to the contrast obtained by an ideal Zernike phase plate. The first electron tomograms of biological specimens reconstructed from in-focus HPC image series are presented in this work. The technical implementation of the phase plate is outlined, and it is demonstrated that the technique is routinely applicable for tomography. A comparison between conventional defocus tomograms and in-focus HPC volumes shows an enhanced SNR and an improved specimen visibility for in-focus Hilbert tomography.

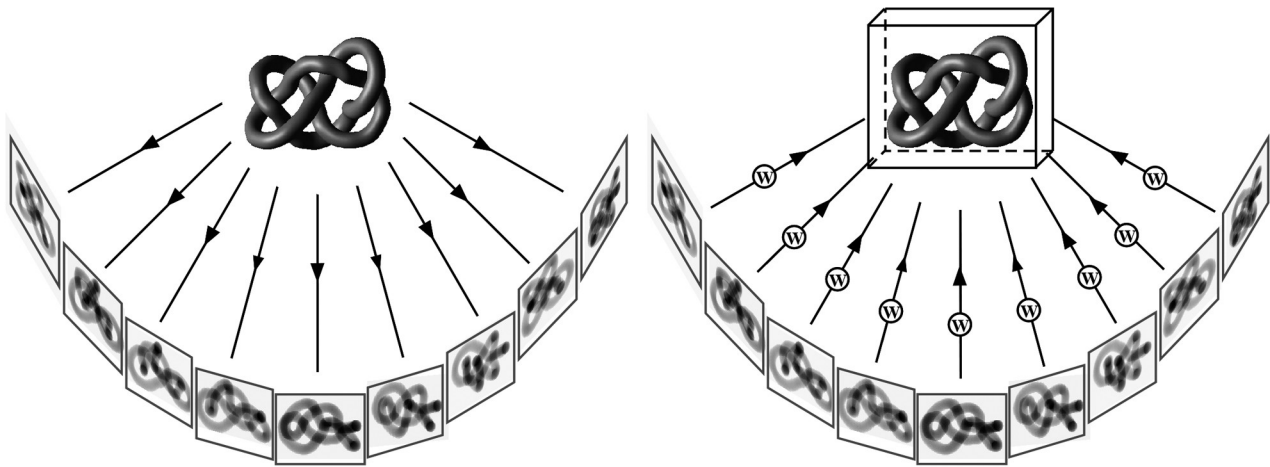


Figure 6.1.: The principle of tomography. A series of projection images of an object from different angles is recorded (“tilt series”). The 3D object reconstruction is then obtained by numerical back projection of the image series.

6.1 Phase contrast in biological electron tomography

The principle of electron tomography and cryo electron tomography (CET), i.e. ET of frozen-hydrated or freeze-sectioned samples, is illustrated in fig. 6.1. By ET, it is possible to reconstruct the 3D structure of a unique, amorphous object from a tilt series of projection images. A particular advantage of this technique is that the specimen density distribution in beam direction (z) can be resolved, which is not possible from a single projection image. Therefore, ET is usually applied to thick specimens. For example, frozen-hydrated cell organelles or thin parts of a whole cell with a thickness of up to 500 nm are analysed in CET (Jensen and Briegel 2007). The mechanism of contrast formation for such thick biological specimens will be considered in the following.

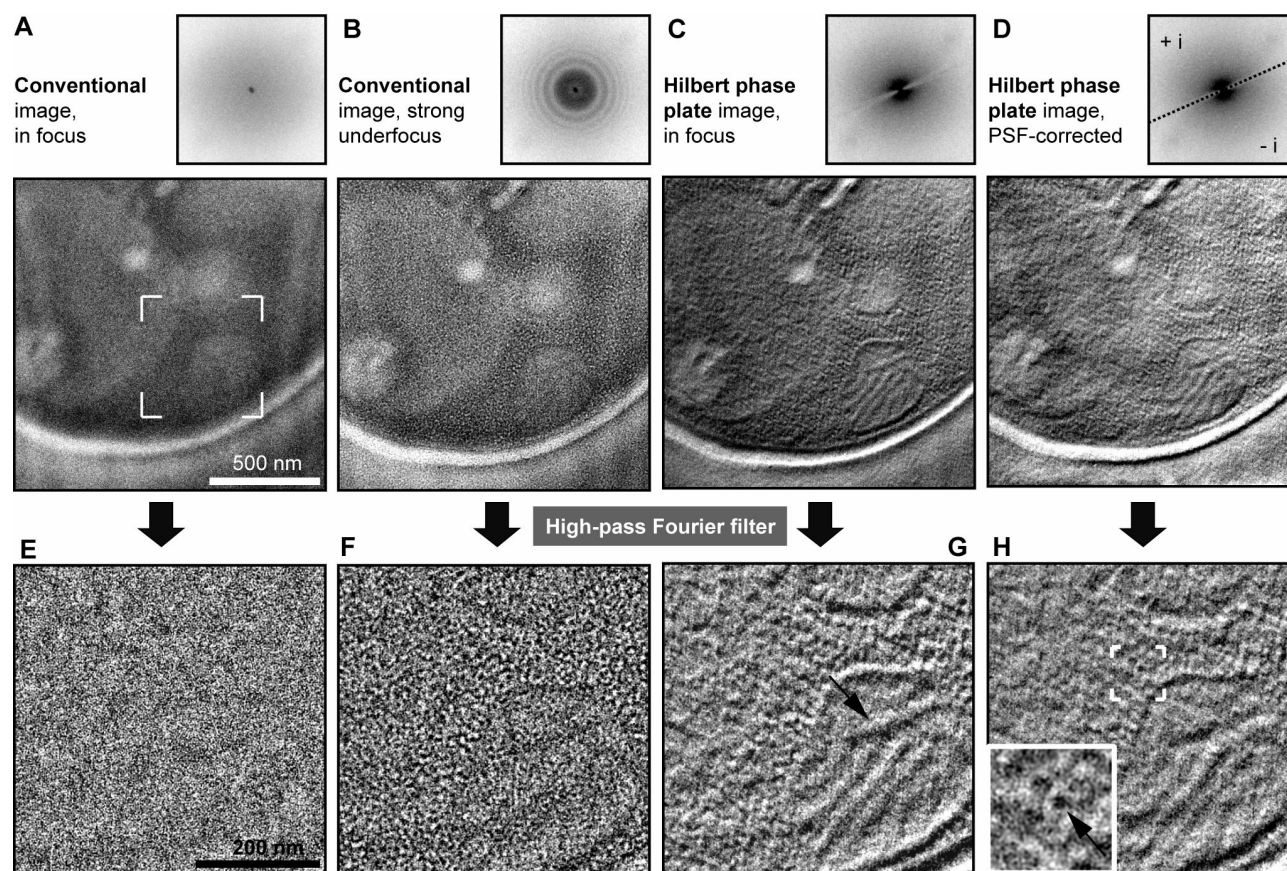


Figure 6.2.: Images of unstained, uncontrasted thin sections of resin-embedded *P. pastoris* cell sections (section thickness about 120 nm, primary magnification 13.3 kx) with and without a Hilbert phase plate. Unlike in frozen hydrated samples, the mass densities of the organic material and the embedding medium (London resin) are nearly the same, which further decreases phase contrast. (A) Image without phase plate close to focus. The low-resolution elastic amplitude and the inelastic zero-loss energy filter amplitude contrast (Angert et al., 2000) reveal few structural details. (B) Image recorded with high underfocus (approx. 15 μm). The contrast is increased, but the image shows point spread artefacts such as an over-pronounced granularity in the cytoplasm, most likely produced by the carbon support film. The structural resolution is compromised by the CTF oscillation, as indicated by Thon rings in the power spectrum inset. (C) Focused image recorded with a Hilbert phase plate in the BFP. (D) Same image as C after numerical PSF correction. (E – H) Close-up of the framed area in A, after removing all spatial frequencies below $1/300 \text{ nm}^{-1}$ in images A–D. The enclosed mitochondrion is invisible in the focused image (E), indicating that the image contains no higher-resolution phase contrast. The underfocus image (F) has faint contrast. In the HPC image (G), the mitochondrion and its cristae (arrow) are clearly visible. After Hilbert PSF-correction (H, see section 6.2.4), some objects in the cytoplasm can be distinguished (inset).

6.1.1 Assessing the phase contrast of thick specimens

The simulation described in section 2.1.5 implies that despite their thickness, image formation for typical CET samples follows the theory of a weak-phase object (fig. 2.2) Furthermore, the phase

signal $|\tilde{\eta}(\mathbf{k})|$ is significantly stronger than the amplitude signal $|\tilde{a}(\mathbf{k})|$. The data shown in fig. 6.2 prove that this holds especially for high resolutions: images of medium thick (~ 150 nm) sections of unstained, resin-embedded yeast cells are high-pass filtered in Fourier space. The bright field image recorded in Gaussian focus (fig. 6.2 A) is generated predominantly from amplitude contrast, as the phase contrast is $\sin W(k) \approx 0$ for $Z=0$ ¹¹. The corresponding high-pass filtered image, where the lowest resolutions ($< 1/(100$ nm)) are eliminated, contains nothing but noise (fig. 6.2 E). If, on the other hand, a phase contrast image is high-pass filtered, cellular features such as membranes and protein complexes can be recognised (fig. 6.2 F-H). The reason for this difference is that amplitude contrast is less localised than phase contrast, as it consists predominantly of filter contrast generated from removing the inelastic image (Schröder 1992; Angert et al. 2002). High-resolution information for thick biological specimens is almost entirely transferred via phase contrast (Han et al. 1995). Consequently, apart from a low-resolution amplitude contribution, such objects have to be treated as phase objects for high resolution imaging and tomography.

6.1.2 Limitations of defocus contrast CET

At present, a typical structural resolution of ~ 4 -5 nanometers is obtained in CET (Lucic et al. 2005), meaning the accuracy to which the final 3D reconstructions can be safely interpreted. Usually, a lower boundary for the resolution of 3D volume is stated which is often artificially imposed by Fourier low-pass filtering of the data (Frangakis and Förster 2004). An important goal of CET is to extend the resolution to a level where individual molecules can be recognised and distinguished by their shape (Bohm et al. 2000). It is generally expected that an isotropic resolution of 2-3 nm will be necessary for such shape recognition. At this level of resolution, the impact of the microscope PSF becomes a limiting factor. This is well known from single particle averaging work, where the correction for the CTF is imperative for reaching high resolution from strongly underfocused images.

As outlined in the previous section, the CTF for a thick, native biological sample can be approximated by a pure phase CTF:

$$pPCTF_c(k) = \sin W(k). \quad (6.1)$$

¹¹ Spatial frequencies > 1 nm⁻¹ can rarely be interpreted in CET, so that in this regime, phase contrast is indeed negligible if images are taken in focus ($Z=0$).

As shown in fig. 6.3, the $\sin W(k)$ contrast transfer produced with the conventional defocus method (underfocus $Z > 0$) is oscillating and approaching zero for low spatial frequencies. For CET, low resolution contrast is essential, e.g. to obtain continuous membrane structures within the reconstructed volume. As a consequence, tilt image series have to be routinely acquired with a high amount of underfocus ($Z = 5\text{--}20\ \mu\text{m}$). Thereby, a contrast transfer band at low spatial frequencies is generated to visualise extended features (cf. fig. 6.3).

However, the rapidly oscillating underfocus *cPCTF* contains signal transfer gaps and contrast reversals. As a consequence, only certain bands of spatial frequencies with alternating positive (black atomic density on white background) and negative (white on black) are represented in the image. Between these bands, close to the CTF zeros, the SNR is particularly low and object structure factors are lost. To reduce these artefacts caused by the *cPCTF*, tilt images for tomography are often low-pass filtered to the spatial frequency corresponding to the first transfer zero, which compromises the attainable resolution. Nevertheless, the object signal for low spatial frequencies cannot be restored, as $\sin W(k)=0$ for $k \rightarrow 0$. In addition, strong underfocusing gives rise to an attenuation of the CTF envelope (cf. (2.28) and Frank and Penczek, 1995). Even though it may be possible in the future to correct the contrast artefacts of the defocus CTF, its attenuating envelope function will still reduce the attainable resolution for tomograms recorded with strong defocus.

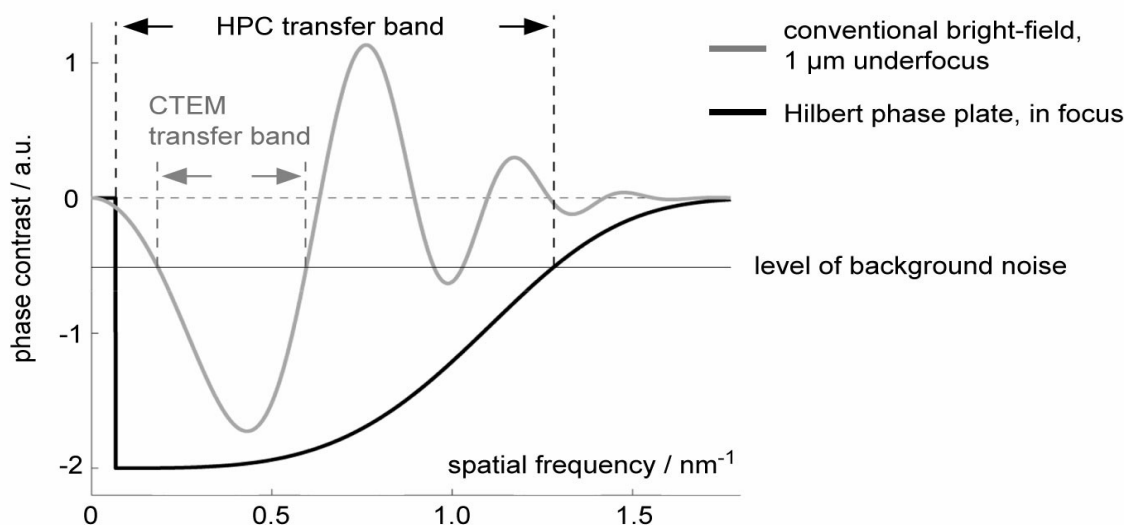


Figure 6.3.: Phase contrast transfer functions (pCTFs) for conventional phase contrast at $1.0 \mu\text{m}$ underfocus (200 keV electron energy, typical objective lens with $C_s = 2.2 \text{ mm}$) and Hilbert in-focus phase contrast (HPC). A phase plate gap corresponding to spatial frequencies below $1 / 15 \text{ nm}^{-1}$ was assumed.

6.1.3 Advantages of in-focus HPC tomography

To improve the contrast of weak-phase objects in CET, an in-focus technique for electron tomography was developed, using a Hilbert half-plane carbon film phase plate. In-focus HPC imaging can substantially improve the two major shortcomings of conventional defocus TEM (CTEM) for cryo tomography: the weak contrast of native frozen-hydrated specimens and the image artefacts generated by strong defocusing. Caused by the contrast reversals, the defocus pCTF potentially violates the projection requirement of tomography¹² (Twitchett et al. 2005). As opposed to the Zernike-type phase plate (section 2.2.1), the asymmetric Hilbert type provides greater ease-of-use for application in tomography. The carbon film half-plane is easier to manufacture, and likewise its alignment to the electron beam. Furthermore, a large number of Hilbert phase plates (50–100) can be loaded into the TEM vacuum column at the same time (see fig. 6.4 B and appendix B).

As shown in section 2.2.2, the Hilbert phase plate transfers the conventional sine pCTF into a cosine. Images recorded in focus with a phase plate contain strong contrast, reaching from the lowest (currently $\sim 50\text{-}100 \text{ nm}$) to the highest spatial frequencies in Fourier space. The corresponding

¹² In order to obtain a 3D reconstruction of an object by tomography, it is required that the detector signal (image grey values) is a monotonic function of a physical property (in this case, the object's inner electric potential \approx mass density).

phase plate PSF is particularly narrow, resulting in a well-defined object point representation. An anti-symmetric image artefact produced by the Hilbert phase plate can be corrected by simple image processing. As no further defocus artefacts arise, corrected in-focus phase contrast images represent a true projection of the object mass density with ideal phase contrast transfer. Consequently, tomograms represent a more faithful representation of the structure in question and can be interpreted more safely. For phase plate contrast imaging, there are no inherent resolution limits imposed by defocus CTF artefacts. In particular, low-pass Fourier filtering of the data, or difficult CTF correction to eliminate defocus artefacts, become obsolete.

6.2 Development of Hilbert phase plate tomography

It is clear from theory that the nearly ideal $\cos(0)$ contrast transfer of an in-focus Hilbert image is superior to the conventional underfocus imaging technique (fig. 6.3). To find out if the HPC can routinely be applied for tomography, it has to be tested on specimens that are typically used for CET, such as frozen-hydrated samples and embedded, unstained tissue sections. Using such phase objects, it must be investigated whether in-focus HPC is really as strong as expected, as compared to conventional phase contrast generated by underfocusing. Furthermore, the extent of the expected loss of coherent signal, caused by interactions of beam electrons with the phase plate, has to be quantified. Does it result in a reduction of the final SNR, or is the wave amplitude reduction compensated by the improved contrast transfer provided by the Hilbert phase plate? The advantages of the asymmetric Hilbert-type over the Zernike-type phase plate for application in CET, both theoretical and practical, will be outlined.

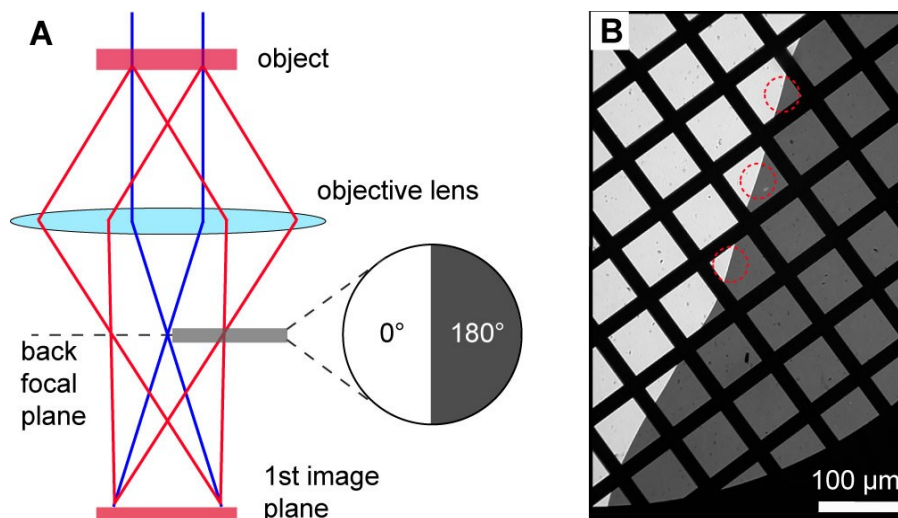


Figure 6.4.: (A) Ray paths in a Hilbert phase contrast TEM. A thin amorphous carbon film is positioned in the back focal plane of the objective lens, perpendicular to the beam axis. Its inner potential shifts the phase of one half-plane of the diffraction pattern by 180°. The edge of the film is positioned as close as possible to the central beam, without affecting its phase or amplitude. (B) Light microscopic image of a Hilbert carbon grid used as a set of phase plates. Inserting a standard specimen grid with an extended carbon edge has the advantage of a quick replacement of a contaminated phase plate area by simply shifting the grid by a few 10 μm along the edge. Assuming a diameter of the diffraction pattern of 20 μm, each square of a 300 mesh grid can provide up to three physical phase plates.

6.2.1 Implementation of Hilbert carbon film phase plates

The physical principle of the Hilbert phase plate is described in sections 2.2.1 and 2.2.2. To determine the carbon film thickness required to achieve a 180° phase shift of the electron wave, a mean inner potential of $U_i = 10.7 \pm 0.1 \text{ V}$ was assumed. This value was published by Harscher and Lichte (1998) and more recently by Wanner et al. (2006). The resulting thickness is 40.3 nm for a 200 kV- and 45.0 nm for a 300 kV TEM (cf. table 3). A large number of Hilbert phase plates was structured on a standard specimen grid to be loaded into the TEM at the same time (fig. 6.4). The fabrication process is described in more detail in appendix B.

It has to be mentioned that different values for the inner potential have been determined. The group of Danev and Nagayama applied a 64 nm thick Hilbert (180°) phase plate (Kaneko et al. 2005) and a 31 nm thick Zernike (90°) phase plate (Danev and Nagayama 2001). This implies that the value of $7.8 \pm 0.6 \text{ V}$ given by Reimer (1984) is used (cf. table 3). It has to be mentioned further that there is a considerable error in producing exactly the right thickness of the carbon film, so that a deviation

of 10-20% from the ideal 180° thickness has to be assumed. The effect of such thickness deviations will be considered in section 6.2.5.

electron energy / keV		120	200	300
Hilbert	180°	34.0 / 46.6	40.3 / 55.3	45.0 / 61.7
Zernike	90°	17.0 / 23.3	20.1 / 27.6	22.5 / 30.9

Table 3. Carbon film thicknesses in nanometers for Hilbert- and Zernike-type phase plates. Black numbers: $U_i=10.7$ V (Wanner et al. 2006), red numbers: $U_i=7.8$ V (Reimer 1984).

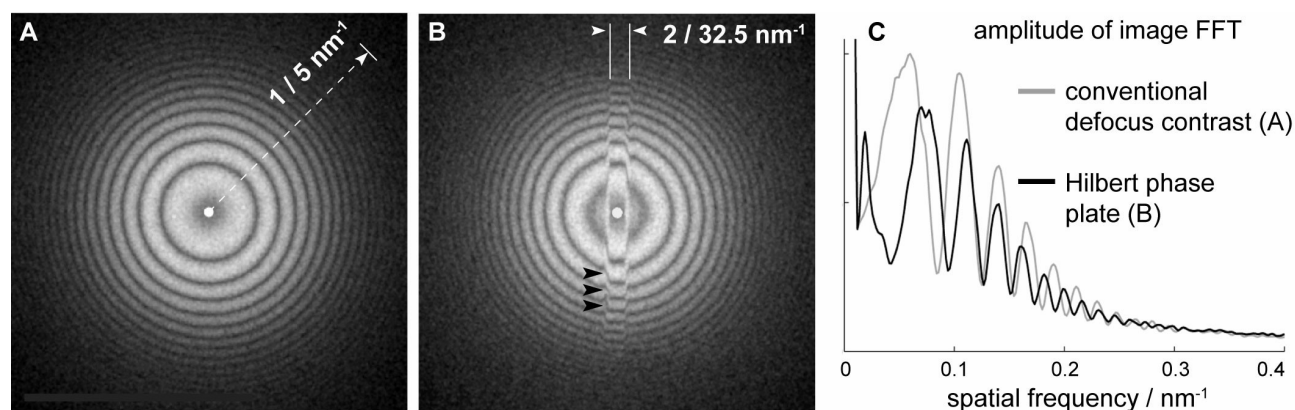


Figure 6.5.: (A) Power spectrum of a conventional 300 kV bright-field image of amorphous carbon film recorded with approx. $20 \mu\text{m}$ underfocus (41 kx primary magnification). The bright concentric Thon rings correspond to the contrast transfer maxima of the conventional $p\text{CTF}=\sin W(k)$. Dark rings indicate spatial frequency bands with vanishing signal. (B) Image of the same specimen area acquired with a Hilbert phase plate (≈ 50 nm thick) in the BFP of the objective lens. The Thon ring patterns in the “gap” region and the HPC region of the spectrum are inverted, indicating the $\sin \rightarrow \cos$ transition for the spatial frequencies influenced by the phase plate. (C) Radial intensities of the power spectra from A and B. The HPC signal (height of the $p\text{CTF}$ maxima above the noise background) is reduced by 29% with respect to the bright-field signal. The defocus of the images is slightly different, so that the $p\text{CTF}$ phase cannot be directly compared.

6.2.2 Experimental characterisation of HPC contrast transfer

The contrast transfer function for HPC is deduced mathematically in section 2.2.2. If the sine term in (2.39) is left out for simplicity, the corresponding Hilbert $p\text{CTF}$ is

$$pCTF_H(\mathbf{k}) = \begin{cases} \sin W(k) & k_x < g \\ -\frac{1+a_H}{2} i \operatorname{sign}(k_x) \cos W(k) & k_x \geq g. \end{cases} \quad (6.2)$$

The gap width $g = d/(\lambda f)$ depends on the distance of the carbon edge from the central beam of the BFP (λ : electron wavelength, f : focal length of objective lens). k_x denotes the direction in the BFP perpendicular to the edge.

Fig. 6.5 shows experimental power spectra calculated from images of amorphous carbon film, recorded with a 300 kV TEM (Tecnai G_2 “Polara”, FEI company, Hillsboro, USA). Conventional image data recorded with strong underfocus ($\sim 20\mu\text{m}$) is compared to a HPC image data recorded with similar defocus. Fig. 6.5 A contains the typical pattern of concentric Thon rings, which correspond to maximal transfer of positive or negative phase contrast, as a thin carbon film can be considered as a phase object (cf fig. 3.5). In the HPC spectrum (fig. 6.5 B), the $\sin \rightarrow \cos$ transition of the pCTF can be directly observed: the Thon rings inside the gap (vertical stripe) follow a sine functionality, whereas outside the gap the Thon ring pattern is inverted. This indicates a 90° phase shift of the pCTF and thus a cosine-shaped phase contrast transfer for spatial frequencies affected by the phase plate.

The radial intensities of the power spectra are compared in fig. 6.5 C. The maxima of the HPC contrast transfer are reduced by $\sim 29\%$ compared to the data without phase plate. This is a consequence of the expected loss of coherent signal caused by interactions of the scattered electrons with the carbon film. Both images are zero loss energy-filtered, so that inelastically scattered electrons do not contribute to the background noise of the data. According to (6.2), a signal amplitude reduction of the pCTF to 71% corresponds to a carbon film transmissivity a_H of $\sim 42\%$. This value roughly agrees with the published results of other groups (Kaneko et al. 2005: 52% transmission at 300 kV). Danev and Nagayama (2008) measured a very similar pCTF amplitude (72%) for 64 nm thick carbon film, which implies that the phase plates used for this particular experiment were slightly thicker than the aspired 45 nm. A Zernike-type carbon film phase plate for 300 kV would require one half of the thickness that was used for the Hilbert phase plates. Consequently, the transmissivity is $\sqrt{0.42} = 0.65$. The corresponding amplitude of the Zernike pCTF has the same value of 65%.

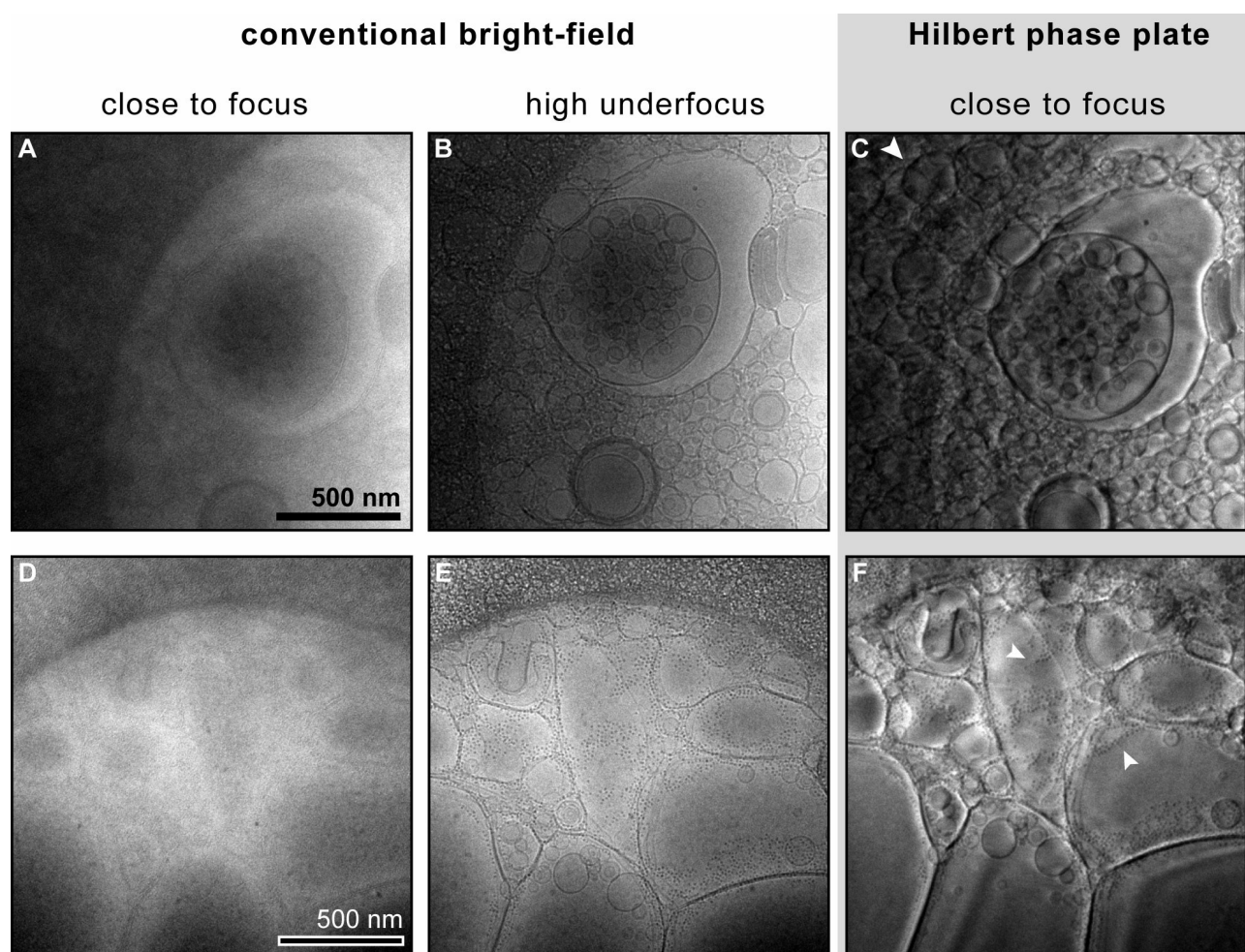


Figure 6.6.: Images of native, frozen-hydrated lipid vesicles mixed with ferritin molecules. The weak phase contrast of the close-to-focus images (A,D) is substantially enhanced by either strong underfocusing of approx. $25\ \mu\text{m}$ (B,E) or the insertion of a Hilbert carbon film phase plate while imaging close to Gaussian focus (C,F). The strong pseudo-topographic contrast of the HPC image yields a very good outline of structures located in denser areas of the field of view, as for the vesicles lying on top of the carbon support film (white arrow in C). This effect originates in the better transfer of low spatial frequencies, corresponding to the mass density projection of extended objects. Image F demonstrates the almost ideal contrast transfer for HPC, as it contains strong and sharp phase contrast for the huge vesicles with a few 100 nm in diameter as well as for the single ferritin molecules with a typical dimension of 5 nm (small arrows, see fig. 6.7). All images are taken at 34 kx primary magnification on a 300 kV FEI Technai G₂ “Polaris”, using a 4k x 4k pixel CCD (binned to 2k x 2k) and zero-loss energy filtering.

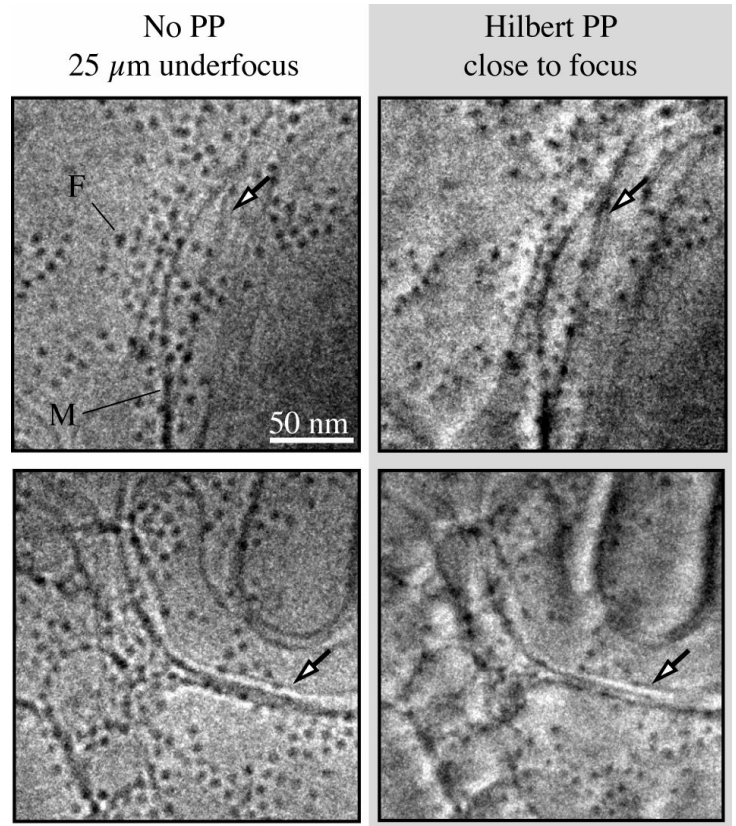
6.2.3 Hilbert phase contrast imaging of frozen hydrated specimens

If an image is acquired in Gaussian focus, the Hilbert PCTF simplifies to

$$pCTF_H^{Z=0}(k_x) = \begin{cases} 0 & k_x < g \\ -\frac{1+a_H}{2} i \operatorname{sign}(k_x) & k_x \geq g. \end{cases} \quad (6.3)$$

Fig. 6.6 shows a comparison of conventional defocus and in-focus HPC images of a typical biological cryo specimen. As expected from theory, the conventional, near-focus images (fig 6.6 A,D) of frozen-hydrated lipid vesicles decorated with ferritin (an iron-containing protein molecule) show particularly weak contrast. The outlines of the vesicles and individual ferritin molecules become visible by strong underfocusing of approx. 25 μm (fig 6.6 B,E). A substantial enhancement compared to the defocus phase contrast is achieved when the same object area is imaged in focus with a Hilbert phase plate inserted in the BFP (fig 6.6 C,F). The membranes of the rather extended vesicles, being 50-500 nm in diameter, appear with strong topographic contrast. This proves a good transfer of low spatial frequencies, which is a characteristic feature of the phase plate imaging technique (cf. fig 6.3). In comparison, the lowest spatial frequencies are under-pronounced in the defocus images (fig 6.6 B,E), which is a consequence of the sine-shaped contrast transfer. The superior contrast transfer of HPC for low spatial frequencies shows especially in the enhanced visibility of vesicles lying on top of the holey carbon support film, which cannot be recognised in the conventional defocus image (arrowhead in fig 6.6 C).

Figure 6.7.: Close-up from fig. 6.6. Frozen-hydrated lipid membranes (**M**) surrounding ferritin molecules (**F**) are imaged in conventional high underfocus ($Z \approx 25 \mu\text{m}$, left) and close to Gaussian focus with a Hilbert phase plate. The HPC image shows a better resolution of the membrane stacks, indicated by the arrows. Furthermore, due to the narrower PSF, the blurring of the ferritin molecules is reduced. Thus, the HPC image yields a more precise representation of the actual size of the molecules.



The difference in object representation between the defocus and the in-focus HPC technique also becomes apparent in fig. 6.7, where close-ups from fig. 6.6 (E and F) are shown. The images prove that beside the strong low-resolution contrast, the phase plate images also contain significant contrast for structural details. The individual ferritin particles mixed with the membrane vesicles represent high-resolution features, as their diameter of $\approx 5 \text{ nm}$ is in the order of the image pixel size of 0.57 nm . The molecules are clearly visible in both the conventional and the HPC image. The advantage of HPC lies in a sharper and clearer representation of double lipid membranes and membrane stacks (white arrowheads in fig. 6.7), which are not clearly resolved in the CTEM images due to the strong defocus blur of image points. This corresponds to the fact that the point spread (PSF) corresponding to the rapidly oscillating defocus CTF is significantly broader than Hilbert PSF. Producing sharper images and providing strong contrast at the same time is the main advantage of the novel HPC technique over conventional defocus CET.

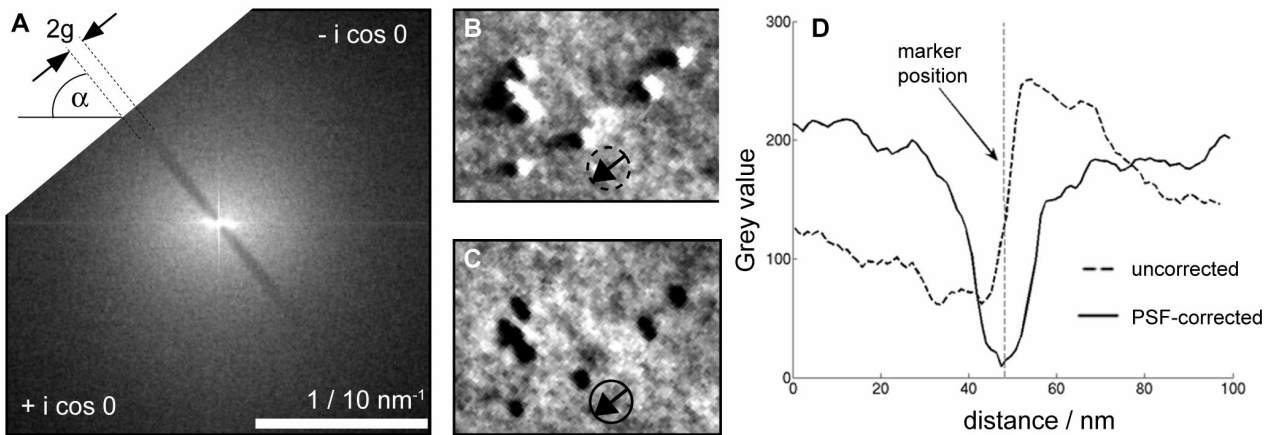


Figure 6.8.: Principle of the numerical Hilbert PSF correction. (A) The two deconvolution parameters, orientation α of the carbon edge and gap width $2g$, can be measured from the power spectrum of the HPC image. (B) 6 nm gold beads, used as markers for tomography, imaged with in-focus HPC. The antisymmetric object contrast (in direction of the arrow) can be clearly recognised. (C) The same image after PSF correction. The markers are now represented in isotropic positive phase contrast and the image can be used for tomogram calculation. (D) Grey values from B and C, measured along the direction of the arrows. The data clearly shows the transition from a spatially extended antisymmetric PSF (dotted curve) to a narrow isotropic point image (solid curve). (A-D) show experimental data recorded with a 200 kV TEM applying zero-loss energy filtering.

6.2.4 Numerical correction for the anti-symmetrical Hilbert contrast transfer

Caused by the $-\text{sign}(k_x)$ modulation of the pCTF, HPC images are convolved with an anti-symmetric PSF. This leads to a pseudo-topographic representation of density gradients within the object. This may sometimes be convenient for the human eye if images are analysed qualitatively (Kaneko et al. 2005, 2006; Setou et al. 2006). However, tilt images recorded for CET must be correlated as closely as possible to projections of the specimen mass density, as the 3D volume is reconstructed by a form of numerical back projection. Despite the strong contrast, this projection requirement of tomography is evidently not fulfilled for unprocessed Hilbert images (see e.g. fig. 6.6 C, E).

However, it is possible to convert HPC images into true projections by image processing. The anti-symmetric $\text{sign}(k_x)$ artefact can be eliminated numerically by multiplication with the inverse pCTF in Fourier space:

$$pCTF_H^{-1} = \begin{cases} 0 & k_x < g \\ i \text{sign}(k_x) & k_x \geq g. \end{cases} \quad (6.4)$$

The effect of this numerical correction (see also appendix D) can be seen in fig. 6.8. The close-up from the original in-focus HPC image, including gold beads used as markers for CET, shows the expected anti-symmetric Hilbert PSF. Numerical correction of the image with (6.4) yields isotropic contrast for the gold beads, and the resulting PSF is a sharp, isotropic dip. If a Hilbert image is recorded in Gaussian focus and then numerically PSF-corrected, it will represent a nearly perfect projection of the object's phase shifting potential. Since a PSF-corrected HPC image tilt series contains defocus artefact-free projections of the specimen's mass density with strong, isotropic contrast, it can be used for tomographic 3D reconstruction. A schematic workflow for HPC tomography, including numerical correction for the Hilbert PSF, is shown in fig. 7.1.

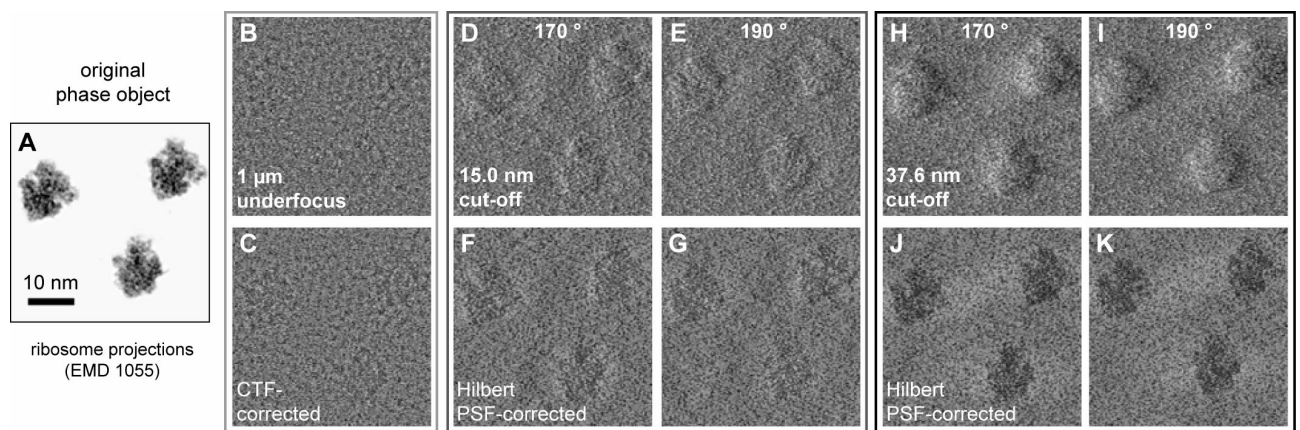
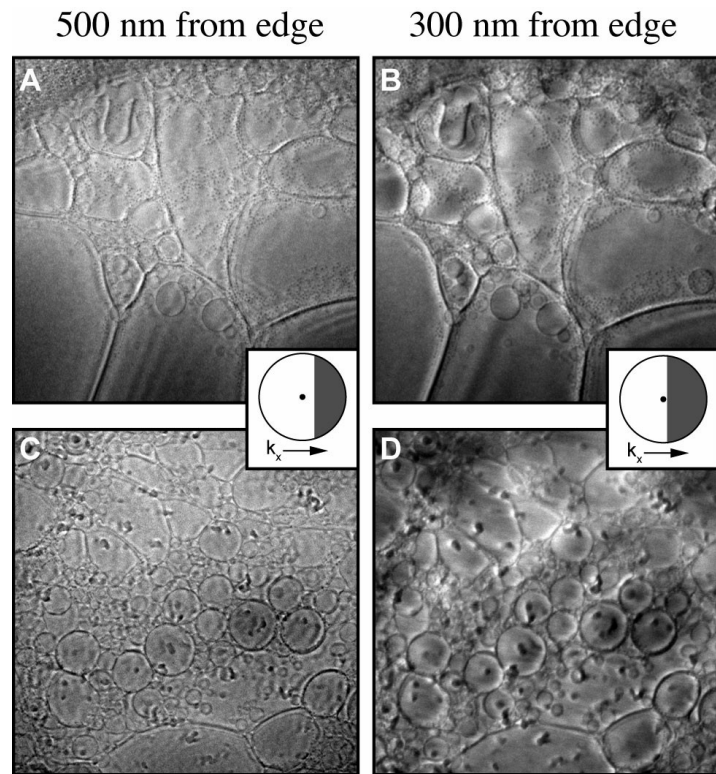


Figure 6.9.: Image simulations of ribosome complexes (EMD 1055), comparing conventional imaging with in-focus HPC with varying parameters. (A) Original model projections in vacuum. (B-K) Simulated images for a 200 kV TEM with $f = 3.0$ mm, assuming an ice-embedding generating 10% noise. (B) Bright-field image acquired with an underfocus of $1 \mu\text{m}$. (C) Same image as B, corrected for the CTF by numerical phase-flipping. (D-G) In-focus HPC images with an edge distance from the beam axis of 200 nm, corresponding to a cut-on frequency $g = 1/(15 \text{ nm})$ (see text). For phase shifts of 170° (D) and 190° (E), i.e. $\pm 6\%$ deviation from the ideal value of 180° , no significant difference can be observed. (F,G) Images D and E after numerical correction for the anti-symmetric Hilbert PSF using (6.4). (H-K) HPC simulations for an edge distance of 500 nm, resulting in a cut-on at $1/(38 \text{ nm})$. The contrast is significantly stronger than in D-G, due to the increased transfer of lowest spatial frequencies. (H,I) Again, a small deviation from the ideal 180° has a negligible impact on imaging. (J,K) After Hilbert PSF correction, both images yield a near-perfect representation of the projected object density A.

6.2.5 Effects of edge orientation, gap width and film thickness variations

There are three important parameters for the experimental implementation of the Hilbert carbon film phase plate:

Figure 6.10.: Effect of the Hilbert carbon edge position on HPC images of frozen-hydrated liposomes. (A,C) Edge in $\sim 500\text{nm}$ distance from focal spot, corresponding to a cut-on frequency (“high pass filter” in Fourier space) of $g = 1/(38\text{ nm})$. (B,D) Distance $\sim 200\text{-}300\text{nm}$, $g = 1/(15\text{-}23\text{ nm})$. As low spatial frequencies are transferred with stronger contrast, the visibility of extended vesicles is enhanced by positioning the phase plate edge closer to the focal spot. Images recorded on a 300 kV TEM with 41 kx primary magnification, using zero-loss energy filtering.



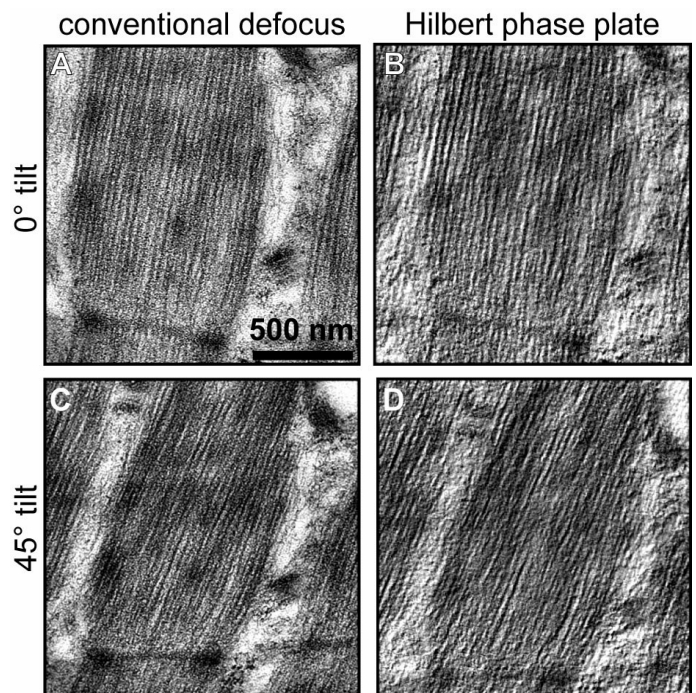
1. the azimuthal orientation of the carbon edge relative to the specimen
2. the distance of the edge from the central beam in the BFP (cf. figs. 6.5 and 6.8)
3. the film thickness, i.e., the amount of phase shift imposed on the scattered wave.

To understand better the influence of these parameters, HPC images of ribosomes were simulated as shown in fig. 6.9. Conventional defocus images show the expected weak phase contrast, so that the particles can hardly be distinguished from the background noise. Numerical CTF correction does not improve the situation (fig. 6.9 B,C). In comparison, the in-focus HPC simulations show a substantially enhanced SNR, and thereby an excellent visibility of the individual ribosome particles (fig. 6.9 D-K). It is evident that the edge position, i.e., the cut-on frequency g for the cosine-shaped contrast transfer, has the highest impact on the final, PSF-corrected HPC images (cf. fig. 6.9 F,G and J,K). To retrieve spatial frequencies as low as possible and thereby obtain the highest possible SNR, the carbon edge has to be positioned as close as possible to the focal spot of the BFP. However, a few 100 nm of edge distance is required in typical (non C_s -corrected) TEMs to prevent damage of the carbon foil by the intense zero beam, which has a FWHM of 300-600 nm. Fig. 6.10

shows that in practice, a distance as close as 200 nm can be realised without apparent damage of the phase plate. The experimental images of frozen-hydrated liposomes show the same increase of SNR with approximation of the carbon edge to the zero focal spot that results from the simulations.

In comparison to the impact of the gap width, the effect of a small deviation from the ideal thickness of the Hilbert phase plate has a negligible effect. The ribosome images simulated for 190° and 170° , respectively show the same amount of phase contrast (fig. 6.9 D,E and H,I), which does not change upon Hilbert PSF-correction (fig. 6.9 F,G and J,K). Likewise, the effect of the orientation of the carbon edge appears to be marginal. Theory predicts zero contrast in the image direction corresponding to the carbon edge. However, for the general visibility of the molecule outline, whose edges do not always coincide with the orthogonal direction of the carbon edge in the diffraction plane, such vanishing contrast in a singular direction is not relevant. In the PSF-corrected HPC images (fig. 6.9 F,G and J,K), the particular orientation of the phase plate can hardly be recognised.

Figure 6.11.: Images from tilt series of mouse skeletal muscle thin sections (thickness about 120 nm, primary magnification 16.6 kx). Part of a sarcomere with z disc and thick myosin filaments is shown. (A and C) Images without phase plate acquired with strong underfocus ($\approx 10 \mu\text{m}$, CTF-corrected by phase flipping) at 0° and 45° specimen tilt, respectively. (B and D) Images recorded in Gaussian focus with a Hilbert phase plate after subsequent numerical PSF correction (see fig. 6.8). Note the improved contrast of individual thick filaments. The corrected Hilbert images represent a faithful projection of the filament structure, as it contains the entire range of resolvable structure factors. Both image series were zero-loss energy filtered.



6.3 Hilbert phase contrast tomography of embedded sections

To test the experimental applicability and performance of Hilbert phase contrast ET, tomograms were recorded at high underfocus without a phase plate (conventional technique) as well as in focus

with a Hilbert phase plate, using the same object. The results obtained from both techniques were compared. As test specimens, lightly contrasted sections of resin-embedded skeletal muscle from mice and unstained, uncontrasted sections of resin-embedded *P. pastoris* (yeast) cells were chosen.

6.3.1 Material and methods

The mouse muscle tissue was fixed with 2.5 % glutaraldehyde (GA) and 0.1 M Na-cacodylat buffer, embedded in low viscosity resin (Agar), microtome-sectioned (~ 100 nm thick) and subsequently exposed to osmic acid vapour. The yeast cells were fixed with 4 % paraformaldehyde, 1 % GA and 0.1 M Na-cacodylat buffer and then embedded in LR White Resin (London Resin Company). The cells were microtome sectioned without any additional staining. Unstained yeast cell sections were chosen to test the new technique on a sample that generates particularly weak phase contrast for conventional ET. The low contrast is owing to the similar mass densities (refractive indices) of the organic material and the embedding medium (resin). However, it should be noted that such samples show a considerable amount of amplitude contrast in the zero-loss energy-filtered imaging mode, which is now routinely used for ET (fig. 6.2). The sections were mounted on a standard electron microscopy grid coated with a thin carbon support film. All other acquisition parameters such as magnification, specimen position and tilt scheme, as well as acquisition times and total electron dose, were the same for both HPC and conventional tomograms.

The tomogram tilt series were recorded using a 200 kV FEG TEM with a corrected in-column 90° energy filter (SESAM II, Carl Zeiss NTS, Oberkochen, Germany). Images were zero-loss energy filtered and recorded with a 1k x 1k pixel slow scan CCD camera (Gatan Inc., Pleasanton, USA). Primary magnifications were 8.500 x and 16.500 x. For acquisition of the HPC in-focus tomograms, a Hilbert phase plate as described in section 6.2.1 was inserted into the back focal plane of the objective lens. The necessary accurate positioning in all spatial directions was achieved by a piezo-driven nanometer (Kleindiek, Germany) as described in section 3.1.2. Fine adjustment of the BFP to coincide exactly with the carbon film was obtained electron-optically by minor changes of the condenser lens excitations. To minimise contamination and charging, a cryo shield surrounding the phase plate was kept at liquid nitrogen temperature. Image focus and lateral position of the carbon edge was checked by inspection of the power spectrum and adjusted (if necessary) after each set of ~10 images. This was sufficient to maintain close-to-optimum Hilbert contrast for the entire tilt series of 60-100 images.

Otherwise, the phase plate contrast was not affected by specimen tilting or electron beam exposure. Linear tilt schemes, i.e. constant tilt angle increments, were used in all the experiments. For the mouse muscle sections, an increment of 1.5° with a maximum tilt angle of $\pm 45^\circ$ was used. For the yeast cell sections, the tilt range was $\pm 60^\circ$ with an increment of 2° . Gold markers were added to the sections for subsequent tilt series alignment.

Images from the conventional defocus phase contrast tilt series were corrected for the CTF. The corresponding defocus of the individual images were determined from periodograms and the phases of structure factors flipped accordingly. Considering the sample area and the achievable resolution, it was sufficient to measure one average underfocus value for each image of the tilt series. The correction for the Hilbert PSF was performed as described in section 6.2.4, using dedicated image processing modules compiled under the program package Mat Lab (The Math Works, USA; see app. D). The rotation of the Hilbert edge was determined once for each image series using the zero tilt image and the Hilbert gap width was measured automatically for each individual image to account for lateral drift of the phase plate during acquisition. After Hilbert PSF correction of each individual image, tomograms were generated using the IMOD package (Boulder Laboratories, USA) using marker points for image alignment. The resulting volumes were slightly de-noised using non-linear anisotropic diffusion (Frangakis and Hegerl, 2001), applying the same parameters to conventional and Hilbert contrast volumes.

6.3.2 *Reconstructions of mouse muscle sections*

The images from the muscle tilt series and the resulting tomogram are shown in figures 6.11 and 6.12. The images taken with Hilbert phase plate reveal a stronger overall contrast, and the myosin filaments within the muscle fibre can be more clearly recognised. This enhanced contrast of the individual myosin filaments is seen even more clearly in the reconstructed volume shown in fig. 6.12 B and E. In the reconstruction calculated from underfocus images, the filaments have a granular appearance, an artefact of the convolution of the object density with the extended, ring-shaped underfocus PSF. The filaments break apart into artificial fragments, as can be seen in the surface-rendered isosurface representations (fig. 6.12 C). Individual filaments can hardly be tracked throughout the volume or counted. On the other hand, the Hilbert reconstruction contains continuous filaments that are well separated from each other (fig. 6.12 F). This continuous appearance underlines the presence of structure factors for low spatial frequencies that are lost in defocus images. At the same time, the over-emphasised granularity owing to CTF oscillations at higher spatial frequencies is strongly reduced. From the close-up of the 3D isosurface visualisation in fig. 6.12 C and F, it is obvious that the HPC reconstruction is a better and less noisy representation of the myosin filaments.

6.3.3 *Unstained yeast cell sections as a test for Hilbert CET*

To investigate the improvement of the SNR by the Hilbert phase plate for specimens with a very low intrinsic contrast, tilt series of thin unstained sections of yeast cells embedded in resin were recorded. As a consequence of the low difference in densities of the embedding polymer and the biological components, intracellular features remain almost invisible when imaged in Gaussian focus (cf. fig. 6.2 A,E). Features such as cell organelles or the cell wall can be visualised only with strong underfocus or by use of the Hilbert phase plate (cf. fig 5B,C).

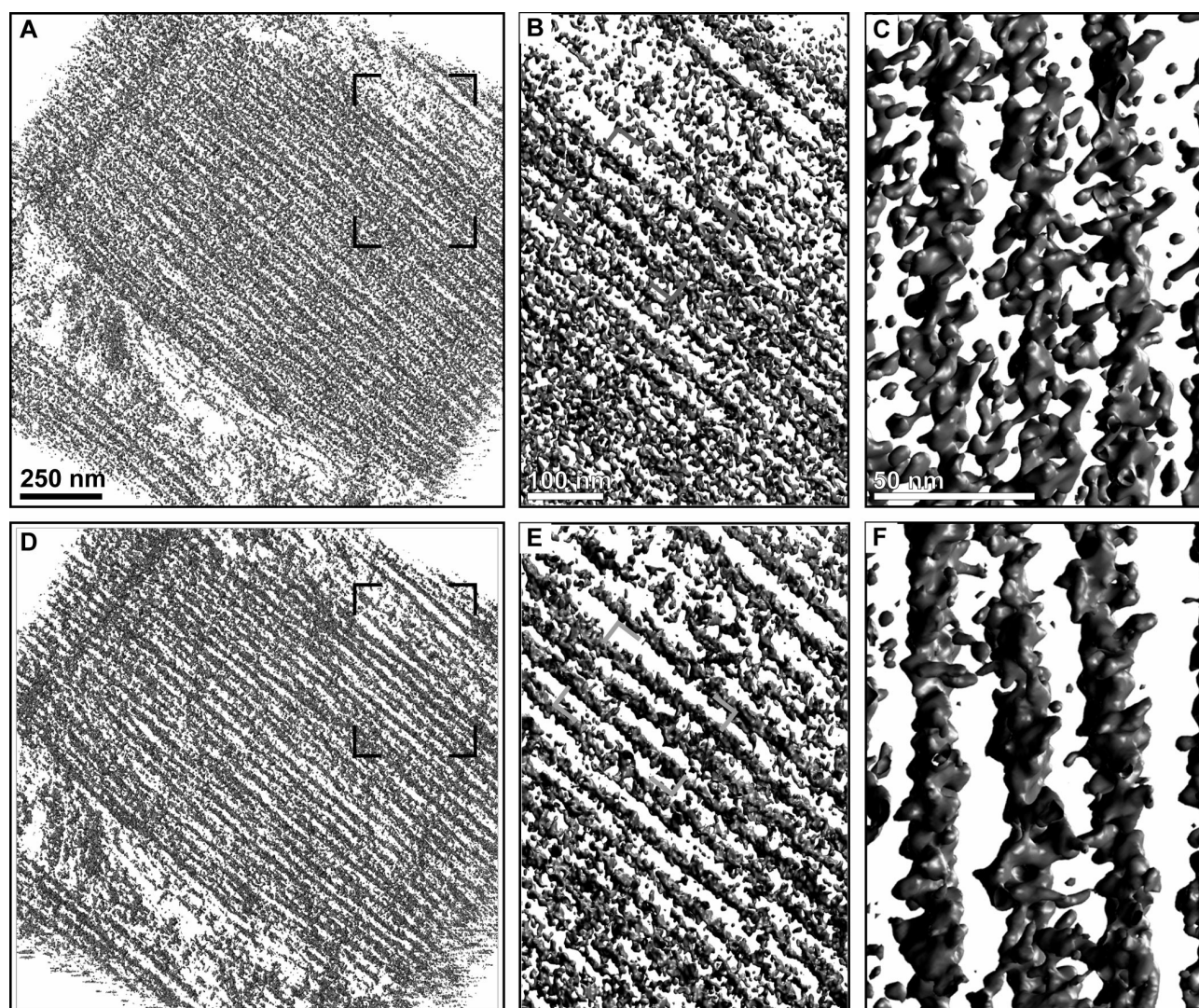


Figure 6.12.: Tomogram of a thin section of resin-embedded mouse skeletal muscle (cf. fig. 6.11). The figures show isosurfaces of the raw volume data, enclosing the same mass for the conventional CTF-corrected underfocus (top row) and HPC-generated volumes (bottom row). (A and D) The entire volume ($1.5 \times 1.5 \times 0.12 \mu\text{m}$) shows part of a sarcomere. (B and E) Close-up of the areas framed in A and D showing myosin filaments viewed along the electron beam direction. The Hilbert reconstruction (E) is significantly less noisy than the conventional volume (B) and allows for a clear separation of the individual filaments. (C and F) Close-up of three myosin filaments. The individual filaments appear discontinuous and granular in the the conventional reconstruction (C), as a result of the low SNR of the defocus phase contrast images. In the sub-volume from the Hilbert reconstruction (F), the filaments are well separated and continuous. The volumes were slightly denoised by linear anisotropic diffusion (Frangakis and Hegerl, 2001), using the same parameters for HPC and underfocus data. The isosurfaces are entirely computer-generated, so that no manual segmentation was involved.

During acquisition of the conventional tilt series, a strong underfocus of about 15-20 μm was applied to generate sufficient contrast for the most prominent object features (fig. 6.13 A, C). On the other hand, when imaging with the Hilbert phase plate the cells and their internal features were clearly visible in focus (fig. 6.13 B, D). Figure 6.14 shows sections through the reconstructed volumes, comparing the resulting object visibility of both techniques. In the conventional reconstruction, the material appears granular, with a very faint contrast for mitochondrial membranes and the cell wall (fig. 6.14 C, E). In comparison, the Hilbert phase contrast reconstruction yields a much clearer outline of the cellular features (fig. 6.14 D, F). The mitochondrial membranes appear with strong contrast in the HPC volume, together with features that were invisible in the conventional reconstruction. Despite the low magnification of 8.500 x, intracellular protein complexes close to the mitochondrion surface, most likely ribosomes, can be distinguished unambiguously (fig. 6.14 F).

*Figure 6.13.: Typical images of unstained, uncontrasted thin sections of resin-embedded *P. pastoris* cell sections (cf. fig. 6.2) as recorded during tilt-series acquisition (primary magnification 8.5 kx). (A and C) Conventional high defocus images (about 20 μm underfocus). (B and D) Corresponding in-focus HPC images of the same specimen area. Insets: power spectra.*

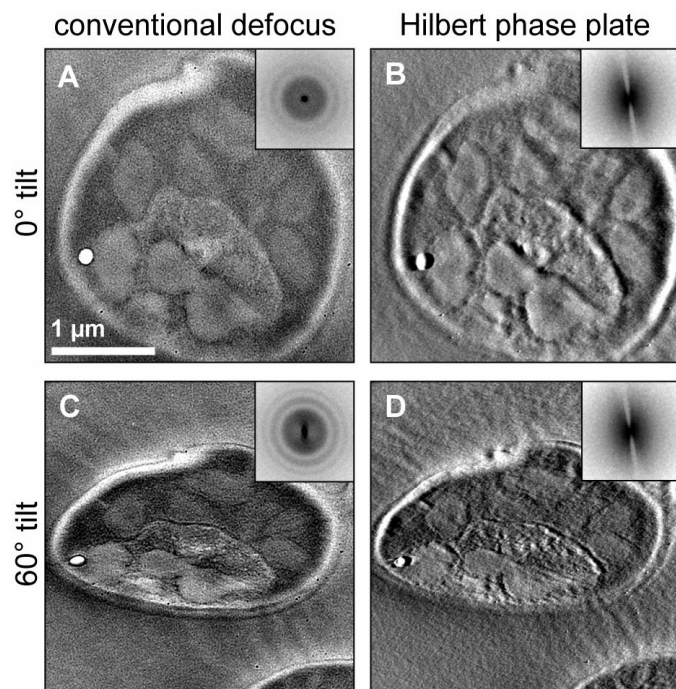
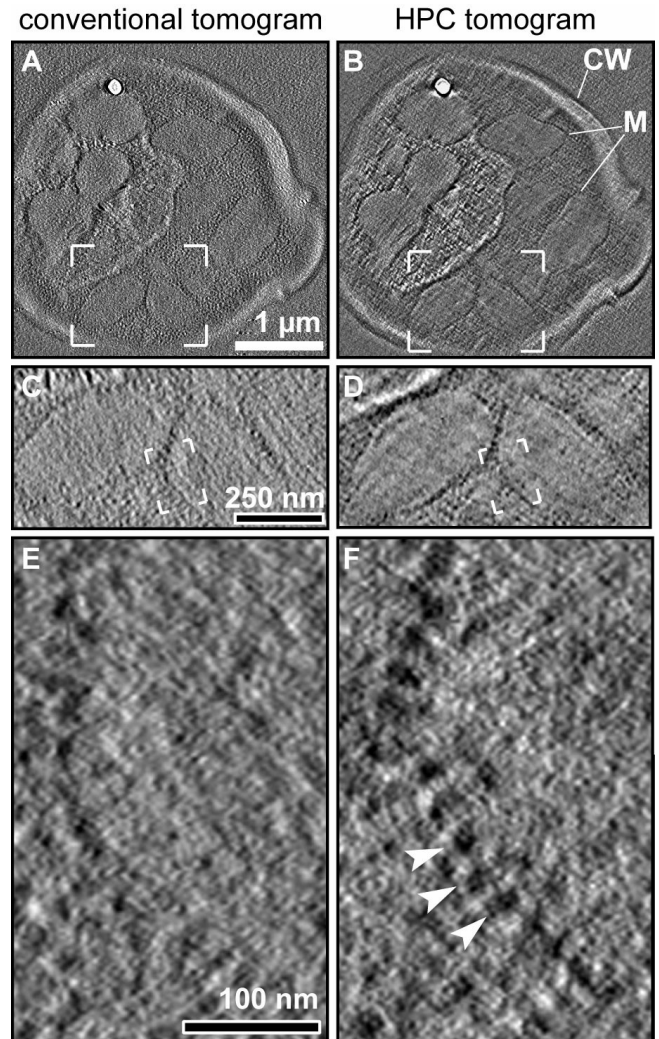


Figure 6.14.: Slices through the tomogram of a section of a resin-embedded, unstained *Pichia* cell. Viewing direction along the initial electron beam direction. (A,C,E) Volume derived from conventional defocus images (tomographic reconstruction after CTF-phase correction, see text). (B,D,F) The same slices through the corresponding Hilbert tomogram (cf. fig. 6.13). (C and D) Boxed area in A and B. The structures are likely to be two neighbouring mitochondria. (E and F) Close-up of mitochondrial membrane framed in C and D. While macromolecular densities can hardly be recognised in the conventional reconstruction (E), they can be clearly seen as individual objects in the HPC volume (arrowheads in F). This clearly indicates an improved SNR in HPC tomography, as compared to defocus phase contrast. The mean spacing between the objects indicated is 30.1 nm, their diameter approx. 12 nm. The cut-on frequency for the HPC tilt series was in the order of $1/(80 \text{ nm})$.



6.4 Discussion & Conclusion

The first experimental HPC tomograms of weak-phase objects demonstrate the superior imaging conditions of in-focus phase contrast. The overall improvement in object contrast and signal has been demonstrated before for Zernike-type carbon phase plates in general (Danev and Nagayama 2001b), and more recently also in a quantitative study (Danev and Nagayama 2008). Hilbert-type phase contrast has so far only been used in a qualitative way (Setou et al. 2006). The experiments documented in this thesis shows for the first time the quantitative PSF correction and the application of the HPC technique in tomography.

An important result of the experiments is the surprising ease of use of the carbon Hilbert phase plate even for the acquisition of time-consuming tilt image series. While Zernike-type carbon phase

plates are hampered by difficult alignment and contamination (Majorovits 2002), the simple carbon edge of the Hilbert phase plate can easily be aligned and replaced simply by moving along the edge. A large number of physical phase plates can be loaded in the microscope column at the same time by using the set-up shown in figure 6.4. To exploit these practical advantages, no specially manufactured indentation was used for the unscattered central beam in the diffraction plane, which would compare to the central hole of a typical carbon film Zernike-type phase plate. Such an indentation would allow us to position the carbon edge exactly to intercept the origin of the diffraction plane. Instead, a smaller contribution of phase contrast was accepted for structure factors in the direction of the carbon edge, which is the result of the dislocation gap of the phase plate in the diffraction plane (cf. fig. 6.5 B and 6.10). The simulations and the experimental results illustrate that the limited loss of contrast in one direction does not impede the visibility of biological objects, or their quantitative reconstruction in a tomogram after correction for the specific Hilbert PSF.

The imaging theory for thick samples is less straight-forward than for ideal weak-phase objects, as different kinds of scattering processes contribute to the contrast. The theoretical considerations and simulations described in section 2.1.5 imply that the application of a phase plate improves object contrast and SNR also for thick samples. As demonstrated in fig. 6.2, this assumption is indeed justified for the mixed amplitude and phase contrast observed for thick objects if images are zero-loss energy-filtered. This agrees with the results of other published studies (Han et al. 1995).

The two biological samples used in this study for illustrating the use of in-focus Hilbert phase contrast demonstrate a major visual improvement of SNR in the analysed tomograms. However, a quantitative assessment of the level of improvement is difficult. In a recent study for single particle analysis (Danev and Nagayama 2008), the answer to the question of contrast enhancement was not very clear: resolution did not improve by using a phase plate, but the number of particles needed to obtain a given resolution decreased as result of the improved visibility. The situation for the experiments presented here seems to be similar: the processing of the myosin thick filament array did not show any additional features in the periodicities of the filaments. However, a simple thresholding of the volume as a first step to segmentation shows a clearer representation of the outline and organisation of the filaments within the muscle fibre (fig. 6.12). Similarly, internal structures in whole cells (fig. 6.14) are visible in the HPC tomograms, whereas even after CTF correction they are not recognisable in defocus phase contrast tomograms.

The trial tomograms show that the application of a Hilbert phase plate in electron tomo-

graphy can enhance the signal-to-noise ratio of the 3D reconstruction significantly, while the applied electron dose and all other acquisition parameters are unchanged. As a result of the contrast enhancing phase shift by a physical phase plate, the microscope can be operated in focus while recording high contrast images of weak-phase objects. Charging or contamination of the carbon film was not a problem, nor was the positioning of the phase plate in the BFP very critical for tilt series acquisition. After a straight-forward, automatic procedure correcting for the anti-symmetric PSF, Hilbert phase contrast yields tomograms with high signal for features such as the outline of large structures or macromolecular complexes. As examples, the improved contrast for mitochondria is demonstrated as well as for structural details such as myosin filaments in muscle fibres. In Hilbert ET, the object information encoded in the object exit wave is almost ideally retrieved, and contrast generation does not compromise resolution - as is the case with the conventional highly defocused images. Given the limitation of electron dose with radiation-sensitive specimens, the Hilbert phase plate has the potential to enhance the SNR of embedded objects and to generate tomograms with lateral resolutions of 2-3 nm. It is worth noticing that the integration of a Hilbert phase plate does not compromise the use of other electron optical components, such as energy filters or aberration correctors and does not require additional expensive hardware.

7 Discussion & Outlook

The problem of low contrast of phase objects represents a considerable limitation of TEM, in particular for native frozen-hydrated biological specimens. For typical samples, the object information is encoded in a small distortion of the plane wave front incident to the specimen, which must be converted into image contrast (phase contrast) for structural analysis.

The conventional method of generating phase contrast, deliberate out-of-focus imaging of the specimen, is highly unsatisfactory because it generates image artefacts. The sine-shaped defocus contrast transfer is particularly weak for low object frequencies, and thus strong defocusing is required to visualise features on the scale of several nanometers. On the other hand, this causes rapid oscillations of the transfer function (CTF) and contrast reversals, so that even after numerical CTF correction only certain bands of spatial frequencies can be recovered. Thereby, the attainable resolution is compromised for many applications or focal series are required, thus increasing electron dose and radiation damage experienced by the specimen.

Han et al. (1995) showed that the problem of weak phase contrast persists for thick specimens (0.3–1 μm), such as ice-embedded cells or organelles as they are analysed in CET. Although objects with a thickness above 0.5 μm cause about 60% inelastic scattering which can be converted into amplitude contrast by energy filtering (Schröder 1992; Angert et al. 2000), this component contributes only at resolutions well below 25 nm. The exit wave reconstruction for thick specimens showed significant phase contrast, and this contribution dominates for resolutions >10 nm (Han et al. 1995). These findings agree well with the simulations and experiments documented in section 6.1 where amplitude contrast is eliminated by high-pass filtering, while in phase contrast images, the specimen features remain visible. The trial in-focus tomograms using a Hilbert phase plate recorded for this work demonstrate that strong in-focus phase contrast substantially enhances the SNR of the obtained 3D reconstructions, compared to the conventional defocus technique. This proves that also for tomography and CET of thick biological specimens, the retrieval of phase contrast is essential.

7.1 Current approaches to the weak phase contrast problem

Many approaches exist in TEM to solve the problem of weak and artifactual contrast transfer for phase objects. In many materials science applications, the exit wave phase is reconstructed by

through-focus series, recording 20 or more images of the same specimen with varying defocus (Coene et al. 1996). This method is certainly not applicable for native biological samples, as it requires an unacceptably high dose. Lentzen and co-workers established an imaging mode for high resolution imaging of materials, producing an extended spectral band of maximum phase contrast using a C_s -tuner (Lentzen 2004). However, this contrast is not effective for object periodicities lower than 0.5 nm, and therefore the technique is not appropriate for biological and many other materials science applications.

An almost ideal object phase reconstruction can be obtained by off-axis electron holography (Gabor 1948). This method principally provides high resolution information (<1nm), and the resulting phase image fulfils the projection requirement of tomography. Three-dimensional reconstructions of the electric potential inside silicon p-n junctions were recently obtained by tomographic electron holography (Twitchett et al. 2005), and electron holography was also applied to biological specimens (Simon et al. 2003, 2004). Nevertheless, the method is afflicted with some problems when used for analysis of radiation-sensitive samples, e.g. frozen-hydrated specimens. First, the refractive indices of biological material and embedding ice are very similar (Majorovits 2002), and thus even for a thick specimen the phase variation of the specimen exit wave is in the order of a few degrees. This is also shown by the simulations in section 2.1.5 of this thesis. This makes the reconstruction difficult in the presence of a usually high noise level of the data. Second, holography requires a hole for the reference beam to be burnt into the ice close to the area of interest, which can lead to specimen damage. Third, the field of view in electron holography is generally restricted, which may be a drawback for cellular tomography where the area of interest can be 2-5 μm in dimension.

7.2 In-focus Hilbert phase contrast enhances electron tomography

To exploit the excellent native preservation of biological specimens obtained by frozen-hydrated preparation, a technique for maximal in-focus phase contrast retrieval has to be developed for TEM (“in-line holography”). The superior contrast transfer by a physical phase plate in images of cryo specimens is demonstrated in section 6.2.3, as well as by other groups (Danev and Nagayama 2004).

The technically less demanding implementation of in-focus contrast by thin-film phase plates, as first realised by the Nagayama group (Nagayama 2002), can be an appropriate solution for obtaining optimal contrast at medium resolution. The first application of a carbon film phase plate in

electron tomography, presented in this thesis, brought two important results: First, initial problems with alignment and contamination of the the phase plate during acquisition of tilt series (Marko et al. 2005) were solved by the choice of the Hilbert geometry. The translational symmetry of the phase plate (see. fig. 6.4) allows for quick replacement and easy positioning. Second, in-focus Hilbert phase contrast (HPC) leads to better visibility of tomogram features, and generally to a more faithful representation of the 3D object reconstruction (figs. 6.12 and 6.14). The amount of coherent elastic signal loss by interactions of the electron beam with the phase plate was determined to be $\sim 29\%$ ¹³, which is in good agreement with the results from other groups (Kaneko et al. 2005; Danev and Nagayama 2008). However, this was not a drawback for the application of the Hilbert phase plate for electron tomography, and the amplitude loss was more than compensated by the improvement of signal by the optimised contrast transfer. In the future, it needs to be shown that HPC can also be used for cryo samples, i.e. CET. From the current experience, it is expected that only when using vitrified samples and state-of-the-art equipment, it will indeed be possible to achieve the anticipated higher resolution by Hilbert phase contrast tomography. There were some difficulties encountered for CET under low-dose conditions preventing the comparison of HPC tomography of frozen-hydrated samples with the conventional technique within the timeframe of this work. One of the difficulties was that the automated tilt series routine featured in the utilised commercial TEM did not provide the required axial beam alignment stability. This made positioning of the phase plate during tomogram acquisition difficult. However, finding an appropriate optical alignment with two defined points (rotation centre of image & focal spot in the BFP) and making the necessary minor modifications to the software should be straight forward in the future (cf. fig. 7.1).

Another interesting result from the experiments made during this project was that thickness variations of the carbon film appear to be largely uncritical. As the inner potential of the material, 10.7 V (Wanner et al. 2006) was assumed, which results in a film thickness of 45 nm to realise a Hilbert phase plate for a 300 kV TEM. Meanwhile, the Nagayama group assumed a potential of only ~ 7.5 V, which requires a thicker phase plate of 64 nm (Kaneko et al. 2005). In both cases the results were similar, and the desired $\sin \rightarrow \cos$ transition of the pCTF was achieved. The high thickness tolerance is one hand owed to the small variation of the cosine pCTF close to zero, which is implied by the image simulations of ice-embedded protein in section 6.2.5. On the other hand, the applied carbon film can principally have different properties, such as surface contributions to the phase

¹³ at 300 kV and 45 nm film thickness

shift, which were not considered in the theoretical calculations. While Nagayama and coworkers successfully avoided insulating contamination of the carbon film by heating of the Zernike phase plates (Danev and Nagayama 2008), the problem was solved for this work by loading a large number of Hilbert phase plates in the TEM at the same time. The large number was achieved by using a long carbon edge spanning a 3 mm grid¹⁴. When contamination occurred, the carbon film was simply shifted by a few micrometers along the edge to obtain a clean phase plate. This procedure can be repeated 50-100 times, without the need to exchange the phase plate holder.

7.3 First realisation and proof-of-principle for a Boersch electrostatic phase plate

A recent study revealed that while in-focus Zernike phase plate imaging dramatically improves the contrast of low spatial frequencies, the high resolution signal is attenuated by coherence loss in the carbon film (Danev and Nagayama 2008). Thus, thin-film phase plates do not yield an improvement in resolution of molecular single particle reconstruction, with respect to conventional defocus imaging. In view of these findings, the electrostatic phase plate, first described by Boersch in 1947, is the ideal implementation of in-focus phase contrast for TEM. The Boersch phase plate shifts the relative phase of scattered and unscattered wave by means of an electrostatic field and thereby avoids electron-matter interaction and coherence loss, as it occurs with thin-film phase plates (Boersch 1947).

Sixty years after its invention, it has now become possible to produce a micro-structured einzel lens and to use it as an electrostatic phase plate. This work presents the first implementation and proof-of-principle for Boersch's electrostatic phase plate (Majorovits, Barton et al. 2007). The experiments documented in section 3.1.2 prove that the unscattered electron beam is uniformly phase shifted by the electrostatic potential of the lens electrode positioned in the centre of the BFP, as it was already shown numerically (Matsumoto and Tonomura 1996). An additional relative phase shift between scattered and unscattered electron wave can be adjusted. Thus, for the appropriate phase shift of $\pi/2$, a conversion of the sine pCTF into a cosine function is achieved (fig. 3.4). The use of a non-centro-symmetrical geometry of the einzel lens support allows for single-sideband signal transfer of object information that is potentially obstructed by the supporting rods (fig. 3.9). Apart from an attenuation of the signal transfer envelope by a factor of $1/2$, this information can be restored by

¹⁴ together with maintaining a good, oil-free vacuum in the range of $5 \cdot 10^{-7}$ mbar inside the specimen chamber.

dedicated image processing.

The fabrication of round electrostatic phase plates was reported in parallel by three other groups, whose technical implementations are compared in table 4. Cambie et al. realised a phase plate by a cylindrically-shaped drift tube with a high aspect ratio (height:diameter $\sim 5:1$). The design may have the advantage of being more mechanically robust than the delicate einzel lenses consisting of layer with a thickness of a few 100 nm each. Moreover, due to the high aspect ratio of the device, a bias voltage of 14 mV is sufficient to obtain a 90° phase shift for 100 kV, which is small in comparison to the ~ 400 mV required in the case of the einzel lens design described in this thesis (fig. 3.5). A smaller voltage may reduce the risk of electrical short-circuits that can destroy the phase plate. A third group, also from Lawrence Berkeley Laboratory, presented a design very similar to the Boersch einzel lens designed for this work, using also a threefold symmetry with slightly smaller dimensions (Hsieh et al. 2007). However, the full phase shift of 90° could not be shown, and comparatively high electrode voltages were needed.

	Berkeley drift tube	Berkeley einzel lens	Tsinghua university	MPI of Biophysics
reference	Cambie et al. 2007	Hsieh et al. 2007	Huang et al. 2006	Majorovits, Barton et al. 2007 Schultheiß et al. 2006
design principle	drift tube	einzel lens	einzel lens	einzel lens
symmetry	onefold	threefold	twofold	threefold
inner electrode radius [μm]	1.0	0.3	2.5	0.5
outer electrode radius [μm]	2.0	1.0	5.0	1.3
low frequency cut-on (200 kV, $f = 3.0$ mm) [nm]	3.4	6.8	1.4	5.2
full 90° phase shift of CTF shown	yes	no	questionable	yes
bias voltage for 90° phase shift [mV]	14 (100 kV)	$> 1,000$ (200 kV)	$> 2,000 ?$ (200 kV)	400 (200 kV)

Table 4: Comparison of the first published implementations of an electrostatic phase plate

7.4 The PACEM project: exploiting ideal phase contrast for biology and CET

The recently achieved technical implementations of electrostatic phase plates represent a promising advancement in electron optics. However, all implementations share a common problem: the obstruction of the central part of the diffraction pattern by the lens or drift tube electrode. Even with the smallest designs, the transfer of all spatial frequencies lower than $1/(5.2 \text{ nm})$ is blocked, as shown in fig. 3.10. For some applications such as electron crystallography, where contrast at low resolutions is less important, the obstruction of low spatial frequencies may be tolerable. This is not the case for most biological TEM techniques, particularly for CET where acquiring low resolution data is important.

The ongoing development of a specialised phase contrast TEM, where the Boersch electrostatic phase plate is combined with a lens system to create a magnified back focal plane together with a spherical aberration corrector, opens new vistas for TEM analysis in biology and materials science. The simulations in section 4.3 show that by with increasing the effective focal length of the objective lens, the low frequency cut-on will be reduced proportionally. For an electrode diameter of $2.6 \mu\text{m}$, a magnification of the diffraction pattern by a factor of 5 will alter the lowest transferred resolution from 5.2 nm to 26 nm ¹⁵. This would allow high-resolution imaging e.g. of large protein complexes with optimal in-focus phase contrast. The PACEM¹⁶ project aims to exploit the full performance of a state-of-the-art TEM for reconstruction of native biological samples.

7.5 A concept for obstruction-free electrostatic phase plates

Another approach for the development of obstruction-free electrostatic phase plates is the concept of the anamorphic phase plate, outlined in chapter 5. With the development of chromatic aberration correctors (Rose 2004; Haider and Müller 2004), the realisation of a dedicated quadrupole optics, generating two perpendicular anamorphic diffraction planes with a high aspect ratio, is now within reach of technology. Although the concept has a comparatively high technical demand, the simulations in section 5.3 of this thesis show that the anamorphic phase plate yields artefact-free, high contrast images of ice-embedded protein complexes. Within a collaboration, a first prototype of such a phase plate was implemented (fig. 5.2).

¹⁵ for a 200 kV TEM with $f = 3.0 \text{ mm}$

¹⁶ phase contrast aberration corrected electron microscope

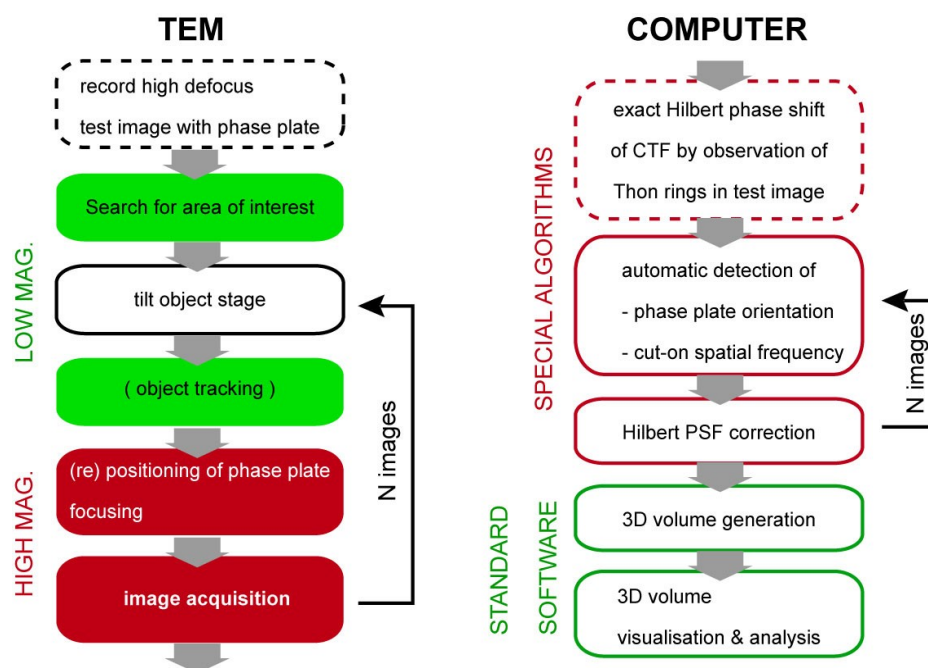


Figure 7.1.: Schematic workflow for 3D reconstruction by Hilbert phase plate CET.

Another nearly obstruction-free phase plate concept, based on the magnetic Aharonov-Bohm (AB) effect, was recently described by Nagayama and co-workers (Yasuta et al 2006). It consists of a thin (800 nm) bar magnet deposited on a biprism wire spanning the objective aperture. By creating an appropriate magnetic flux around one half of the diffraction pattern, Hilbert-type phase contrast can be achieved. However, so far the proof-of-concept is lacking.

The experiments with Hilbert phase plates described in chapter 6 show that the half-plane geometry has practical advantages, as the simple geometry also simplifies the necessary devices. As Nagayama's AB phase plate, an anamorphic phase plate operated in Hilbert mode would require less technical complexity than its Zernike equivalent (fig. 5.4). The experiments with Hilbert-type phase plates carried out during this project prove that the pseudo-topographical contrast artefact produced by this particular type of phase plate can be removed reliably by image processing. This results in a faithful, artefact-free projection image (section 6.2.4). The contrast transfer of the Hilbert phase plate is, after PSF correction, equivalent to that of a Zernike phase plate.

7.6 The future of in-focus TEM

The fact that conventional defocus imaging techniques for phase objects in TEM are deficient and

utilise only a part of the attainable object information is often neglected. Information about the exit wave phase, and thereby the structure of the analysed phase object, is not transferred at all or with substantial artefacts if phase contrast is generated by defocusing. In comparison to other instrumental parameters such as energy filtering, image detection, the electron source or even aberration correction, the issue of low phase contrast is often underestimated for TEM of native biological specimens. There is considerable danger of interpretation of artefacts arising from the incomplete transfer of structure factors, especially when dealing with the reconstruction of structurally unknown, amorphous and pleomorphic systems, as is typically the case in biological CET and single particle methods. In materials science, a similar drawback exists for the analysis of phase objects, e.g. polymers consisting of light organic elements, or magnetic or electrostatic fields inside the probe, which are phase objects par excellence.

The development of in-focus imaging techniques for TEM in biological and materials science is promising because of two reasons: it removes uncertainties in data interpretation that may be caused by defocus artefacts, and at the same time it exploits the full performance of the instrument for the analysis of phase objects (Henderson 1995). In biological cryo TEM and CET, in-focus imaging reduces the impairments that result from the dose limitation by enhancing the signal and making defocus series acquisition unnecessary. The new technique can help to build the bridge in structural biology between in vivo light microscopy and molecular structure determination by X-ray crystallography (Sartori et al. 2007). Enhancing the SNR, and thereby the structural resolution of 3D reconstructions of molecular complexes, will routinely permit hybrid approaches, such as flexed fitting of molecular structures into densities obtained from single particle TEM and 2D electron crystallography (Schröder 2004; Robinson et al. 2007). Molecular recognition in tomograms of complex close-to-native biological systems is expected to be feasible if isotropic resolutions of 2-3 nm can be routinely achieved. In this way, it may become possible to draw protein maps of cellular systems and to yield snapshots of the highly complex machinery in live cells, e.g. in neuronal synapses.

Although the use of phase plates is expected to optimise the signal transfer, the problem of high noise owing to limited electron dose, inelastic scattering and imperfect sampling of electrons by the detector will persist. Ultimately, the analysis of biological structures by TEM will never be better than permitted by the instrument's weakest component. Therefore, dedicated instruments have to be designed that fulfil all requirements of cryo TEM and especially cryo CET in an optimal way.

Apart from establishing phase plate TEM, developments concerned with improving other aspects of TEM imaging are ongoing. These include monochromators and filters (van Aken et al. 2007), highly stable and eucentric in-column specimen stages (Lengweiler 2005; Schmidt et. al 2007), efficient direct electron detectors (Faruqi et al. 2006; Faruqi and Henderson, 2007) and extensive robotics (Suloway et al. 2005). A promising development are correctors for the chromatic aberration, which will be tested in the near future in the course of the TEAM project (Rose 2005; Dahmen 2005). It was shown that inelastic scattering can produce coherent image signal (Lichte and Freitag 2000; Popatov et al. 2007). Especially for CET, converting the background noise originating from inelastic scattering into interpretable image contrast will represent a great benefit.

A schematic drawing, including the critical components to take phase TEM to the next stage, is shown in fig. 7.2. Evidently, the costs of development, assembly and operation for such instruments will be high, and so will be the demands on the knowledge, skill and experience of the the operator. Therefore, rather than maintaining the present situation of having many independently operated low- and medium performance TEMs scattered over different laboratories, it is highly desirable for the future to establish central TEM facilities, running machines with outstanding performance operated by dedicated experts, similar to the current synchrotron facilities for X-ray crystallography. With such tools in hand, insights may be obtained that provide a deeper understanding of the complex workings within cells on a molecular level.

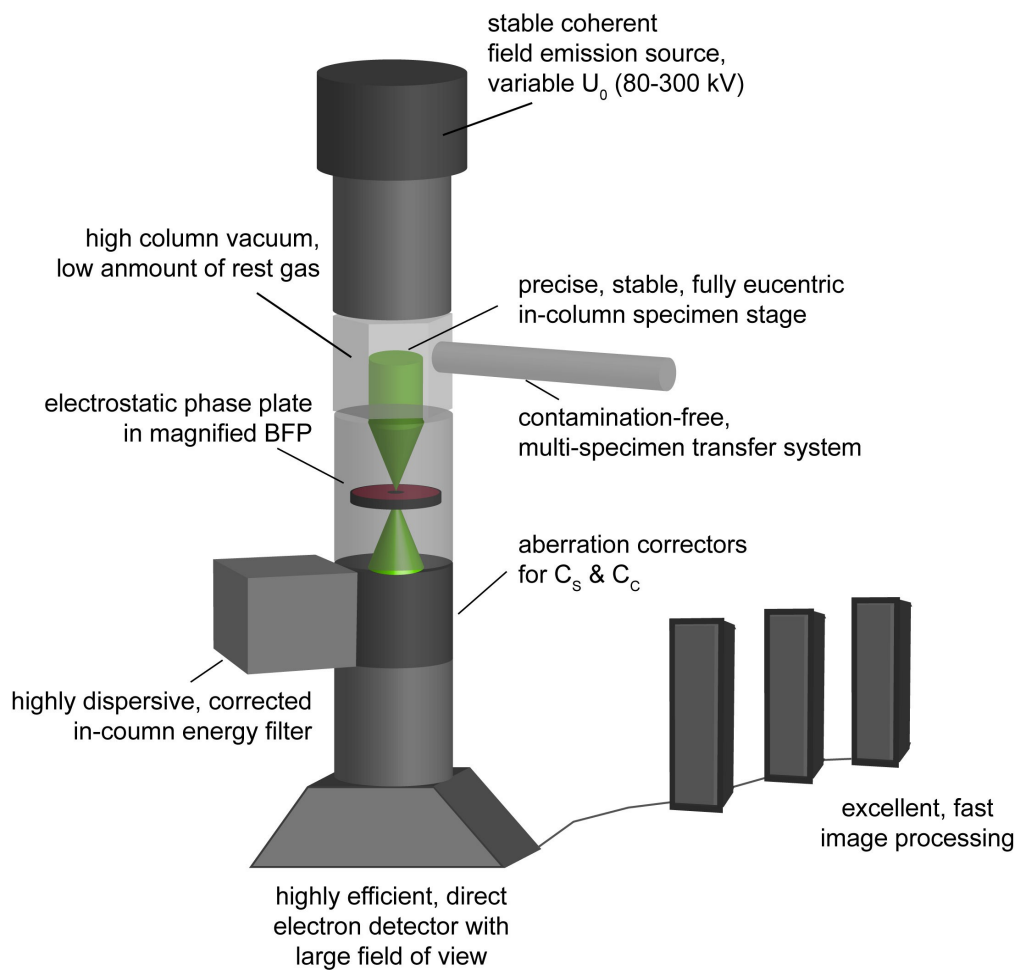


Figure 7.2.: Schematic drawing of an electron microscope equipped with state-of-the-art components to lead biological TEM to perfection.

Appendix A: Basic concepts of electron optics

A.1 Electron lenses

A.1.1 The movement of electrons in a static electromagnetic field

The movement of an electron with charge e inside an electromagnetic field distribution is generally described by the Lorenz equation

$$\frac{d}{dt} \left(\frac{\mathbf{v}}{\sqrt{1-\beta^2}} \right) = \frac{e}{m_0} (\mathbf{E} + \mathbf{v} \times \mathbf{B}) . \quad (1)$$

As the electron beam energies in TEM (80 keV – 1 MeV) are usually in the order of the electron rest mass $m_0 c^2 = 511$ keV, the relativistic form with $\beta = |\mathbf{v}| / c$ has to be used. The electric field vector \mathbf{E} can be expressed as the gradient of a scalar electrostatic potential Φ :

$$\mathbf{E}(\mathbf{r}) = -\text{grad } \Phi(\mathbf{r}) . \quad (2)$$

With the electric potential, the *acceleration potential* $\hat{\Phi}$ can be defined as

$$\hat{\Phi}(\mathbf{r}) = \Phi(\mathbf{r}) [1 + \epsilon \Phi(\mathbf{r})] \quad (3)$$

with $\epsilon = e / (2 m_0 c^2)$. Here, the electron beam energy at the exit of the electron source is arbitrarily set to zero, which is justified if chromatic effects, i.e. the energy distribution of the beam, are not considered.

To deduce the explicit trajectories (x, y) from (1), it is handy to introduce the following quantities: the partial derivative of a coordinate u with respect to the axial coordinate z ,

$$u' = \frac{\partial u}{\partial z} , \quad (4)$$

the tangent of the electron trajectory

$$\rho = |\mathbf{r}'| = \sqrt{1 + x'^2 + y'^2} = \frac{1}{\cos \alpha} , \quad (5)$$

α being the angle of the tangent to the optical axis, and $\eta = \sqrt{e/2m_0}$. The *trajectory equations* in cartesian coordinates are then

$$\begin{aligned}
 x'' &= \frac{e^2}{2\hat{\Phi}} \left(\frac{\partial \hat{\Phi}}{\partial x} - x' \frac{\partial \hat{\Phi}}{\partial z} \right) + \frac{\eta e^2}{\sqrt{\hat{\Phi}}} (e B_y - y' B_t) \\
 y'' &= \frac{e^2}{2\hat{\Phi}} \left(\frac{\partial \hat{\Phi}}{\partial y} - y' \frac{\partial \hat{\Phi}}{\partial z} \right) + \frac{\eta e^2}{\sqrt{\hat{\Phi}}} (-e B_x - x' B_t).
 \end{aligned} \tag{6}$$

B_t denotes the component of the magnetic field vector which is tangential to the trajectory (x, y) .

A.1.2 Round electron lenses and the paraxial equation

Most of the electron lenses of electron microscopes, e.g. condenser and objective lenses in a TEM, or the weak electrostatic Einzel lens described in chapter 3, are round lenses. The setup of the polepieces and electrodes has a rotational symmetry, so that their magnetic field $\mathbf{B}(\tilde{r}, z)$ and electric potential $\hat{\Phi}(\tilde{r}, z)$ distributions only depend on the distance \tilde{r} from the symmetry axis (parallel to the optical axis) and z .

For such lenses, the paraxial approximation can be made, which assumes that all rays propagate within an domain very close to the optical axis. In the regime of the paraxial approximation, terms of the trajectory equations which are quadratic in x and y , their derivatives, and all higher orders are neglected. With this assumption, the tangential component B_t can be replaced by B_z , $B_t = B_z = B$. If then a coordinate system (X, Y, z) rotating around the optical axis is used, such that

$$\begin{aligned}
 x &= X \cos \theta - y \sin \theta \\
 y &= X \sin \theta + y \cos \theta
 \end{aligned} \tag{7}$$

with the angle $\theta(z)$ monotonic in z , the *paraxial equations* as the simplified trajectory equations can be written as

$$\begin{aligned}
 X'' + \frac{y\phi'}{2\hat{\Phi}} X' + \frac{y\phi'' + \eta^2 B^2}{4\hat{\Phi}} X &= 0 \\
 Y'' + \frac{y\phi'}{2\hat{\Phi}} Y' + \frac{y\phi'' + \eta^2 B^2}{4\hat{\Phi}} Y &= 0.
 \end{aligned} \tag{8}$$

Thus, the paraxial equations for a round lens only depend on the axial magnetic field $B = B_z(0, 0, z)$ and the axial potentials $\phi = \Phi(0, 0, z)$ and $\hat{\Phi}(z) = \phi(1 + \epsilon \phi)$. The separation of the coupled trajectory equations (6) is achieved via the transformation to the screw coordinate sys-

tem (X, Y, z) . This reflects the fact that the electron trajectories inside magnetic fields are indeed spirals. The angular velocity of the rotation (*Larmor frequency*) is found to be $d\theta/dt = eB/2m_0\gamma$. In the further descriptions, the notation (x, y, z) will be used instead of (X, Y, z) . Whenever the term “parallel rays” appears, one has to bear in mind that this still means a movement on spiral trajectories around the optical axis.

For a purely magnetic lens, the paraxial equations can be written in the very simple form

$$u'' = F(z) u \quad (9)$$

with $u = X + iY$ and $F(z) = \eta^2 B^2 / 4\hat{\phi}$, describing the focusing action of the lens field.

A.1.3 Asymptotic image formation of round lenses

A general solution for the paraxial equation (8) can be written as

$$x(z) = AG(z) + B\bar{G}(z), \quad (10)$$

i.e. a linear combination of a ray G incident parallel to the optical axis, and a ray \bar{G} that emerges the lens field region parallel to the optical axis. The planes where the asymptotes $\bar{G}(z \rightarrow -\infty)$ and $G(z \rightarrow \infty)$ intersect the optical axis and the parallel axis $x=1$, respectively, are called the *principal planes*, (z_{Pi}, z_{Fi}) and (z_{Fo}, z_{Po}) . The distances between those planes are then the asymptotic focal lengths, $f_i = z_{Fi} - z_{Pi}$ and $f_o = z_{Po} - z_{Fo}$. It can be shown that for lenses which do not change the electron energy, i.e. magnetic lenses and non-accelerating electrostatic lenses, it is always $f_o = f_i$. Furthermore, f_i and f_o are always positive, meaning that such lenses are always convergent.

Using these so-called cardinal elements of the lens, a linear *transfer matrix*

$$T = \begin{pmatrix} -(z_2 - z_{Fi})/f_i & f_o + (z_1 - z_{Fo})(z_2 - z_{Fi})/f_i \\ -1/f_i & (z_1 - z_{Fo})/f_i \end{pmatrix} \quad (11)$$

that describes the imaging of a ray $\mathbf{x} = (x, x')^T$ by the lens from a plane z_1 to another plane z_2 :

$$\mathbf{x}(z_2) = T \mathbf{x}(z_1). \quad (12)$$

A pair of planes z_o, z_i for which T_{12} vanishes, i.e. $f_o f_i = (z_{Fo} - z_o)(z_i - z_{Fi})$, are called *conjugate planes*. For such planes, the matrix elements $T_{11} = -(z_i - z_{Fi})/f_i = M$ and

$T_{22} = -(z_o - z_{F_o})/f_i = M_\alpha$ are the transverse and angular *magnifications* of the lens, respectively. An example for such conjugate planes are the specimen plane and 1st image plane in the objective lens of a TEM.

It is interesting to consider the imaging of a parallel bundle of rays $\mathbf{x}_n = (x_n, c)^T$, with some fixed angle to the optical axis, into the back focal plane z_{F_i} . This corresponds to electrons in the object exit plane that are scattered to some constant angle θ , as $x' = dx/dz = \tan \theta \approx \theta$. By setting $z_1 = 0$, $z_2 = z_{F_i}$, $f_i = f_o$ in (11), one gets

$$\begin{pmatrix} x_n \\ c \end{pmatrix} T^{(ia)} = \begin{pmatrix} cf \\ \theta_a(x_n, c) \end{pmatrix}. \quad (13)$$

The notation $T^{(ia)}$ expresses that this describes the imaging of rays from the image plane to the back focal or aperture plane. In practice, this means that electrons scattered by the same angle in the image plane will be focused into the same fixed point $cf \approx \theta f$ in the back focal plane of the lens. In the important special case $c = \theta = 0$, it says that a bundle of rays parallel to the optical axis will be focused to the focal spot on the axis. Within the wave optical concept described in section A.2, this means that a plane wave entering the lens field will exit the lens as a spherical wave centered around the focal spot $(0, 0, z_F)$ ¹⁷.

A.1.4 Deviations from ideal imaging: lens aberrations

The paraxial equations (8) describe the imaging from the object plane z_o with coordinates x_o, y_o to the image plane z_i with coordinates x_i, y_i in terms of a linear operation, as quadratic and higher terms in x and y are neglected. However, to give a more realistic quantisation of the properties of round electron lenses, also some non-linear effects have to be considered¹⁸. The deviation of an image point $(\Delta x_i, \Delta y_i)$ from the the position determined by the paraxial equations is called the *geometrical aberration*: $(x_o, y_o) \rightarrow (x_i + \Delta x_i, y_i + \Delta y_i)$. Those geometric lens aberrations can be expressed in terms of coefficients in a linear expansion of $\Delta u_i = \Delta x_i + i \Delta y_i$:

¹⁷ This is true if the symmetry axis of the round lens coincides with the optical axis, which is generally the case in a well-aligned TEM.

¹⁸ The explicit mathematical description of these nonlinear contributions involves the evaluation of the quartic terms of the electron optical refraction index and is beyond the scope of the description given here. For a complete mathematical treatment see. REF., pp. 297.

$$\begin{aligned}
 \Delta u_i &= Cr_a^2 u_a && \text{spherical aberration} \\
 &+ 2(K+ik)r_a^2 u_o + (K-ik)u_a^2 u_o^* && \text{coma} \\
 &+ (A+ia)u_o^2 u_a^* && \text{astigmatism} \\
 &+ Fr_o^2 u_a && \text{field curvature} \\
 &+ (D+id)r_o^2 u_o && \text{distortion}
 \end{aligned} \tag{14}$$

$u_a = x_a + i y_a$ are the coordinates in the object plane, and $u_a = x_a + i y_a$ are coordinates in an aperture plane z_a , lying between object and image plane. r_a and r_o are the distances from the optical axis within those planes.

The lens aberrations can be classified according to whether they depend on the the object coordinates (x_o, y_o) , on the aperture plane coordinates (x_a, y_a) or on both.

Aberrations depending only on (x_a, y_a) : The aberrations are independent of the position of the object point and only depend on the intersection point with the aperture plane. On the other hand, they do not vanish if the object point lies on the optical axis. As rays emerging from the same object point can be displaced by different amounts, those aberrations lead to a blurring of image point, or in other words, the object point is imaged into a disc in the image plane. An important case is the spherical aberration, which depends only on the coordinate in the objective back focal plane, i.e. the electron scattering angle. The defocus, corresponding to an image plane that is not exactly conjugate to the object plane, is also a purely aperture-dependent aberration.

Aberrations depending only on (x_o, y_o) : These aberrations are called distortions and shift the paraxial image point by an amount depending on its position in the object plane. They do not cause blurring of the point.

Intermediate aberrations: Examples for this kind of aberrations are comas (linear in x_o and y_o) astigmatism.

A.1.5 Spherical aberration

As mentioned in section A.1.4, the spherical aberration term causes the imaging of a point into a disc

$$x_i = M \left\{ x_o + C x_a (x_a^2 + y_a^2) \right\}. \tag{15}$$

If z_a is confined to an aperture with radius r_A , through which only rays with $x_a^2 + y_a^2 \leq r_A^2$ can

pass, the aberration disc will have a radius MCr_A^3 . Expressed by the angle x_i' at which the outermost ray intersects the object plane, which corresponds to the scattering angle in the case of parallel specimen illumination, the aberration is

$$\Delta x_i = C_s x_o' (x_o'^2 + y_o'^2). \quad (16)$$

C_s is called the spherical aberration coefficient. With $x' = dx/dz = \tan \theta \approx \theta$ for small angles¹⁹, the radius of the aberration disc is $MC_s \theta^3$.

A.2 From particle to wave optics

A.2.1 The paraxial Schrödinger equation

The relativistic *Schrödinger equation* (or scalar *Dirac equation*) for an electron wave inside an electromagnetic field with electric potential $\hat{\Phi}$ (see eq. 3) and vector potential \mathbf{A} can be formulated as

$$\nabla^2 \Psi + \frac{2ie}{\hbar} \mathbf{A} \cdot \nabla + \frac{1}{\hbar^2} (2m_0 e \hat{\Phi} - e^2 \mathbf{A}^2) \Psi = -\frac{2im}{\hbar} \frac{\partial \Psi}{\partial t}. \quad (17)$$

As in the previous sections, round lens systems are considered where the potentials $\hat{\Phi}$ and \mathbf{A} are rotationally symmetric. If an electron beam leaving the cathode at an energy $E_0 = 0$ and a small chromatic energy spread $e\Delta\phi$ is assumed, the Schrödinger equation on the axis is

$$\frac{\partial \Psi_0}{\partial z^2} + \frac{g^2(z)}{\hbar^2} \Psi_0 = 0 \quad (18)$$

with the axial momentum $g(z) = \sqrt{2m_0 e \hat{\Phi}(z) + 2m e \Delta\phi}$.

A solution to (17) has the form

$$\Psi(\mathbf{r}, t) = \Psi_0(z, t) \psi_p(\mathbf{r}) \quad (19)$$

with an axial component Ψ_0 and a paraxial component ψ_p . Within the paraxial approximation, the electric potential can be expanded as

¹⁹ As the scattering angles for electrons with high energies of a few hundred keV are in the range of mrad, this assumption is justified.

$$\begin{aligned}\Phi(z, r) &= \phi(z) - \frac{r^2}{4} \phi''(z) + O(r^4) \\ \hat{\Phi} &= \hat{\phi}(z) - y \frac{r^2}{4} \phi''(z) + O(r^4)\end{aligned}\tag{20}$$

and the square of the vector potential as

$$A^2(z, r) = \frac{1}{4} r^2 B^2(z) + O(r^4).\tag{21}$$

The linear terms of the vector potential can be eliminated by transforming the problem into the rotating coordinate system described in section A.1.2. After a few further simplifications, the paraxial wave equation becomes

$$\frac{\partial^2 \psi}{\partial x^2} + \frac{\partial^2 \psi}{\partial y^2} + \frac{2i}{\hbar} g(z) \psi - \frac{r^2}{\hbar^2} \left\{ \frac{e m(z)}{2} \psi''(z) + \frac{e^2 B^2(z)}{4} \right\} = 0.\tag{22}$$

Similar to (9), the wave equation can be further simplified by defining a lens function, which now also includes the chromatic energy spread of the beam:

$$F(z) = \frac{\gamma \phi'' + \eta^2 B^2}{4 \phi (1 + e \phi + 2 \epsilon \Delta \phi)}\tag{23}$$

With this, (22) can be rewritten as

$$\underbrace{-\frac{\hbar^2}{2m} \left(\frac{\partial^2 \psi}{\partial x^2} + \frac{\partial^2 \psi}{\partial y^2} \right)}_{\text{transverse kinetic energy}} + \underbrace{\frac{g^2 F}{2m} (x^2 + y^2) \psi}_{\text{quadratic focusing potential}} = \underbrace{\frac{i \hbar g}{m} \frac{\partial \psi}{\partial z}}_{\text{axial velocity}}.\tag{24}$$

A.2.2 Propagation of the electron wave through a round lens

A general solution for the paraxial wave equation (24) is an electron described by a wave packet propagating from the object plane z_o :

$$\psi(x, y, z) = \iint C(x_o, y_o) \exp \left\{ \frac{i}{\hbar} \bar{S}(x, y, z, x_o, y_o, z_o) \right\} \frac{dx_o dy_o}{h_p(z)}.\tag{25}$$

Here, $h_p(z)$ is a ray that intersects the object plane on the optical axis. The phases \bar{S} of the elementary waves are called the *eikonal*. $C(x_o, y_o)$ is the amplitude change (absorption) by the object. With the help of a pair of basic solutions for the paraxial ray equation (8), $h_p(z)$ and

$g_p(z)$, the propagation of the wave packet through the lens can be evaluated. Two important facts can be found:

1. The intensity distribution at the image plane z_i , where $h_p(z_i)=0$ is identical to the intensity in the object (exit) plane, magnified by the factor $M=g_p'(z_i)$:

$$|\psi(x_i, y_i, z_i)|^2 = M^{-2} |\psi(x_i/M, y_i/M, z_o)|^2 \quad (26)$$

2. The wave function in the back focal plane z_F of the lens, where $g_p(z_F)=0$, is equal to the inverse Fourier transform F^{-1} of the object exit wave:

$$\psi(x, y, z_F) = -\frac{ie^{i\varphi}}{\lambda_f f} F^{-1}(\psi(z=z_o)) \quad (27)$$

Here, $e^{i\varphi}$ is an unimportant phase factor, $\lambda_f=2\pi\hbar/g(z_F)$ is the wavelength in the BFP and $f=-1/g_p'(z_F)$ is the focal length of the lens.

A.2.3 The wave-optical description of lens aberrations

As shown in section A.1.3, a perfect lens within the paraxial approximation will transform a plane incident wave into a spherical wave, whose phase is described by the eikonal \bar{S} in the wave optical description. Deviations from the paraxial behavior can be quantified in terms of the lens aberrations (14). Thus, the aberration terms can be written as “distortions” of the eikonal, i.e. additional phase factors:

$$\begin{aligned} W &= \frac{1}{4} C_s \theta^4 && \text{spherical aberration} \\ &- \frac{1}{2} Z \theta^2 && \text{defocus} \\ &+ \theta (d_1 \cos \varphi_o + d_2 \sin \varphi_o) && \text{deflection axial coma} \\ &+ \frac{1}{3} \theta^3 (c_1 \cos \varphi_o + c_2 \sin \varphi_o) && \text{cubic axial coma} \\ &+ \frac{1}{2} \theta^2 (a_1^{(2)} \cos 2\varphi_o + a_2^{(2)} \sin 2\varphi_o) && \text{twofold axial astigmatism} \\ &+ \frac{1}{3} \theta^3 (a_1^{(3)} \cos 3\varphi_o + a_2^{(3)} \sin 3\varphi_o) && \text{threefold axial astigmatism} \end{aligned} \quad (28)$$

Here, θ is again the object scattering angle, Z is the distance from the specimen to the object plane of the lens and φ_o is the azimuthal angle in the object plane. If the scattering angle is again ex-

pressed by the coordinates in the back focal plane,

$$\mathbf{k} = \mathbf{u}_a / \lambda f \quad \text{and} \quad |\mathbf{k}| = k = r_a / \lambda f, \quad (29)$$

the modulation of the wave front can be written as a transfer function depending on \mathbf{k} :

$$T_L(\mathbf{k}) = \exp \left\{ -i \frac{\pi}{2} (C_s \lambda^3 k^4 - 2Z \lambda k^2) \right\} \quad (30)$$

The “parasitic”, i.e. non-rotationally symmetric terms in (28) are not considered because they can be eliminated in practice with the help of stigmators.

It is sometimes useful to write T_L in terms of the reduced spatial frequency $Q = (C_s \lambda^3)^{1/4} k$ and the reduced defocus $D = Z / (C_s \lambda)^{1/2}$:

$$T_L(Q) = \exp \left\{ i \frac{\pi}{2} (2DQ^2 - Q^4) \right\} \quad (31)$$

Appendix B: Fabrication of Hilbert carbon film phase plates

For the deposition of the 20-50 nm thick amorphous carbon layers, a carbon coating system (Edwards Auto 306, Edwards, London, UK; fig B1 A) was used. Carbon was evaporated from a heated carbon rod onto freshly cleaved mica sheets under high vacuum conditions. The thickness was monitored using a built-in oscillating quartz. The error of thickness determination is estimated to be $\sim \pm 5$ nm. After evaporation the carbon film was floated off the mica on a water surface, which was then lowered onto 10-20 EM specimen grids (100-300 mesh molybdenum).

Two different fabrication techniques were applied. For the tomography experiments in the SESAM, a large number of phase plates had to be loaded into the TEM. The wet carbon film was ruptured and one half of the carbon layer was removed from each grid, producing a long carbon edge (fig B.1 B, C). The result was observed under the light microscope and grids with a large number of straight edges were selected. Two grids containing 30-100 physical Hilbert phase plates (cf. fig B.1 C) were mounted on a piezo-driven positioning system (cf. fig. 3.3). The positioning system was attached to the objective of the TEM, so that the phase plates could be positioned to the BFP of the objective lens during image recording.

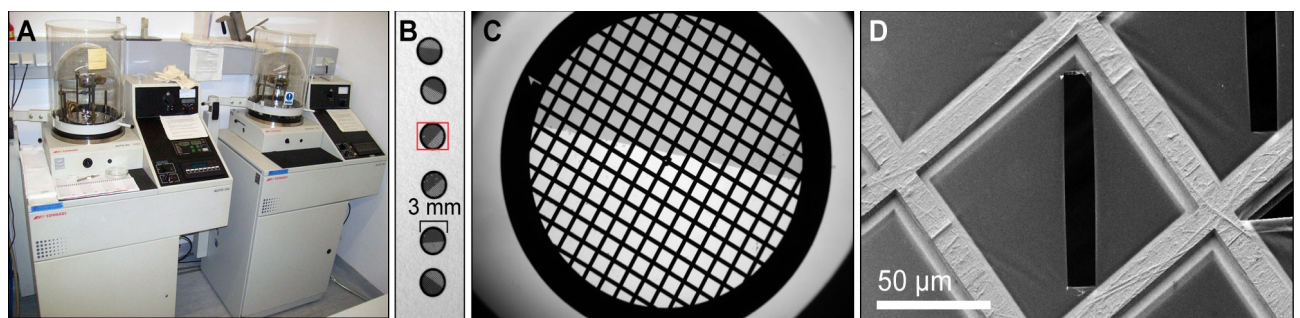


Figure B.1.: (A) Edwards Auto 306 carbon coating system with oscillating crystal thickness monitor. (B) Light microscope image of carbon film half planes deposited on 100 mesh electron microscopy specimen grids. (C) Framed area in B. The edge length of the grid squares is ~ 200 μm . The electron beam diameter in the BFP is < 60 μm , so that a carbon edge spanning one grid square represents 3-5 Hilbert phase plates. (D) SEM image of a rectangle patterned into the carbon film by a FIB (see text).

For use in the Polara, Hilbert phase plates were produced at the Laboratorium für Elektronenmikroskopie at the University of Karlsruhe. Rectangles were patterned into the carbon film using the 30kV Ga⁺ focussed ion beam of a Zeiss EsB1540 SEM/FIB dual-beam instrument (Zeiss NTS, Oberkochen, Germany). Each rectangle had edge lengths of 60-100 μm, thus providing 3-4 Hilbert phase plates. The FIB milling technique had the advantage of a cleaner and in general more straight carbon edge. On the other hand, the rupturing technique provided minimum fabrication effort and at the same time produced a larger number of physical phase plates. From a multitude of carbon-covered grids, the best edges were selected. Therefore, both fabrication techniques yielded equivalent Hilbert contrast.

Appendix C: Construction of a Piezo-driven Phase Plate Goniometer

To provide an accurate and stable positioning of the electrostatic phase plates in the magnified BFP of the future PACEM instrument, a piezo-driven in-column stage was developed and built. The design follows the fully eucentric in-column specimen stage developed by Lengweiler (2005). The translation of the tip in x, y (lateral) and z (beam direction) is generated by a slick-and-slide movement of ruby hemispheres along sapphire rails. The rubies are attached to plates consisting of a piezoactive material (PI Ceramic, Lederhose, Germany). The principle of such a piezo drive is shown in fig. C.1.

Figure C.1.: Principle of the slick-and-slide movement of the piezo drives generating the translational movement of the phase plate goniometer. The shear piezos perform a slow movement (ms) which displaces the load (S) by a distance of a few nm. The subsequent movement back to the initial position is extremely fast (75 ns), which causes the ruby hemispheres (RH) to slide along the sapphire rails without moving the load. The rubies are held in contact with the sapphire rails by a titanium frame (TF).

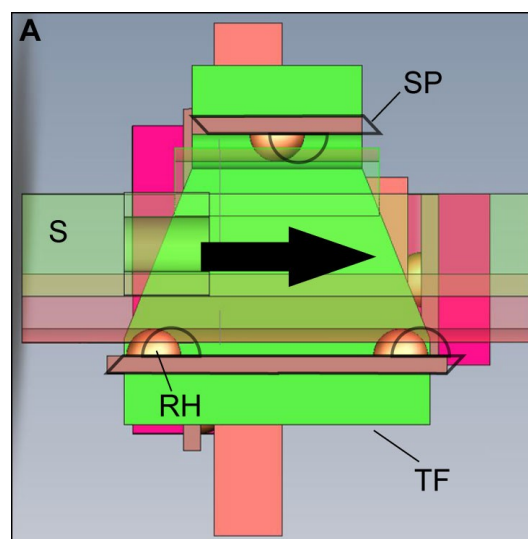


Figure C.2 shows the functional prototype of the positioning system which was designed to be tested in the PACEM. The goniometer is mounted inside a modified vacuum flange to attach the system to the TEM column. The flange has a vacuum feed-through for the necessary voltage supply. The range of movement allows to completely retract the phase plates from the beam path if they are not needed.

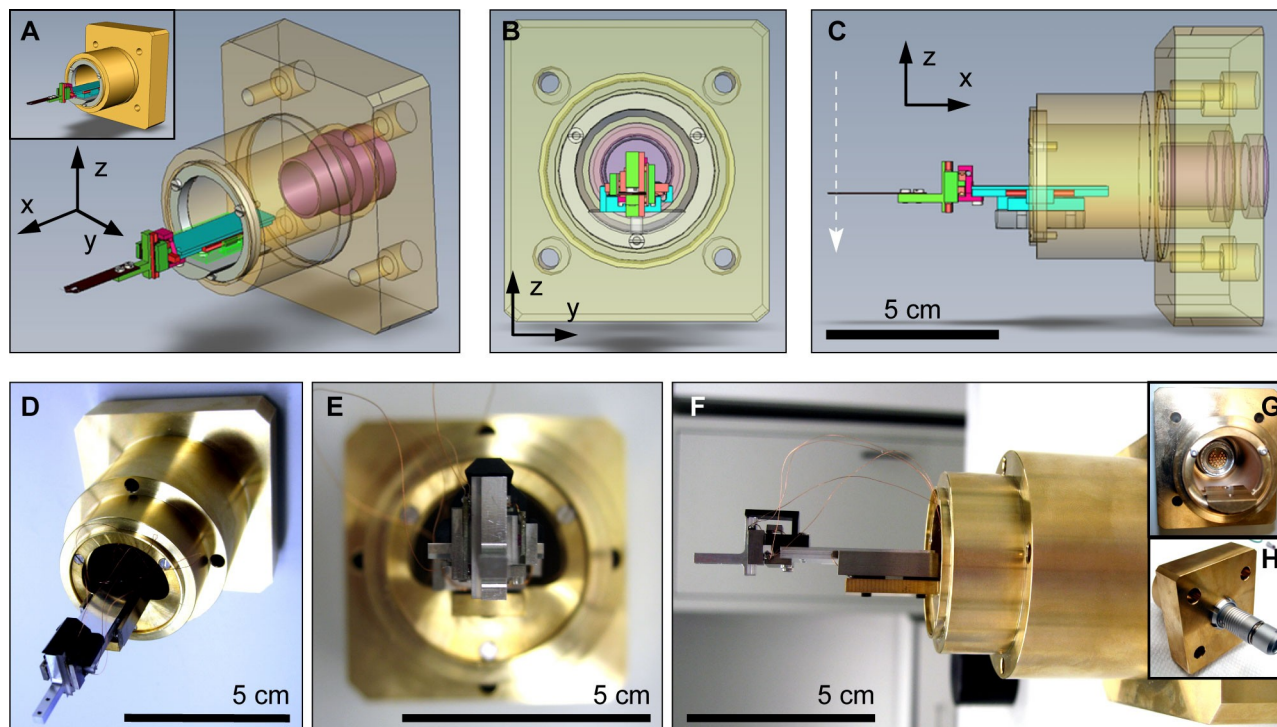


Figure C.2.: (A-C) CAD design of the phase plate positioning system. (D-E) Prototype of the goniometer.

Appendix D: Digital image processing with MatLab

For many experiments carried out for this work, non-standard image processing was required to evaluate the raw image data. Software packages like SPIDER, although very useful and widely used for routine EM image processing, often do not provide the necessary flexibility. Therefore, a large number of special algorithms were programmed using the software package MatLab (The Math Works, USA). MatLab offers a suitable platform for image processing because it handles all variables as matrices. This makes the handling of TEM images which are recorded in the form of square matrices of grey values (CCD camera counts) convenient. The software provides many elementary operations such as image addition, Fourier transformation and rotation, which can then be combined to more complex routines. The functions are written in a intuitive language similar to C. Matlab also provides elementary functions of image display and data visualisation (cf. fig. 6.12).

Two examples for the programs that were written are shown here. The first routine *spektrum.m* generates a periodogram of an image. A periodogram is generated from a number of overlapping windows that are rasterized over an image. Of each window, the power spectrum is calculated, and the resulting power spectra are averaged to obtain a low-noise representation of the modulus of the image Fourier transform.

```
function PW=spektrum

datei=input('Dateiname: ','s');
warning off all;
datei=uigetfile('*.tif','TIFF-Datei auswaehlen');
%figure('Name',[pwd '/' datei]);
M=imread(datei,'tiff');
PW=pw(M);
bild(log(PW),datei);
set(gcf,'Name',[pwd '/' datei]);
%text(20,20,datei,'FontSize',16,'Color','white');

function PW = pw(M);

% Dimensionen festlegen
bild=size(M);
fenster=round(size(M)/4);
anz=floor(bild./fenster*2-1);
PW=zeros(fenster*2);
```

```

% Gaussmaske erzeugen
if fenster==[257 256]
    load('/Applications/Matlab/toolbox/Bastians
Toolbox/data/gaussmaske','GAUSS');
else
    GAUSS=gaussmaskel(fenster*2,min(fenster*2/8));
end

% Oversampling mit Einbetten
for y=1:fenster(1)/2:size(M,1)-fenster(1);
    for x=1:fenster(2)/2:size(M,2)-fenster(2);
        %rect is a four-element vector with the form
        %[xmin ymin width height];
        CR=imcrop(M,[x y fenster(2)-1 fenster(1)-1]);
        B=bett(CR);
        G=B.*GAUSS;
        PW=PW+abs(fft2(G)).^2;
    end
end

% Umordnen der 4 Bildquadranten
PW=fftshift(PW);

```

The second example *hilbert_corr_fermi.m* is used to correct for the anti-symmetric PSF in HPC images. The Fourier Transform of an image is calculated, the FFT is rotated so that the HPC contrast gap is oriented horizontally. Then, both halves are modulated by a phase image with corresponding to a Fermi distribution in vertical direction. The Fourier back transform is performed to obtain the corrected image.

```

function [C D] =hilbert_corr_fermi(I,alpha,b,phi);

% In Fromat "double" umwandeln
% DI=double(I);

% Fouriertransformation rechnen
F=fft2(I);
SF=fftshift(F);

% drehen sodass Spalt horizontal liegt (entlang [ x]-Koordinate)
RSF=imrotate(SF,alpha,'crop');
% figure, bild(log(abs(RSF)))

% Phasenfaktoren
pf = exp(i*(phi/2));

% Fermikante
[fe FE] = fermi(size(I,2),round(size(I,2)/2),b);
FE = exp(FE*i*phi/2);

% Multiplizieren
CRSF = RSF .* FE;

```

```
% zurckdrehen
CSF=imrotate(CRSF,-alpha,'crop');

% Rcktransformation
CF=ifftshift(CSF);
CC=ifft2(CF);

% Realteil, falls ifft Imaginrteile ergibt
C=uint16(real(CC));

% % Zeigen
% figure('Name','Original');
% bild(I);
% figure('Name',['Hilbert-korrigiert, alpha= ' num2str(alpha) ', b = '
num2str(b) ', phi = ' num2str(phi)']);
% bild(C);
```

Bibliography

- Angert, I., Majorovits, E. and Schröder, R. R., 2000. Zero-loss image formation and modified contrast transfer theory in EFTEM. *Ultramicroscopy* 81, 203-222.
- Ban, N., Nissen, P., Hansen, J., Moore, P. B. and Steitz, T. A., 2000. The complete atomic structure of the large ribosomal subunit at 2.4 Å resolution. *Science* 289, 905-920.
- Barton, B., 2005. Elektrostatische Phasenplatten für die Transmissions-Elektronenmikroskopie. PhD Thesis, University of Heidelberg, Germany
- Beck, M., Forster, F., Ecke, M., Plitzko, J. M., Melchior, F., Gerisch, G., Baumeister, W. and Medalia, O., 2004. Nuclear pore complex structure and dynamics revealed by cryoelectron tomography. *Science* 306, 1387-1390.
- Beck, M., Lucic, V., Forster, F., Baumeister, W. and Medalia, O., 2007. Snapshots of nuclear pore complexes in action captured by cryo-electron tomography. *Nature* 449, 611-615.
- Boersch, H., 1947. Über die Kontraste von Atomen im Elektronenmikroskop. *Z. Naturforschung* 2a, 615.
- Bohm, J., Frangakis, A. S., Hegerl, R., Nickell, S., Typke, D. and Baumeister, W., 2000. Toward detecting and identifying macromolecules in a cellular context: Template matching applied to electron tomograms. *Proceedings of the National Academy of Sciences of the United States of America* 97, 14245-14250.
- Cambie, R., Downing, K. H., Typke, D., Glaeser, R. M. and Jin, J., 2007. Design of a microfabricated, two-electrode phase-contrast element suitable for electron microscopy. *Ultramicroscopy* 107, 329-339.
- Cheng, Y., Boll, W., Kirchhausen, T., Harrison, S. C. and Walz, T., 2007. Cryo-electron tomography of clathrin-coated vesicles: structural implications for coat assembly. *J Mol Biol* 365, 892-899.
- Coene, W.M.J., Thust A., de Beeck M.O., Van Dyck, D., 1996. Maximum-likelihood method for focus-variation image reconstruction in high resolution transmission electron microscopy. *Ultramicroscopy* 64, 109-135.
- Dahmen, U., 2005. The TEAM Project – An Update. *Microsc Microanal* 11 (Suppl 2)
- Danev, R. and Nagayama, K., 2001a. Complex observation in electron microscopy. II. Direct visualization of phases and amplitudes of exit wave functions. *Journal of the Physical Society of Japan* 70, 696-702.
- Danev, R. and Nagayama, K., 2001b. Transmission electron microscopy with Zernike phase plate. *Ultramicroscopy* 88, 243-252.

- Danev, R. and Nagayama, K., 2004. Complex observation in electron microscopy: IV. Reconstruction of complex object wave from conventional and half plane phase plate image pair. *Journal of the Physical Society of Japan* 73, 2718-2724.
- Danev, R. and Nagayama, K., 2008. Single particle analysis based on Zernike phase contrast transmission electron microscopy. *Journal of Structural Biology* 161, 211-218.
- Dinges, C., Berger, A. and Rose, H., 1995. Simulation of TEM images considering phonon and electronic excitations. *Ultramicroscopy* 60, 49.
- Dubochet, J., Booy, F. P., Freeman, R., Jones, A. V. and Walter, C. A., 1981. Low temperature electron microscopy. *Annu Rev Biophys Bioeng* 10, 133-149.
- Faruqi, A. R. and Henderson, R., 2007. Electronic detectors for electron microscopy. *Curr Opin Struct Biol* 17, 549-555.
- Faruqi, A. R., Henderson, R. and Holmes, J., 2006. Radiation damage studies on STAR250 CMOS sensor at 300keV for electron microscopy. *Nuclear Instruments & Methods in Physics Research Section A-Accelerators Spectrometers Detectors & Associated Equipment* 565, 139-143.
- Frangakis, A. S. and Forster, F., 2004. Computational exploration of structural information from cryo-electron tomograms [Review]. *Current Opinion in Structural Biology* 14, 325-331.
- Frangakis, A. S. and Hegerl, R., 2001. Noise reduction in electron tomographic reconstructions using nonlinear anisotropic diffusion. *Journal of Structural Biology* 135, 239-250.
- Frank J., Rademacher, M., Penczek, P., Zhu, J., Li, Y., Ladjadj, M. and Leith, A., 1996. SPIDER and WEB processing and visualization of images in 3D electron microscopy and related fields. *J. Struct. Biol.* 116, 190.
- Frank, J. and Penczek, P., 1995. On the Correction of the Contrast Transfer Function in Biological Electron Microscopy. *Optik* 98, 125-129.
- Frank, J., 1996. *Three-dimensional electron microscopy of Macromolecular Assemblies*. Academic Press.
- Gabor, D., 1948. A New Microscopic Principle. *Nature*, 161, 777-778.
- Gamm, B., Schultheiß, K., Gerthsen, D. and Schröder, R. R., 2007. Effect of a Physical Phase Plate on Contrast Transfer in an Aberration-Corrected Transmission Electron Microscope. *Ultramicroscopy*, submitted
- Gonen, T., Sliz, P., Kistler, J., Cheng, Y. F. and Walz, T., 2004. Aquaporin-0 membrane junctions reveal the structure of a closed water pore. *Nature* 429, 193-197.
- Grimm, R., Barmann, M., Hackl, W., Typke, D., Sackmann, E. and Baumeister, W., 1997. Energy filtered electron tomography of ice-embedded actin and vesicles. *Biophys J* 72, 482-489.
- Haider, M. and Müller, H., 2004. Design of an Electron Optical System for the Correction of the

Chromatic Aberration Cc of a TEM Objective Lens. *Microscopy and Microanalysis* 10, 2-3.

- Haider, M., Rose, H., Uhlemann, S., Kabius, B. and Urban, K., 1998. Towards 0.1 Nm Resolution with the First Spherically Corrected Transmission Electron Microscope. *Journal of Electron Microscopy* 47, 395-405.
- Haider, M., Rose, H., Uhlemann, S., Schwan, E., Kabius, B. and Urban, K., 1998. A Spherical-Aberration-Corrected 200 Kv Transmission Electron Microscope. *Ultramicroscopy* 75, 53-60.
- Haider, M., Uhlemann, S., Schwan, E., Rose, H., Kabius, B. and Urban, K., 1998. Electron Microscopy Image Enhanced. *Nature* 392, 768-769.
- Han, K. F., Sedat, J. W. and Agard, D. A., 1995. Mechanism of Image Formation for Thick Biological Specimens - Exit Wavefront Reconstruction and Electron Energy-Loss Spectroscopic Imaging. *Journal of Microscopy* 178, 107-119.
- Harscher, A. and Lichte, H. 1998. *Int Conf Electron Microsc ICEM14*.
- Henderson, R., 1992. Image contrast in high-resolution electron microscopy of biological macromolecules: TMV in ice. *Ultramicroscopy* 46, 1-18.
- Henderson, R., 1995. The Potential and Limitations of Neutrons, Electrons and X-Rays for Atomic Resolution Microscopy of Unstained Biological Molecules. *Quarterly Reviews of Biophysics* 28, 171-193.
- Holmes, K. C., Angert, I., Kull, F. J., Jahn, W. and Schroder, R. R., 2003. Electron cryo-microscopy shows how strong binding of myosin to actin releases nucleotide. *Nature* 425, 423-427.
- Hosokawa, F., Danev, R., Arai, Y. and Nagayama, K., 2005. Transfer doublet and an elaborated phase plate holder for 120 kV electron-phase microscope. *Journal of Electron Microscopy* 54, 317-324.
- Hsieh, W. K., Anderson E., Benner, G., Park M., Gomez, E., Balsara, N. and Kisielowski, C., 2007. Contrast Transfer Function Design by an Electrostatic Phase Plate. *Microscopy and Microanalysis 2007, Ft. Lauderdale, (USA)*
- Huang, S. H., Wang, W. J., Chang, C. S., Hwu, Y. K., Tseng, F. G., Kai, J. J. and Chen, F. R., 2006. The fabrication and application of Zernike electrostatic phase plate. *Journal of Electron Microscopy* 55, 273-280.
- Jensen, G. J. and Briegel, A., 2007. How electron cryotomography is opening a new window onto prokaryotic ultrastructure. *Current Opinion in Structural Biology* 17, 260-267.
- Kabius, B., Haider, M., Uhlemann, S., Schwan, E., Urban, K. and Rose, H., 2002. First application of a spherical-aberration corrected transmission electron microscope in materials science. *Journal of Electron Microscopy* 51, S51-S58.
- Kaneko, Y., Danev, R., Nagayama, K., Nakamoto, H., 2006. Intact carboxysomes in a cyanobacterial cell visualized by Hilbert differential contrast transmission electron microscopy. *J. Bacteriol* 188, 805-808.

- Kaneko, Y., Danev, R., Nitta, K. and Nagayama, K., 2005. In vivo subcellular ultrastructures recognized with Hilbert differential contrast transmission electron microscopy. *Journal of Electron Microscopy* 54, 79-84.
- Kühlbrandt, W., Wang, D. N. and Fujiyoshi, Y., 1994. Atomic model of plant light-harvesting complex by electron crystallography. *Nature* 367, 614-621.
- Lengweiler, S., 2005. Fully eucentric piezo mechanical goniometer to facilitate electron tomography. Diss., Technische Wissenschaften, Eidgenössische Technische Hochschule ETH Zürich, Nr. 16167.
- Lentzen, M., 2004. The tuning of a Zernike phase plate with defocus and variable spherical aberration and its use in HRTEM imaging. *Ultramicroscopy* 99, 211-220.
- Lichte H. and Freitag, B., 2000. Inelastic electron holography. *Ultramicroscopy* 81, 177-186.
- Lucic, V., Forster, F. and Baumeister, W., 2005. Structural studies by electron tomography: from cells to molecules. *Annu Rev Biochem* 74, 833-865.
- Lucic, V., Kossel, A. H., Yang, T., Bonhoeffer, T., Baumeister, W. and Sartori, A., 2007. Multiscale imaging of neurons grown in culture: From light microscopy to cryo-electron tomography. *Journal of Structural Biology* 160, 146-156.
- Majorovits, E. (2002). Assessing Phase Contrast Electron Microscopy with Electrostatic Boersch- and Zernike-type Phase Plates. PhD Thesis, University of Heidelberg.
- Majorovits, E., Barton, B., Schultheiss, K., Perez-Willard, F., Gerthsen, D. and Schroder, R. R., 2007. Optimizing phase contrast in transmission electron microscopy with an electrostatic (Boersch) phase plate. *Ultramicroscopy* 107, 213-226.
- Marko, M., Hsieh, C.-E., K.A., D., Typke, D., Mannella, C. A. and Frank, J., 2005. Use of the Zernike Phase Plate for Electron Tomography of Frozen-Hydrated Specimens. *Microsc Microanal* 11, 310 – 311.
- Matsumoto, T. and Tonomura, A., 1996. The Phase Constancy of Electron Waves Traveling through Boersch's Electrostatic Phase Plate. *Ultramicroscopy* 63, 5-10.
- Matsumoto, T., Tonomura, A. and Osakabe, N., 1997. Phase contrast electron microscope and phase plate therefore. European patent application #96120384.1 () 20
- McBride, W. and Allen, L. J., 2004. Phase imaging with a half-plane aperture. *Journal of the Optical Society of America A-Optics & Image Science* 21, 1172-1178.
- McMullan, G., Cattermole, D. M., Chen, S., Henderson, R., Llopart, X., Summerfield, C., Tlustos, L. and Faruqi, A. R., 2007. Electron imaging with Medipix2 hybrid pixel detector. *Ultramicroscopy* 107, 401-413.
- Medalia, O., Weber, I., Frangakis, A. S., Nicastro, D., Gerisch, G. and Baumeister, W., 2002. Macromolecular architecture in eukaryotic cells visualized by cryoelectron tomography. *Science* 298, 1209-1213.

-
- Müller, H., Rose, H. and Schorsch, P., 1998. A coherence function approach to image simulation. *J. of Microscopy* 190, 73.
- Müller, H., Uhlemann, S., Hartel, P. and Haider, M., 2006. Advancing the hexapole C-s-corrector for the scanning transmission electron microscope. *Microscopy & Microanalysis* 12, 442-455.
- Nagayama, K., 2002. A Novel Phase-contrast Transmission Electron Microscopy Producing High-contrast Topographic Images of Weak objects. *Journal of Biological Physics* 28, 627 - 635.
- Nagayama, K., 2005. The to complex optics Ultimate phase-contrast method IV - The utilization of Aharonov-Bohm effect. *O plus E* 313, 1448-1451.
- Nagayama, R. D. K. 2006. Single Particle Analysis of Image Data Acquired by Zernike Phase Contrast Transmission Electron Microscopy. 16th International Microscopy Congress, Sapporo (Japan).
- Nickell, S., Mihalache, O., Beck, F., Hegerl, R., Korinek, A. and Baumeister, W., 2007. Structural analysis of the 26S proteasome by cryoelectron tomography. *Biochemical & Biophysical Research Communications* 353, 115-120.
- Penczek, P., Radermacher, M. and Frank, J., 1992. Three-dimensional reconstruction of single particles embedded in ice. *Ultramicroscopy* 40, 33-53.
- Potapov, P.L., Verbeeck, J., Schattschneider, P., Lichte, H. and van Dyck, D., 2007. Inelastic electron holography as a variant of the Feynman thought experiment. *Ultramicroscopy* 107, 559-567.
- Reimer, L., 1984. *Transmission Electron Microscopy* (Springer Series in Optical Sciences; v. 36). Springer-Verlag, Berlin.
- Robinson, C. V., Sali, A. and Baumeister, W., 2007. The molecular sociology of the cell [Review]. *Nature* 450, 973-982.
- Rose, H., 2004. Outline of an ultracorrector compensating for all primary chromatic and geometrical aberrations of charged-particle lenses. *Nuclear Instruments and Methods in Physics Research Section A* 519, 12-27
- Rose, H., 2005. Prospects for aberration-free electron microscopy. *Ultramicroscopy* 103, 1-6.
- Sartori, A., Gatz, R., Beck, F., Rigort, A., Baumeister, W. and Plitzko, J. M., 2007. Correlative microscopy: Bridging the gap between fluorescence light microscopy and cryo-electron tomography. *Journal of Structural Biology* 160, 135-145.
- Schmid, A.K., Duden, T., Olson, E., Donchev, T. and Petrov, I., 2007. In-column Piezo-Stages and Experimental Opportunities. *Microscopy and Microanalysis 2007*, Ft. Lauderdale (USA).
- Schröder, R. R., 2004. Hybrid electron microscopy: Neue Wege bei der Kombination röntgenkristallographischer und elektronenmikroskopischer Strukturdaten. *Biospektrum* 10, 743-744.
- Schröder, R. R., Barton, B., Rose, H. and Benner, G., 2007. Contrast Enhancement by Anamorphot-

- ic Phase Plates in an Aberration Corrected TEM. *Microsc Microanal* 13, 136 - 137.
- Schröder, R. R., Manstein, D. J., Jahn, W., Holden, H., Rayment, I., Holmes, K. C. and Spudich, J. A., 1993. Three-dimensional atomic model of F-actin decorated with Dictyostelium myosin S1. *Nature* 364, 171-174.
- Schultheiß, K., Perez-Willard, F., Barton, B., Gerthsen, D. and Schroder, R. R., 2006. Fabrication of a Boersch phase plate for phase contrast imaging in a transmission electron microscope - art. no. 033701. *Review of Scientific Instruments* 77, 33701.
- Setou, M., Danev, R., Atsuzawa, K., Yao, I., Fukuda, Y., Usuda, N. and Nagayama, K., 2006. Mammalian cell nano structures visualized by cryo Hilbert differential contrast transmission electron microscopy. *Med Mol Morph* 39, 176-180.
- Simon, P., Lichte, H., Drechsel, J., Formanek P., Graff, A., Wahl, R., Mertig, M., Adhikari, R. and Michler, G.H., 2003. Electron holography of organic and biological materials. *Adv. Mater.* 15, 1475
- Simon, P., Lichte, H., Wahl, R., Mertig, M. and Pompe, W., 2004. Electron holography of non-stained bacterial surface layer proteins. *Biochim. Biophys. Acta* 1663, 178.
- Stoffler, D., Feja, B., Fahrenkrog, B., Walz, J., Typke, D. and Aebi, U., 2003. Cryo-electron tomography provides novel insights into nuclear pore architecture: Implications for nucleocytoplasmic transport. *Journal of Molecular Biology* 328, 119-130.
- Suloway, C., Pulokas, J., Fellmann, D., Cheng, A., Guerra, F., Quispe, J., Stagg, S., Potter, C. S. and Carragher, B., 2005. Automated molecular microscopy: the new Legimon system. *J Struct Biol* 151, 41-60.
- Tagari, M., Newman, R., Chagoyen, M., Carazo, J. M. and Henrick, K., 2002. New electron microscopy database and deposition system. *Trends in Biochemical Sciences* 27, 589.
- Taylor, K. A. and Glaeser, R. M., 1976. Electron microscopy of frozen hydrated biological specimens. *J Ultrastruct Res* 55, 448-456.
- Tochigi, H. et al., 1970. The improvement of the image contrast by using the phase plate in the TEM. *Microscopie Electronique* 1, 73
- Toyoshima, C. and Unwin, N., 1988. Contrast transfer for frozen-hydrated specimens: determination from pairs of defocused images. *Ultramicroscopy* 25, 279-291.
- Twitchett, A. C., Yates, T.J.V., Somodi, P. K., Newcomb, S. B., Dunin-Borkowski, R. E. and Midgley, P., 2005. A three-dimensional analysis of the dopant potential of a silicon p-n junction by holographic tomography. *Springer Proceedings In Physics* 107, 229-232.
- Uhlemann, S. and Haider, M., 1998. Residual Wave Aberrations in the First Spherical Aberration Corrected Transmission Electron Microscope. *Ultramicroscopy* 72, 109-119.
- Urban, K., Kabius, B., Haider, M. and Rose, H., 1999. A way to higher resolution: spherical-aberration correction in a 200 kV transmission electron microscope. *Journal of Electron Microscopy*

48, 821-826.

Valle, M., Zavialov, A., Li, W., Stagg, S. M., Sengupta, J., Nielsen, R. C., Nissen, P., Harvey, S. C., Ehrenberg, M. and Frank, J., 2003. Incorporation of aminoacyl-tRNA into the ribosome as seen by cryo-electron microscopy. *Nature Structural Biology* 10, 899-906.

van Aken, P.A., Koch, C.T., Sigle, W., Höschel, R., Rühle, M., Essers, E., Benner, G. and Matijevic, M., 2007. The Sub-Electron-Volt-Sub-Angstrom-Microscope (SESAM): Pushing the Limits in Monochromated and Energy-Filtered TEM. *Microsc Microanal* 13 (Suppl 2).

Wanner, M., Bach, D., Gerthsen, D., Werner, R. and Tesche, B., 2006. Electron holography of thin amorphous carbon films: Measurement of the mean inner potential and a thickness-independent phase shift. *Ultramicroscopy* 106, 341-345.

Yasuta, H., Okawara, H. and Nagayama, K. 2006. Aharonov-Bohm Phase Plate in Transmission Electron Microscopy. 16th International Microscopy Congress, Sapporo (Japan).

Zernike, F., 1935. Das Phasenkontrastverfahren bei der mikroskopischen Beobachtung. *Phys. Z.* 23, 848.

Publications

Journal publications

- K. Schultheiß, F. Pérez-Willard, B. Barton, D. Gerthsen and R. R. Schröder: Fabrication of a Boersch phase plate for phase contrast imaging in a transmission electron microscope. *Rev. Sci. Instrum.* 77 (2006) pp. 033701-4
- E. Majorovits, B. Barton, K. Schultheiß, F. Pérez-Willard, D. Gerthsen and R. R. Schröder: Optimizing phase contrast in transmission electron microscopy with an electrostatic (Boersch) phase plate. *Ultramicroscopy* 107 (2007) pp. 213-226
- B. Barton, F. Joos and R. R. Schröder: Improved Specimen Contrast by Hilbert Phase Plate Tomography. *J. Struct. Biol.*, under review

Conference talks

- R.R. Schröder, B. Barton, E. Majorovits, K. Schultheiß, F. Pérez-Willard, D. Gerthsen: Achieving Phase Contrast TEM Using an Electrostatic Boersch Phase Plate. *Proc. ICM 16, Sapporo, Japan 2006*
- B. Barton, E. Majorovits and R. R. Schröder: Improving signal transfer of the electrostatic Boersch phase plate for TEM by single-sideband imaging. *Proc. ICM 16, Sapporo, Japan 2006*
- K. Schultheiß, F. Pérez-Willard, D. Gerthsen, B. Barton, R. R. Schröder: Fabrication of a Boersch Phase Plate for Phase Contrast Imaging in a Transmission Electron Microscope. *Proc. ICM 16, Sapporo, Japan 2006*
- K. Schultheiß, B. Barton, F. Pérez-Willard, D. Gerthsen, R.R. Schröder: Fabrication of a Boersch Phase Plate for Phase Contrast Imaging in a Transmission Electron Microscope, *Proc. ACMM 19, Sydney, Australia 2006*
- R. R. Schröder, B. Barton, H. H. Rose, G. Benner: Contrast Enhancement by Anamorphic Phase Plates in an Aberration-Corrected TEM. *Proc. M&M 2007, Ft. Lauderdale, USA*
- D. Gerthsen, K. Schultheiß, B. Barton and R. R. Schröder: Effect of a Physical Phase Plate on Contrast Transfer in an Aberration-Corrected Transmission Electron Microscope. *Proc. M&M 2007, Ft. Lauderdale, USA*
- B. Barton and R. R. Schröder: Electron Tomography of Unstained Cell Sections using a Half-Plane (Hilbert) Phase Plate. *Proc. M&M 2007, Ft. Lauderdale, USA*
- B. Barton and R.R. Schröder: Electron Tomography of Unstained Cell Sections Using a Half-Plane (Hilbert) Phase Plate. *Proc. MC 2007, Saarbrücken, Germany 2007*
- R.R. Schröder, B. Barton, H. Rose and G. Benner: Contrast Enhancement by Anamorphic Phase Plates in an Aberration Corrected TEM. *Proc. MC 2007, Saarbrücken, Germany 2007*

Danksagung

Ich danke Rasmus Schröder, von dem ich während der letzten Jahre sehr viel gelernt habe, für die Betreuung meiner Doktorarbeit. Für die Betreuung seitens der Fakultät für Physik und Astronomie bedanke ich mich bei Herrn Prof. Christoph Cremer, und bei Frau Prof. Dagmar Gerthsen für die erfolgreiche Zusammenarbeit während des gesamten Projekts. Werner Kühlbrandt hat als Direktor des MPI unsere Arbeit ebenfalls nach Kräften unterstützt.

Viele der Ergebnisse wären ohne die Mitarbeit von Katrin Schultheiß nicht zustande gekommen – dafür vielen Dank. Gleiches gilt für Björn Gamm und Fabian Pérez-Willard (alle LEM Karlsruhe). Ich bedanke mich bei Jürgen Reichert, Fabian Baur, Steffen Rebenich und Fabian Bayer aus der Feinwerkstatt des MPI für viele wunderschöne Werkstücke in Rekordzeit. Danke auch an Friederike Joos, Winfried Haase, Christiane Feuerbach, Rolf Bergbauer, Deryck Mills, Mike Strauss und Götz Hofhaus (MPI). Für Unterstützung von Seiten der Fa. Carl Zeiss SMT bedanke ich mich bei Gerd Benner, Endre Majorovits, Gerhard Brümmer, Heinz Drexler, Thilo Mandler und natürlich Stefan Lengweiler für die Goniometer-Entwicklungshilfe. Danke an Simone Lepper (Uni Heidelberg) für die zwei (leider recht vergeblichen) Trips nach Ffm. Thanks to Rado Danev (NRI Okazaki) for useful tips on phase plates.

Für die finanzielle Unterstützung während dieser Doktorarbeit möchte ich mich bei der Deutschen Forschungsgemeinschaft (DFG) bedanken, ebenso bei der Max-Planck-Gesellschaft. Unterstützung in Form von Reisestipendien erhielt ich von der Deutschen Gesellschaft für Elektronenmikroskopie (DEG), der European Microscopy Society (EMS) und der Microscopy Society of America (MSA).